Solar Power Integration into the Saudi Arabian Power Grid

A Dissertation Presented for the

Doctor of Philosophy

Degree

The University of Tennessee, Knoxville

Abdulelah Yousef Alharbi

December 2018

© by Abdulelah Yousef Alharbi, 2018

All Rights Reserved.

Dedication

I would like to dedicate this dissertation to my beloved parents, my lovely wife, and my kids.

Acknowledgments

First and foremost, all praises to Allah, the Almighty, for giving me the sustenance, the courage, and the guidance throughout my life. Without his countless blessings, continuous grace, and strength, completing this dissertation would not have been accomplished.

I would like to express my sincere appreciation to my academic and thesis advisor, Dr. Yilu Liu for her professional guidance, constant support, and continuous encouragement throughout this dissertation work. She has consistently been there whenever I was in need. I am much indebted to Dr. Liu for the educational knowledge, skills, and experience I have acquired in my journey towards this degree. Indeed, I cannot be more lucky and grateful to have her as my supervisor.

I would like to express my profound gratitude and thanks to my PhD committee members, Dr. Fangxing Li, Dr. Hairong Qi, and Dr. Khalid Alshibli for their significant effort and precious time. Their professional comments, critiques, and feedback are really inspiring and helpful in improving the quality of this research.

My sincere thanks also go to all faculty members in the department of electrical engineering at UTK for their high-quality lectures, cooperation and generous support during my doctoral education. In addition, I was very fortunate to be part of PowerIT lab group. I

am very grateful to all group members for their fruitful discussions and professional comments during the research progress.

My acknowledgement would not be completed without thanking my beloved parents, Yousef and Ghazeel Alharbi, for their praying, countless scarifies, and infinite support throughout my entire life. I can never ever thank them enough. Also, not forgetting to thank my parents in law for their praying, unlimited encouragement, and moral support. Additionally, I would like to express my sincere appreciation to all my family members for their motivation, tremendous support, and best wishes. Their help and care enabled me to overcome many difficulties during this journey.

Last but not least, my highest and affectionate thanks go to my loving wife, Mashael Alharbi, for her dedication, selfless love, and sincere support. She always understands me and shares the struggle with me in the hardest moments of my personal and academic life. She kept encouraging me toward success even when things got tough during the work on this research. From the bottom of my heart, thank you for everything, for your commitment and taking care of my children. I am truly blessed to have such a great wife. Mashael, without you, I would not have gone this far. At the same time, I would like to express my heartfelt appreciation and love to my kids, Fajr and Talal, for their great patience and endless love. They are the biggest source of my life joy and my first source of inspiration. I just cannot tell how much they mean to me.

I would like to thank my sponsor, Qassim University represented by Saudi Arabian Cultural Mission to the United States, for giving me the opportunity to study abroad and the generous financial support. Without their help and efforts, this work would have never existed. Finally, I would like to thank those who indirectly contributed in this achievement.

Abstract

Recently, Saudi Arabia is going through a process of developing and modernizing various aspects of life in the country. In order to cope with these changes, reduce local oil consumption, and meet the high electricity demand, the trend has been to introduce renewable energy sources and limit fossil fuels power generation. This expected major renewable revolution in Saudi Arabia, in addition to the significant growth in the current grid size and demand, makes it essential to establish a comprehensive study about the status of the existing grid stability and the impact of incorporating renewable energy.

To address the aforementioned changes, an adaptive dynamic model is built based on the Saudi power system real data gathered from public domains. For higher accuracy, the developed model is tested and validated against field measurement data taken using the Frequency Monitoring Network (FNET/GridEye). Indeed, with the increasing penetration of the renewable energy, the voltage stability becomes one of the challenges to the existing power grid. The voltage stability status of the Saudi grid is firstly investigated and the recommended measures are implemented to ensure the stability of the network before integrating high level of renewable energy. Regarding solar energy, the information about solar radiation in Saudi Arabia proves the fact that most of the locations in the Kingdom

are suitable for installing solar planets. Thus, a large amount of solar energy is added to the Saudi power system in all operating areas. This research work explores the impact of the increased amount of solar energy on the frequency response of the Saudi grid under different disturbances and outage events. Having determined the adverse impact on the frequency response, this dissertation further analyzes some mitigation measures utilized to prevent frequency response degradation. Further, several dynamic stability studies are conducted to notice the effect on the inter-area oscillations and the rotor angle stability of the Saudi system when several photovoltaic penetration levels are introduced.

Table of Contents

1 INTRODUCTION **1**

1.1 Background 1

1.2 Motivation 2

1.3 Research Objectives 3

1.4 Dissertation Organization 5

2 SAUDI POWER SYSTEM DESCRIPTION AND MODELING **7**

2.1 Introduction 7

2.2 Saudi National Power Grid 8

2.2.1 Saudi Arabia Electricity Fuel Types 9

2.2.2 Saudi Arabian Power Grid Operating Areas 10

2.2.3 Regional and National Interconnections of the Power Grid 11

2.3 Saudi Arabian National Grid Model 13

2.3.1 Power Flow Data 13

2.3.2 Dynamic Simulation Model 17

2.4 Simulation Results 20

2.4.1 Flat Run Simulation 21

2.4.2 Generator Trip Events . . . 22
2.4.3 Load Shedding Events . . . 27
2.4.4 Line Trip Events . . . 31
2.5 Dynamic Model Validation of the Saudi Grid . . . 37
2.5.1 The Frequency Monitoring Network (FNET) . . . 38
2.5.2 Model Validation Cases . . . 40
2.6 Summary . . . 48

3 VOLTAGE STABILITY ASSESSMENT OF THE SAUDI POWER GRID 49

3.1 Introduction . . . 49
3.2 Voltage Stability . . . 50
3.2.1 Reactive Power Compensation Devices . . . 52
3.2.2 Impact of Load Characteristics . . . 55
3.3 Voltage Stability Analysis . . . 56
3.3.1 V-Q Sensitivity Analysis . . . 57
3.3.2 Q-V Modal Analysis . . . 58
3.3.3 PV Curve Analysis . . . 60
3.3.4 QV Curve Analysis . . . 60
3.4 Saudi Grid Voltage Stability Analysis . . . 61
3.4.1 Load Bus Voltages . . . 62
3.4.2 V-Q Sensitivity Analysis . . . 63
3.4.3 Q-V Modal Analysis . . . 63
3.4.4 Active Power and Reactive Power Margins . . . 66

3.4.5 Remedial Measures . . . 69
3.5 Summary . . . 71

4 SOLAR ENERGY IN SAUDI ARABIA 73

4.1 Introduction . . . 73
4.2 Advantages of Solar Penetration in the Saudi Grid . . . 75
4.3 History of Solar Energy in Saudi Arabia . . . 77
4.4 Solar Irradiance in Saudi Arabia . . . 80
4.4.1 Solar Irradiance in Saudi Arabia from December 2015 to November 2017 81
4.5 Summary . . . 87

5 IMPACT OF THE SOLAR PENETRATION ON THE FREQUENCY STABILITY OF THE SAUDI POWER GRID 88

5.1 Introduction . . . 88
5.2 Solar PV Penetration in the Saudi Grid . . . 89
5.2.1 Solar PV Model . . . 89
5.2.2 Solar PV Plants Locations and Penetration Levels . . . 92
5.2.3 Flat Run Simulation with High PV Penetration . . . 94
5.3 Impact of High PV Penetration in the Saudi Grid on Frequency Response . . . 95
5.3.1 Impact of Losing a Conventional Generator . . . 97
5.3.2 Impact of Tripping a Large PV Plant . . . 101
5.3.3 Impact on Frequency Response Characteristic . . . 102
5.3.4 Impact on Frequency Metrics . . . 103
5.3.5 Impact on Under-Frequency Load Shedding . . . 109

5.3.6 Impact of 100% PV Penetration at One Area 114
5.3.7 Improving the Frequency Response by Using Mitigation Methods . . 117
5.3.8 Energy Storage for Frequency Regulation 125
5.4 Summary 135

6 IMPACT OF THE SOLAR PENETRATION ON THE ROTOR ANGLE STABILITY OF THE SAUDI POWER GRID **137**

6.1 Introduction 137
6.2 Impact on Critical Clearing Time 138
6.3 Impact on Inter-Area Oscillations 148
6.4 Summary 159

7 CONCLUSION **160**

BIBLIOGRAPHY **165**

APPENDICES **185**

A Meteorological Stations Information 186
B GE PV Model Control Strategies and Dynamic Parameters 192
C Lists of the Displaced Conventional Generators for PV Plants 195
D Additional Results for Generator Trip Cases with Higher PV Penetration . . 199

VITA **203**

List of Tables

2.1 Buses distribution through Saudi grid model. 14

2.2 Power flow results. 16

2.3 Active and reactive power generation and load at each region. 16

2.4 Dynamic model data for round rotor units (GENROU PSS®E model). . . . 18

2.5 Dynamic model data for simplified excitation systems (SEXS PSS®E model). 19

2.6 Summary of the disturbances events. 46

3.1 Load buses voltage magnitudes. 63

3.2 Highest V-Q sensitivities. 64

3.3 The smallest eigenvalues of $[J_R]$. 64

3.4 Highest bus participation factors. 65

3.5 Highest branch participation factors. 67

3.6 Active and reactive power margins. 67

3.7 Critical buses profiles after adding series capacitors. 69

3.8 Final critical buses profiles. 71

5.1 The generation amount for each of the solar PV penetration levels. 93

5.2 Typical contingencies at each operating area. 110

5.3 Governor responsive generation capacity. 118

5.4 Impact of adjusting governor ratio on the frequency response metrics. 124

5.5 Impact of adjusting governor droop on the frequency response metrics. . . . 124

6.1 Transmission lines with highest power flow. 142

6.2 Comparison of CCTs values for the ten cases (Unit: Cycle). 142

6.3 AM transient stability index for the ten cases. 146

6.4 Oscillation frequency and damping ratio of the critical modes for the base case. 152

A.1 Stations elevation and instruments types. 186

A.2 Irradiance information in Saudi Arabia. 188

A.3 Average monthly DHI/GHI ratio for all stations. 190

B.1 GE PV model control strategies. 192

B.2 Dynamic model data for control model (GEPVE). 192

B.3 Dynamic model data for inverter model (GEPVG). 194

C.1 List of the displaced conventional generators for 10% PV penetration level. . 195

C.2 List of the displaced conventional generators for 30% PV penetration level . . 196

C.3 List of the displaced conventional generators for 50% PV penetration level . . 197

C.4 List of the displaced conventional generators for 65% PV penetration level. . 198

List of Figures

2.1 Saudi Arabia electricity fuel types. 10

2.2 Saudi power grid and generation stations. 11

2.3 Gulf Cooperation Council (GCC) grid interconnection. 13

2.4 Single line diagram of the Saudi power grid. 15

2.5 Block diagram for the GENROU PSS®E model. 17

2.6 Block diagram for the SEXS PSS®E model. 19

2.7 Block diagram for the TGOV1 model. 20

2.8 Block diagram for the GAST model. 20

2.9 Machine speed deviation without disturbance. 21

2.10 Machine terminal voltage deviation without disturbance. 22

2.11 The frequency response after generator trip at bus 102. 23

2.12 The voltage response after generator trip at bus 102. 23

2.13 The frequency response after generator trip at bus 211. 24

2.14 The voltage response after generator trip at bus 211. 25

2.15 The frequency response after generator trip at bus 309. 26

2.16 The voltage response after generator trip at bus 309. 26

2.17 The frequency response after load shedding at bus 119. 27
2.18 The voltage response after load shedding at bus 119. 28
2.19 The frequency response after load shedding at bus 201. 29
2.20 The voltage response after load shedding at bus 201. 29
2.21 The frequency response after load shedding at bus 308. 30
2.22 The voltage response after load shedding at bus 308. 31
2.23 The frequency response after tripping the line between 102 and 122. 32
2.24 The voltage response after tripping the line between 102 and 122. 32
2.25 The frequency response after tripping the line between 108 and 406. 33
2.26 The voltage response after tripping the line between 108 and 406. 34
2.27 The power flow at the lines connecting WOA and SOA. 34
2.28 The frequency response after tripping the line between 215 and 301. 36
2.29 The voltage response after tripping the line between 215 and 301. 36
2.30 The power flow at the lines connecting EOA and COA. 37
2.31 The main structure of the FNET system. 39
2.32 FDR locations for the proposed FNET system in Saudi Arabia. 40
2.33 FDR frequency response after generator trip in August 2016. 41
2.34 Case 1 locations. 41
2.35 Simulation and measurement comparison of case 1 before the modification. . 43
2.36 Simulation and measurement comparison of case 1 after the modification. . . 44
2.37 FDR frequency response after generator trip in July 2016. 45
2.38 Case 2 locations. 45
2.39 Simulation and measurement comparison of case 2 before the modification. . 47

2.40 Simulation and measurement comparison of case 2 after the modification. . . 47

3.1 Standard QV curve. 62

3.2 Buses and branches with the highest participation factors. 66

3.3 PV curve for bus 303. 68

3.4 QV curves for all five load buses. 68

3.5 PV curves for bus 303 after inserting series capacitors. 70

3.6 QV curves for all five load buses after inserting series capacitors. 70

4.1 Best ten cites for solar irradiance in Saudi Arabia. 81

4.2 Map of the solar monitoring network in Saudi Arabia 83

4.3 Summary of the average solar irradiance and temperature in all sites. 84

4.4 Average monthly solar irradiance for all regions. 85

4.5 Average global horizontal irradiance in the southern region. 86

4.6 Averages monthly DHI/GHI ratio for each region. 87

5.1 General structure of a grid connected solar PV plant. 89

5.2 Load flow representation of large scale PV unit. 90

5.3 GE solar PV model dynamic model overview. 91

5.4 10% PV penetration map. 93

5.5 30% PV penetration map. 93

5.6 50% PV penetration map. 94

5.7 65% PV penetration map. 94

5.8 Frequency deviations without disturbance. 96

5.9 Single line diagram of the western operating system. 98
5.10 Frequency response after tripping a conventional generator in the WOA. . . 98
5.11 Single line diagram of the central operating system. 99
5.12 Frequency response after tripping a conventional generator in the COA. . . . 100
5.13 Frequency response after tripping a large PV plant. 101
5.14 Saudi grid *Beta* value with different PV penetration levels. 102
5.15 Frequency responses with different PV levels after a contingency in the WOA. 104
5.16 Frequency responses with different PV levels after a contingency in the SOA. 105
5.17 ROCOF change due to increased PV penetration level. 105
5.18 Frequency nadir change due to increased PV penetration level. 106
5.19 Nadir time change due to increased PV penetration level. 106
5.20 Settling frequency change due to increased PV penetration level. 107
5.21 Settling time change due to increased PV penetration level. 107
5.22 Maximum deviation for all frequency metrics from the mean value with different PV penetration levels. 108
5.23 Frequency responses after 1,684 MW generator loss in the WOA. 110
5.24 Frequency responses after 1,237 MW generator loss in the EOA. 111
5.25 Frequency responses after 1,722 MW generator loss in the COA. 111
5.26 Frequency responses after 1,259 MW generator loss in the SOA. 112
5.27 Frequency responses after 1,282 MW generator loss in the NOA. 112
5.28 Regional and national frequency responses for 10% PV penetration level. . . 115
5.29 Regional and national frequency responses for 65% PV penetration level. . . 115
5.30 Frequency response after tripping 1 GW of PV units in the NOA. 116

5.31 Frequency response with various governor ratios for the 30% PV case. 119
5.32 Frequency response with various governor ratios for the 65% PV case. 119
5.33 Frequency response with various governor droops for the 30% PV case. . . . 121
5.34 Frequency response with various governor droops for the 65% PV case. . . . 121
5.35 Frequency response with various governor ratios and droops for the 30% PV case. 123
5.36 Frequency response with various governor ratios and droops for the 65% PV case. 123
5.37 Single line diagram of active power control of the CBEST model. 127
5.38 Frequency responses with unlimited BESS capacitates in the WOA. 128
5.39 Frequency responses with unlimited BESS capacity at different locations. . . 129
5.40 Frequency nadir with unlimited BESS capacitates at different locations. . . . 130
5.41 Nadir time with unlimited BESS capacitates at different locations. 130
5.42 Settling frequency with unlimited BESS capacitates at different locations. . . 131
5.43 Frequency responses with limited BESS capacitates in the WOA. 132
5.44 Frequency responses with limited BESS capacity at different locations. . . . 132
5.45 Frequency nadir with limited BESS capacitates at different locations. 133
5.46 Nadir time with limited BESS capacitates at different locations. 133
5.47 Settling frequency with limited BESS capacitates at different locations. . . . 134

6.1 Critical clearing time (CCT) changes with different PV penetration levels. . 143
6.2 Critical clearing time (CCT) changes with different voltage control strategies. 144

6.3 Rotor angle oscillations of a machine in the COA with different penetration levels. . . . 145
6.4 Rotor angle oscillations of a machine in the WOA with different penetration levels when a fault lasted for 8.10 cycles. . . . 145
6.5 Oscillations of synchronous machines rotor angles after applying a fault in the WOA. . . . 147
6.6 Oscillations of synchronous machines rotor angles after applying a fault in the EOA. . . . 147
6.7 Tripped generators and observation locations. . . . 151
6.8 Mode 1 inter-area oscillation frequency. . . . 153
6.9 Mode 1 inter-area oscillation damping ratio. . . . 153
6.10 Mode 2 inter-area oscillation frequency. . . . 154
6.11 Mode 2 inter-area oscillation damping ratio. . . . 154
6.12 Mode shape of the inter-area mode (Mode1). . . . 156
6.13 Mode shape of the inter-area mode (Mode2). . . . 157
6.14 Inter-area oscillation frequency with four PV control strategies. . . . 158
6.15 Inter-area oscillation damping ratio with four PV control strategies. . . . 158

D.1 Frequency responses with different PV levels after a contingency in the EOA. 199
D.2 Frequency responses with different PV levels after a contingency in the COA. 199
D.3 Frequency responses with different PV levels after a contingency in the NOA. 200
D.4 Frequency responses for each area after a generator loss in the COA with 10% PV. . . . 200

D.5 Frequency responses for each area after a generator loss in the COA with 30% PV. 201
D.6 Frequency responses for each area after a generator loss in the COA with 50% PV. 201
D.7 Frequency responses for each area after a generator loss in the COA with 65% PV. 202

Nomenclature

AM	Power Angle-Based Stability Margin
$\boldsymbol{\beta}$	Frequency Response Characteristic
BESS	Battery Energy Storage System
CCT	Critical Clearing Time
COA	Central Operating Area
CSP	Concentrating Solar Thermal Power Plant
DHI	Diffuse Horizontal Irradiance
DNI	Direct Normal Irradiance
ECRA	Saudi Arabia's Electricity & Cogeneration Regulatory Authority
EHV	Extra High Voltage
EI	Eastern Interconnection
EOA	Eastern Operating Area
ESS	Energy Storage System
FACTS	Flexible Alternating Current Transmission System
FDR	Frequency Disturbance Recorder
FNET/GridEye	Frequency Monitoring Network

GEPVE	GE PV Electrical Control
GEPVG	GE PV Electrical Inverter
GHI	Global Horizontal Irradiance
HVDC	High Voltage Direct Current Transmission System
$[\boldsymbol{J_R}]$	Reduced Jacobean Matrix
K.A.CARE	King Abdullah City for Atomic and Renewable Energy
$\boldsymbol{K_t}$	Governor Ratio
NOA	Northern Operating Area
PMU	Phasor Measurement Unit
PSS®E	Power System Simulator for Engineers
PV	Photovoltaic
PV Curve	Active Power-Voltage Curve
QV Curve	Reactive Power-Voltage Curve
ROCOF	The Rate of Change of Frequency in mHz/s
SEC	Saudi Electricity Company
SIL	Surge Impedance Load
SOA	Southern Operating Area
UFLS	Under-Frequency Load Shedding
WOA	Western Operating Area

Chapter 1

INTRODUCTION

1.1 Background

The new Saudi leadership are keenly interested in diversifying the country's economic activities in all different aspects, including the intention to shift towards renewable energy resources. The main purpose of the Saudi Vision 2030 plan, issued in April 2016, is to reduce the country's oil dependency. Hence, the vision sets a target of electrifying the Kingdom using renewable energy resources. It sets an initial goal of generating 9.5 GW of power from renewable resources by 2030. Additionally, in order to reduce the increasing power demand, in August 2017, Saudi Arabia's Electricity & Cogeneration Regulatory Authority (ECRA) has issued regulatory rules for consumers to run their own small-scale solar photovoltaic (PV) systems and export solar power to the distribution grid. This work takes place in mid-2018 with no more than two megawatts for each power consumer [1]. On March 2018, Saudi Arabia and SoftBank Group Corp. agreed to construct the world's biggest solar power with a capacity of 200 GW in the Kingdom by 2030. The project, which includes a construction

of solar panels and investing in the battery technology, would cost $200 billion by the end of the project. It is claimed that the project will start by installing 7.2 GW by the mid of the 2019 as the short-term project plan [2].

These ambitious projects of utilizing solar PV generation can provide enormous economic and environmental benefits. Solar energy would reduce the pollutant emission and the associated global warming. Also, it could be considered cost effective energy resource, taking into account the savings of reducing petroleum local consumption and the costs of environmental and health destruction caused by traditional power plants pollution. Besides, the geographical location of the country encourages Saudi government to easily consider the solar power as an alternative energy source.

1.2 Motivation

The Saudi government is making a historic transformation by reducing its dependency on oil, including burning oil and natural gas to generate electricity. This means that the country is targeting sustainable renewable energy in the foreseeable future. Solar energy is the major power source that can be exploited easily in Saudi Arabia due to the abundant solar radiation throughout the country.

Saudi Arabia, however did not have a history of large-scale solar energy penetration and the solar power industry is limited in the country. As far as the author knows, there are no studies investigating the stability impact of the high solar energy penetration in the Saudi grid. It is known that high solar PV penetration could considerably influence the stability of a power grid due to their features that are different from the conventional power

generation sources. This is what stimulated the interest to analyze the possible impact of higher photovoltaic integration on the stability of the Saudi national power grid.

Several blackouts have been lately reported in the Saudi grid due to voltage stability issues. Additionally, the Saudi grid has experienced an increase in load demand that might deteriorate the voltage stability of the grid by letting the system operate close to the stability limits. Also, it has been addressed that the voltage stability is one of the major parameters that are heavily affected by the solar penetration. For that purpose, it is critical to check the voltage stability status of the existing grid and apply useful preventive actions before interconnecting renewable energy resources.

Unfortunately, the Saudi grid dynamic model is not shared publicly. However, in order to perform the above-mentioned studies, a reliable dynamic model that resembles the actual Saudi power grid is required. Therefore, an adaptive dynamic model of the Saudi grid needs to be built using PSS®E software based on the real data gathered from the available public database provided by Saudi Arabia's Electricity & Cogeneration Regulatory Authority (ECRA).

1.3 Research Objectives

The specific objectives of this dissertation can be summarized as follows:

- Building an adaptive dynamic model representing the Saudi national grid, including all operating regions.

- Testing the Saudi model by applying several disturbances (e.g., generator trip, load shedding, and line trip) at different locations in the grid to validate the dynamic stability of the model.
- Validating the model accuracy by comparing the field measurements for generation trip cases collected by (FNET/GridEye) with the simulation results.
- Checking the status of Saudi power system's voltage stability using static analysis techniques.
- Identifying the weakest buses and branches in the Saudi grid in terms of voltage stability using V-Q sensitivity analysis and Q-V modal analysis.
- Estimating the system proximity to voltage collapse limits using PV and QV curves.
- Proposing mitigation procedures to improve the voltage stability of the Saudi grid.
- Analyzing the solar irradiance in Saudi Arabia in the last two years.
- Finding the maximum allowable penetration levels of solar plants and their locations.
- Studying the impact of large-scale penetration of solar planets on the frequency stability of the Saudi power system.
- Investigating the preventive actions used to enhance the frequency stability.
- Studying the impact of large-scale solar generation on the critical clearing time.
- Studying the impact of large-scale solar generation on the inter-area oscillations.

1.4 Dissertation Organization

This dissertation work is structured in seven chapters.

The second chapter describes the process of creating the dynamic model of the Saudi grid. It summarizes the required information about the Saudi power system, including operating regions, generation capacity, load demands, and generation units and their fuel types. The dynamic stability of the developed model is examined by applying different disturbances. This chapter presents two real events to validate the accuracy of the dynamic model against field measurements.

In the third chapter, the static analysis approaches used for voltage stability analysis are generally reviewed. This chapter studies the voltage stability status of the Saudi grid. Suggested preventive actions that can be used to avoid voltage instability issues are presented at the end of this chapter.

The fourth chapter begins with a general review of the history of solar energy in Saudi Arabia. It also highlights the advantages and challenges of utilizing solar power in the Kingdom. The solar radiation pattern in the last years in Saudi Arabia is analyzed in this chapter.

Chapter five discusses the procedures of adding solar panels into the Saudi grid along with the photovoltaic modeling aspects. The main goal of this chapter is to investigate the effect associated with large scale penetration of PV units on the frequency stability of the Saudi grid. This is done through looking at the frequency response after applying different types of contingencies. This chapter presents methods to improve frequency response with higher solar energy penetration.

Chapter six concentrates on the rotor angle stability impact as a result of higher PV penetration. The study scope includes transient stability and small-signal stability by observing the impact on the critical clearing time and the inter-area oscillations.

The concluding chapter summarizes the major findings of the dissertation work and suggests the scope and the direction for the possible future work that could be expanded based on this research.

Chapter 2

SAUDI POWER SYSTEM DESCRIPTION AND MODELING

2.1 Introduction

Saudi Arabia is the biggest country in the Middle East in western Asia with an area of 830,000 mi^2. It is among the world's highest oil producers, controlling about 20% of world's oil reserves. It is considered to be on the top of the list of the countries that burn oil and natural gas directly to generate electrical power. The country is expected to consume more oil and natural gas to meet the huge increase in the electricity consumption. Consequently, the Saudi government plans to diversify its sources of power generation and improve the current grid efficiency. Thus, the existing grid needs to be strong enough and be able to withstand the predicted changes in the near future like integrating renewable energy resources and interconnection with neighboring countries. A detailed description of the Saudi power grid and its dynamic model are presented in this chapter. Based on real data gathered from

public domain resources, the Saudi model is built and validated against field measurements for confirmed loss of generation cases.

2.2 Saudi National Power Grid

For several decades, fast population growth in Saudi Arabia has contributed significantly in the economic and the industrial developments. As a result, the electricity consumption has been growing rapidly for both residential, commercial and industrial sectors. It is estimated that the peak load increase has a rate of additional 10% each year. The peak load was 30 GW in 2005 and it reached almost 62 GW in 2016. The total number of customers has drastically increased to reach 8,607,000 in 2016 [3, 4]. By 2030, it is planned that the capacity of the electricity generation will reach 120 GW to be able to supply the expected huge increase in the electricity demand [5].

This substantial demand increase, in addition to the current and the future HVDC interconnections with neighboring countries as well as the proposed renewable energy generation, has made the Saudi power network experiencing many development projects. Therefore, several undergoing projects have been commenced in the Saudi power industry such as constructing new power plants as well as upgrading and expanding the existing power facilities. Additionally, in the last decade, private sectors have played an important role in reinforcing the power industry in Saudi Arabia by building very large power plants at different regions in the country such as four gigawatts-Qurayyah Independent Power Producer (IPP), which was built in 2014 and two gigawatts-Rabigh 2IPP, which was connected to the grid in

the middle of 2017 [4]. MARAFIQ, which is a private corporation, built IWPP (Independent Water and Power Producer) plants in Jubail with a total capacity of 2,941 MW.

80% of Saudi Arabia's geographical area are electrified by one company that is Saudi Electricity Company (SEC), which is more than 80% owned by the Saudi government [6]. It is the main responsible for both generation, transmission and distribution of the electric power in the country. It runs more than 50 power generation plants throughout the Kingdom [4]. Starting in 2012, the SEC has been going through a process of breaking into six totally owned subsidiaries as follows: four generation companies (GENCO's), one transmission company (National Grid), and one distribution company (DISTCO) [7].

2.2.1 Saudi Arabia Electricity Fuel Types

All generation plants in Saudi Arabia use conventional fossil fuels for power generation. They are all composed of gas turbines, steam turbines, combined cycle units, and diesel generation units. As shown in Figure 2.1, a significant proportion of the generation capacity, as of 2017, is provided by gas turbine units (GT) with more than 42% of the overall generation, directly followed by steam turbine units (ST) that supply 41% of the electricity. The amount of power produced by combined cycle units (CC) is about 15% while diesel units, which are mostly used in remote areas, yield less than one percent [4].

The main fuels that have been used for the centralized power plants are natural gas, crude oil, diesel oil, and heavy fuel oil (HFO) [4]. Generally, more than 43% of power plants are operated by natural gas, especially in the eastern part of the country where there is abundant of natural gas reserve. HFO is used as the primary fuel for most of the steam

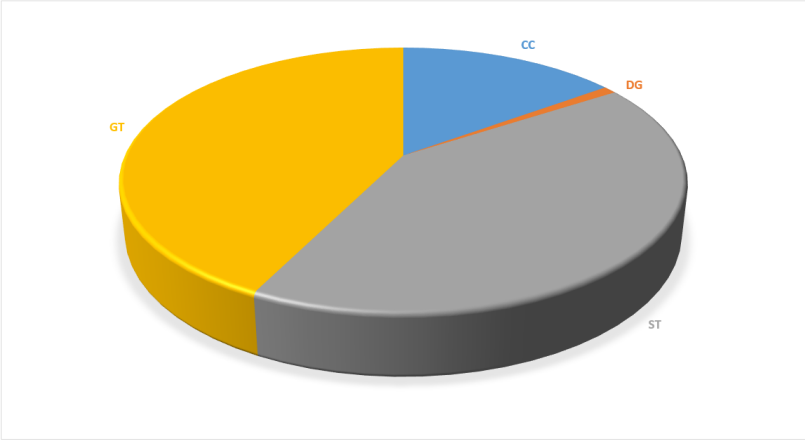


Figure 2.1: Saudi Arabia electricity fuel types, Adapted from [4].

turbine plants whereas the crude and the diesel oils are used for combined cycle units and small distributed generation units, respectively [4].

2.2.2 Saudi Arabian Power Grid Operating Areas

The Saudi power grid is mainly divided into four major operating areas based on their geographical locations: Western (WOA), Eastern (EOA), Central (COA), and Southern (SOA). The far northern area of the grid is going through interconnection projects to be connected with WOA in its western part and with COA in its eastern part. Figure 2.2 shows all operating areas in the Saudi grid and their voltage levels as well as generation stations and their units' types.

The national grid standard voltage levels range from 380 kV to 110 kV. As shown in Figure 2.2, the ultra-high voltage level 380 kV is mostly common in COA and WOA, while 230 kV transmission lines are mainly used in the eastern part of the grid. Most of the COA network is connected by 132 kV transmission lines to transfer the power from the generation stations to the load centers. Also, 132 kV conductors are distributed throughout the remote



Figure 2.2: Saudi power grid and generation stations [3].

areas in the southern and the northern regions. The voltage levels of 115 kV and 110 kV are mostly used in the EOA and WOA, respectively.

2.2.3 Regional and National Interconnections of the Power Grid

As of 2016, the Saudi power grid has a total installed capacity of 62 GW. The eastern operating area is the largest power producer with more than 34% of the total generation capacity whereas the SOA has only six gigawatts generation capacity. The central operating area consumes about 30% of the load, more than any other area in the Saudi grid [4]. To increase the grid reliability, reduce the overall installed capacity, and meet the projected demand in all areas, all operating areas have been interconnected recently to establish a national grid. Eastern area is exporting power to the central region via a 230 kV double circuit and two 380 kV transmission lines with double circuit, which can interchange approximately four gigawatts between the two areas [8]. The western region is connected

with the central and southern regions through 500 MW double circuit 380 kV lines and 300 MW single circuit 380 kV transmission line, respectively [9]. To achieve higher reliability and to increase power generation capacity, there is an expected plan to connect the central and western areas through a ±600 kV bipolar DC line with the maximum transfer of 3.5 GW and total distance of 770 km [8]. Furthermore, as a part of the major project of connecting the Saudi grid with the Egyptian grid, it is proposed that there will be a 530 km, ±500 kV HVDC line to connect the WOA with the northern small area [3].

In a national scale level, since Saudi Arabian power grid is the only grid operating at 60 Hz in the region, it is connected with neighboring grids of the other five Gulf states: the United Arab Emirates, Oman, Kuwait, Qatar, and Bahrain through 400 kV HVDC double circuit lines that include 900 km of overhead lines and a 37 km submarine cable to Bahrain. This Gulf Cooperation Council (GCC) grid allows Saudi network, particularly EOA region, to interchange a maximum of 1,200 MW as can be seen in Figure 2.3. The main objectives of this interconnection are interchanging the electrical power between all GCC members during emergency situations, reducing the spinning reserves of all countries, and improving the power reliability and the economic efficiency [10, 11].

On the west coast, Saudi Arabia has agreed with Egypt to interconnect their national grids by constructing approximately 1,500 km bipolar ±500 kV multi-terminal HVDC line. This line, which includes 25 km AC submarine, will allow electric capacity exchange of 3,000 MW between the two grids. This interconnection project will exploit the differences in the peak times between Saudi Arabia and Egypt and it is expected to start in 2019 [10]. Furthermore, there are several feasibility studies to evaluate the possibility of connecting the Saudi network with other regional and global networks.

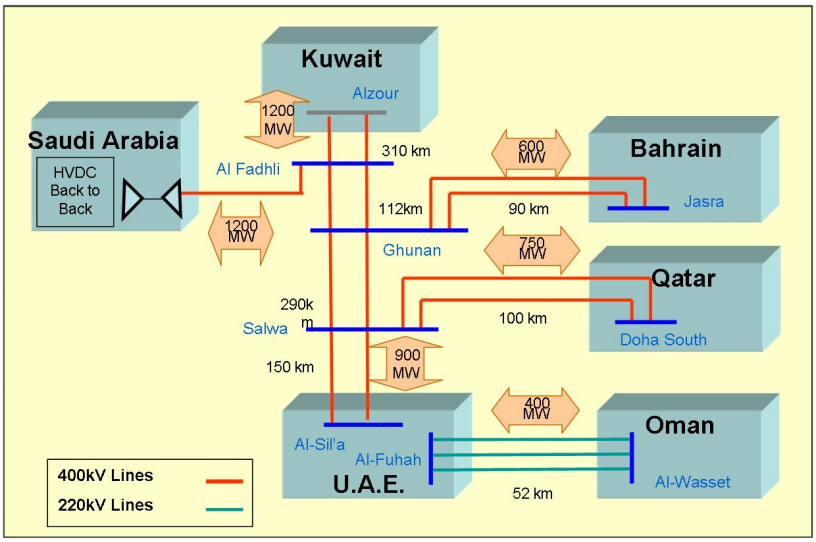


Figure 2.3: Gulf Cooperation Council (GCC) grid interconnection [11].

2.3 Saudi Arabian National Grid Model

In this study, the network model used to represent the Saudi grid is based on the load and generation capacity's latest data collected from Electricity & Cogeneration Regulatory Authority (ECRA) [4] domain and the annual reports from Saudi Electricity Company (SEC).

2.3.1 Power Flow Data

Steady state data such active power and load demand are provided while the missing data such as reactive power of each bus is estimated based on 0.95 power factor. The topology of the transmission lines is developed using Google Map tool. For transmission lines and machines' parameters, typical data are used. The Saudi power grid under study consists of 91 buses with voltage levels ranging from 380 kV to 110 kV. At each node, the generation capacity of units that have the same type is aggregated and represented by one machine.

Table 2.1 presents the distribution of the buses among the five operating areas. The single line diagram of the Saudi power grid is shown in Figure 2.4.

In this Model, Qurayyah bus (214) in the eastern region is randomly selected as the slack bus because it has the largest generation capacity. Using the Siemens PTI's PSS®E software, the power flow simulation is conducted using Newton Raphson method with five iterations for the base operating conditions, making sure that the voltage magnitudes are within 0.95-1.05 pu as the standards imposed by the SEC. The total active and reactive power generation are 60,895 MW and 23,843 Mvar, respectively while the active and reactive power demands are 59,979 MW and 19,714 Mvar, respectively. Tables 2.2 and 2.3 summarize the results of the power flow in the base case.

Table 2.1: Buses distribution through Saudi grid model.

Region	**Region code**	**Number of buses**
Western (WOA)	100	24
Eastern (EOA)	200	23
Central (COA)	300	18
Southern (SOA)	400	13
Northern (NOA)	500	13
Total		91

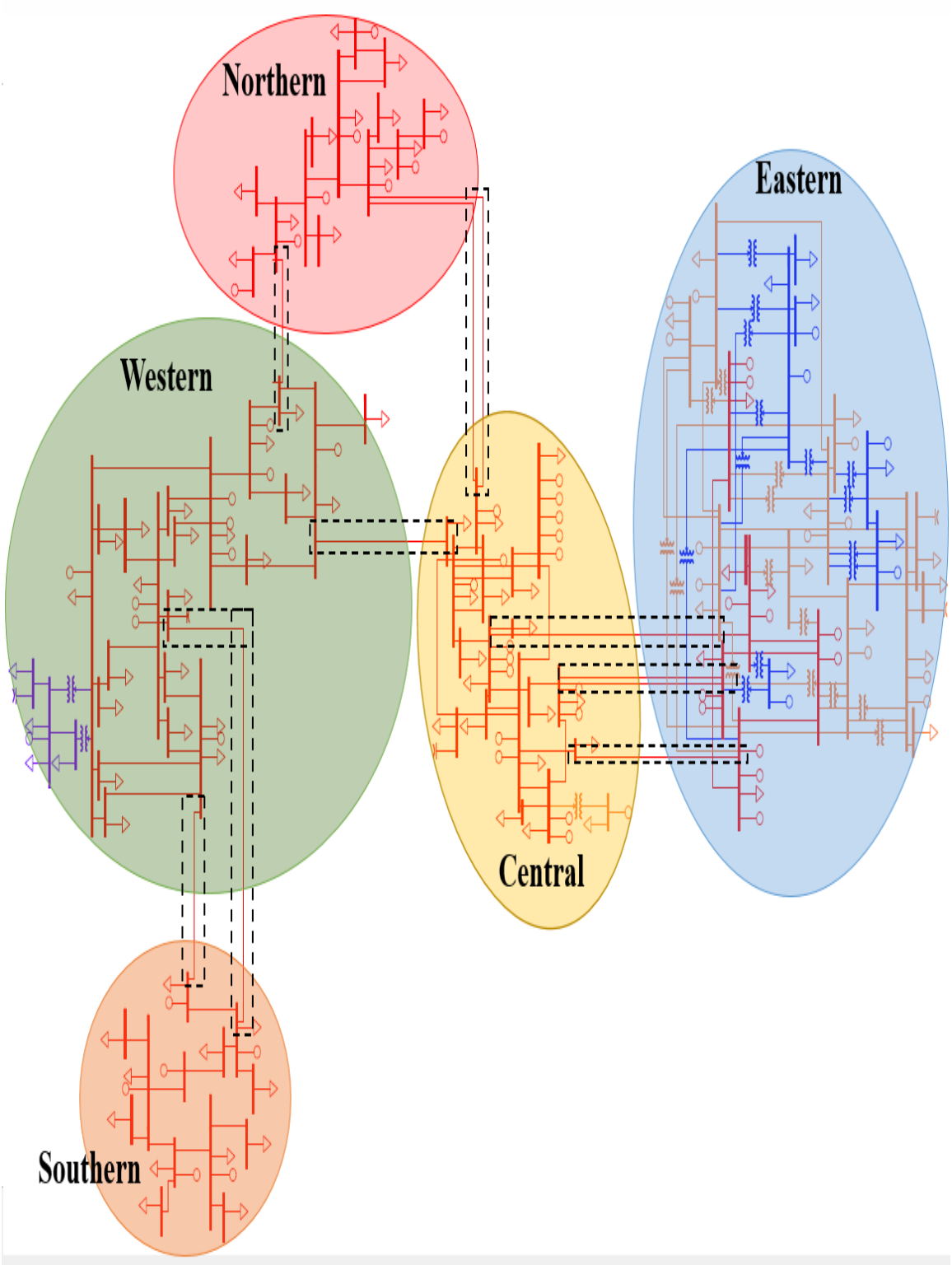


Figure 2.4: Single line diagram of the Saudi power grid.

Table 2.2: Power flow results.

Parameter	**Value**
Total active power generation	60,895.2 MW
Total reactive power generation	23,842.7 Mvar
Total active power load	59,978.6 MW
Total reactive power load	19,714.01 Mvar
Voltage limits	0.9526 pu to 1.0097 pu

Table 2.3: Active and reactive power generation and load at each region.

	WOA	**EOA**	**COA**	**SOA**	**NOA**
Generation (MW)	16,708.8	22,095.9	13,930.30	5,076.30	3,083.90
Load (MW)	16,123.4	17,783.4	18,999.04	4,814.60	2,258.15
Generation (Mvar)	6,501.90	6,384.30	7,016.600	3,704.90	235.0000
Load (Mvar)	5,299.51	5,845.12	6,244.680	2,112.48	212.2200

2.3.2 Dynamic Simulation Model

Based on their prime movers, all generation machines in any power station are considered to be identical units. They can be grouped and have the exact same dynamic model and parameters. Because of the unavailability of the dynamic model parameters, typical data are used for the parameters of the machines' models and their excitation control systems as well as governors' models based on [12, 13, 14].

Since all machines in the Saudi grid are thermal units, the PSS®E round rotor model (GENROU model) is the only generator model used in the developed Saudi model. The block diagram of the GENROU model is presented in Figure 2.5 and the dynamic model data for one of the models used in the Saudi power grid are presented in Table 2.4.

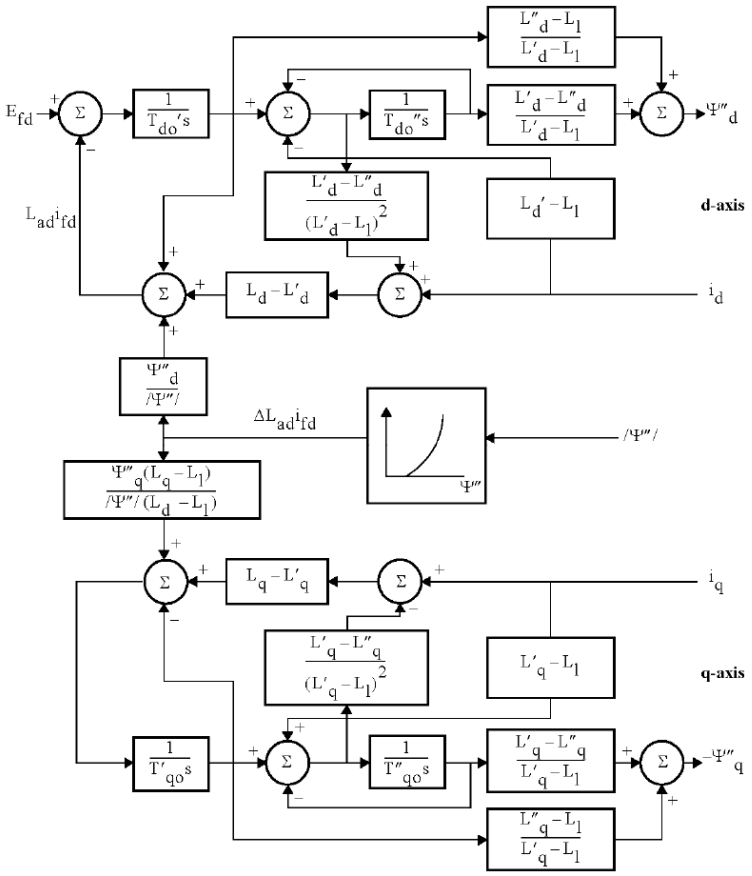


Figure 2.5: Block diagram for the GENROU PSS®E model [15].

Table 2.4: Dynamic model data for round rotor units (GENROU PSS®E model).

Parameter	**Value**
$T'd0(>0)(sec)$	8.0
$T"d0(>0)(sec)$	0.50
$T'q0(>0)(sec)$	1.0
$T'q0(>0)(sec)$	0.05
$H, Inertia$	3.9398
D, Speed damping	0
X_d	1.40
X_q	1.35
X'_d	0.30
X'_q	0.60
$X"_d = X"_q$	0.20
X_I	0.10
$S(1.0)$	0.03
$S(1.2)$	0.40

The PSS®E simplified excitation system (SEXS model) is considered for the excitation systems associated with each machine in the Saudi model. The block diagram of the exciter model is shown in Figure 2.6 while its parameters for one of the generation units in the studied model are summarized in Table 2.5. In terms of governor models, the steam turbine-governor model (TGOV1) is used for the slack unit and gas turbine-governor model (GAST) is used for all gas turbine units [16]. The control diagrams of the TGOV1 and GAST governors are illustrated in Figure 2.7 and Figure 2.8, respectively.

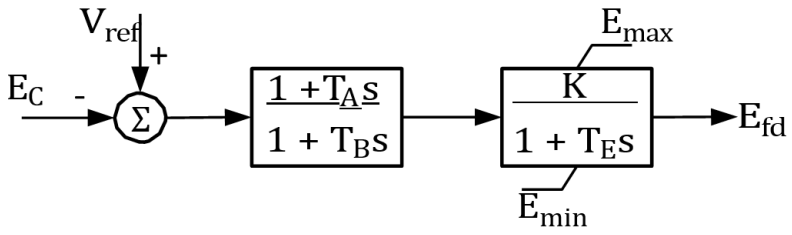


Figure 2.6: Block diagram for the SEXS PSS®E model [16].

Table 2.5: Dynamic model data for simplified excitation systems (SEXS PSS®E model).

Parameter	**Value**
$TA/TB)$	0.10
$TB(>0)$	10.0
K	100
TE	0.1
$EMIN$	-4.0
$EMAX$	5.0

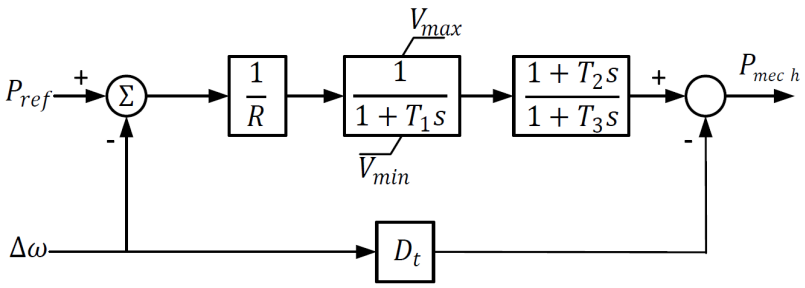


Figure 2.7: Block diagram for the TGOV1 model [16].

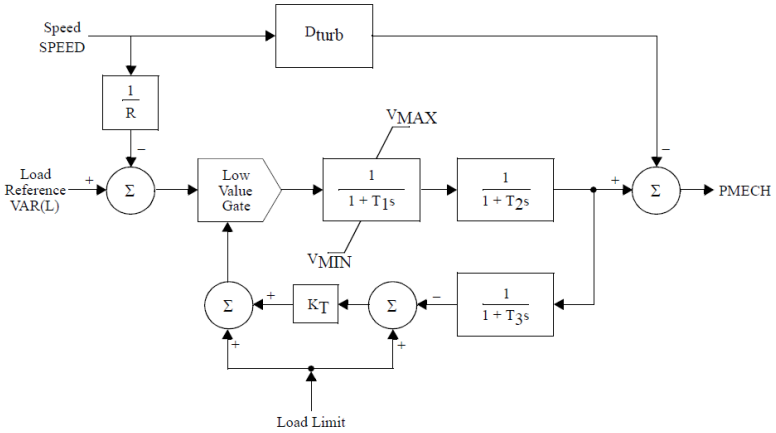


Figure 2.8: Block diagram for the GAST model [16].

In regard of load characteristics, the information about load dynamic characteristics is not available; therefore, a simple load model is used to approximately represent the load impact on system dynamics. The active and reactive power loads are converted to 100% constant current load and 100% constant admittance load, respectively.

2.4 Simulation Results

To validate the dynamic stability of the Saudi grid model, initial testing simulation and several time-domain simulations of different disturbances at different locations in the grid have been applied. Those disturbances are generator trips, load shedding, and line trips.

2.4.1 Flat Run Simulation

The first step to validate a dynamic model is to observe the behavior of the developed model when there is no disturbance [17]. For the Saudi dynamic model, a no-disturbance simulation that lasts 40 seconds is executed. The deviations in both speed and terminal voltage of all machines in the model are observed and the results are shown in Figure 2.9 and Figure 2.10, respectively. It can be seen that the magnitudes of the deviations are very small and within the order of 10^{-7} for both quantities. This indicates that this model is dynamically stable when no disturbance occurs.

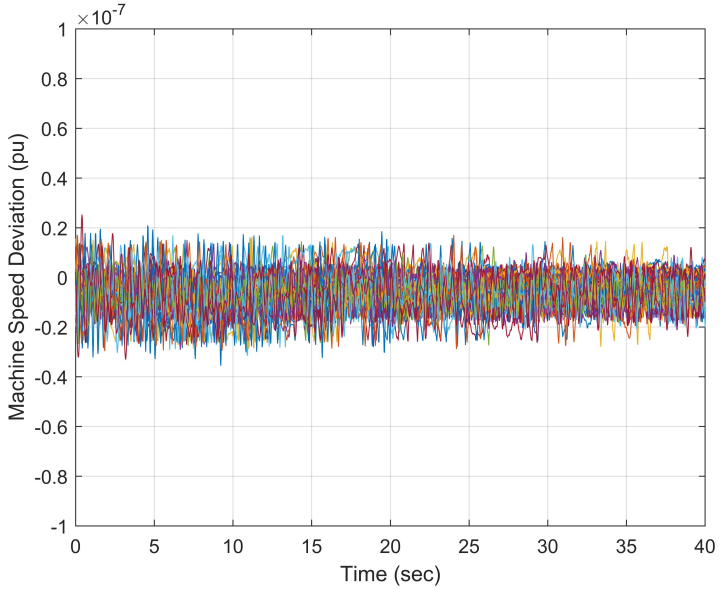


Figure 2.9: Machine speed deviation without disturbance.

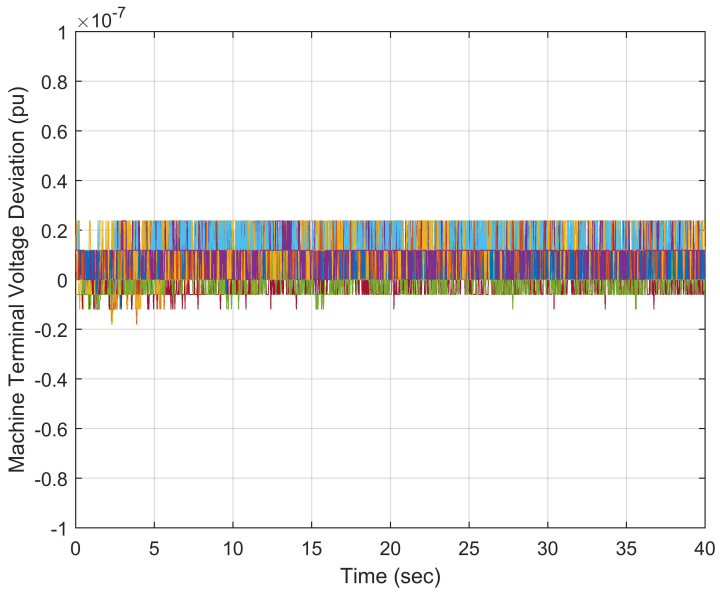


Figure 2.10: Machine terminal voltage deviation without disturbance.

2.4.2 Generator Trip Events

Case 1: Generator Trip at Bus 102 in the Western Region

A machine at bus 102 in the western region is tripped. The generation capacity of this unit is 1,684 MW. This gas turbine unit is tripped after five seconds and the system response is presented in Figure 2.11 and Figure 2.12 for frequency and voltage magnitudes, respectively, for different buses at the three main operating regions: WOA (Makkah bus), EOA (Gazlan bus), and COA (Riyadh bus). The system frequency is shown to have dropped no less than 59.55 Hz before it damped out within 15 seconds. Since Makkah bus (101) is very close to the tripped machine bus, its frequency took slightly more time to damp out than the other two frequency responses. The voltage magnitude at Makkah bus (101) dropped to 0.98 pu while the voltage drop at the other two regions did not reach 0.99 pu.

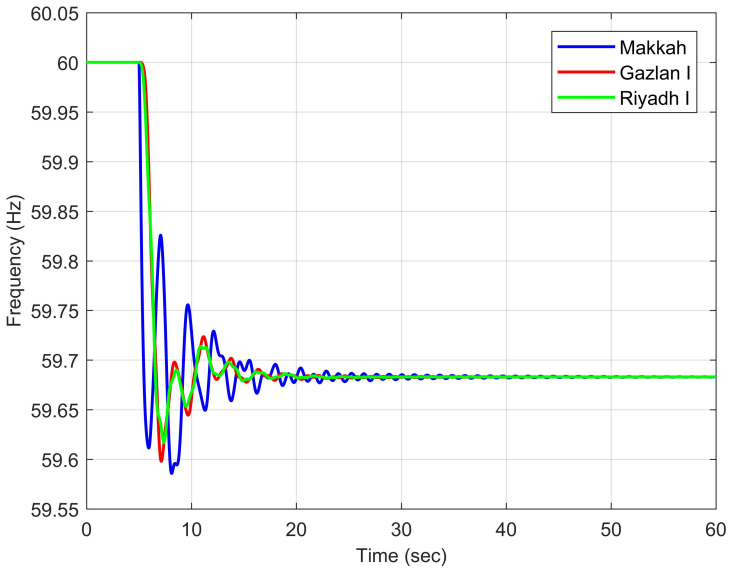


Figure 2.11: The frequency response after generator trip at bus 102.

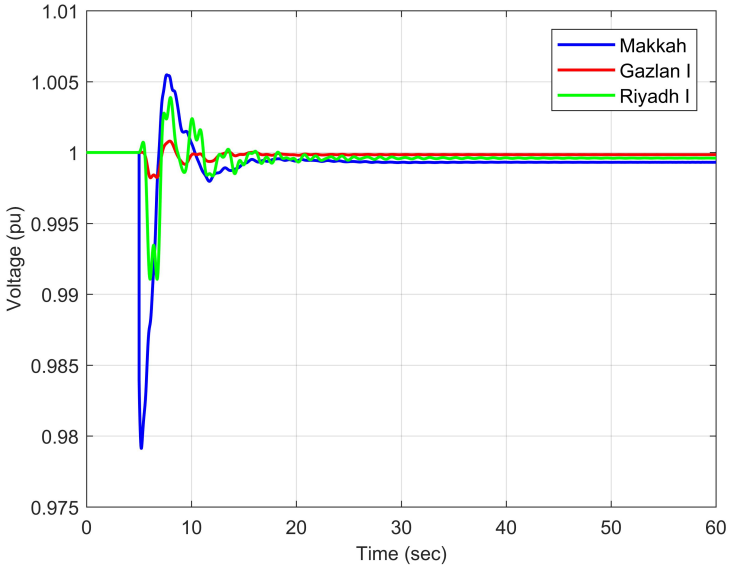


Figure 2.12: The voltage response after generator trip at bus 102.

Case 2: Generator Trip at Bus 211 in the Eastern Region

The second case is similar to the preceding case; however, the machine is tripped in the eastern region at bus 211. This tripped unit generated 885 MW and 109 Mvar at the time of disconnection. Figure 2.13 shows the system frequency response at three different measurement locations in the three operating areas. The frequency dipped to reach 59.77 Hz, then it damped out in less than 30 seconds. The voltage response, as shown in Figure 2.14, oscillated between 1.006 and 0.996 pu after tripping the generator before it reverted back to its nominal value around 1.0 pu.

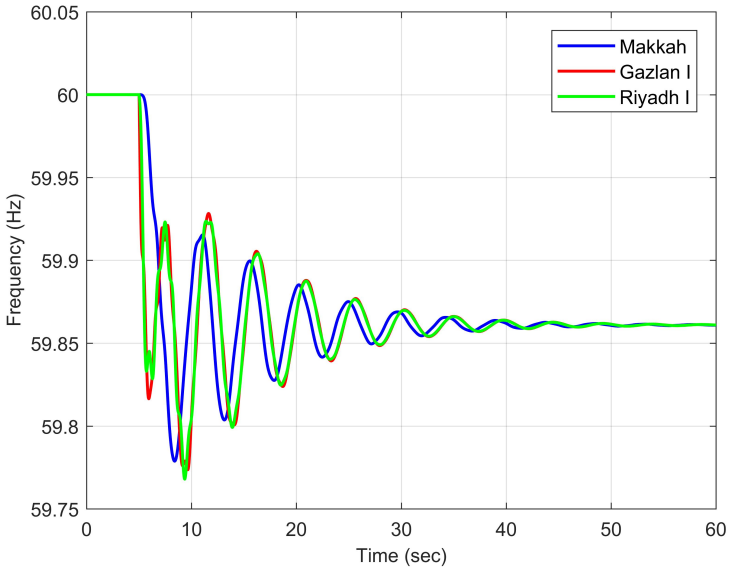


Figure 2.13: The frequency response after generator trip at bus 211.

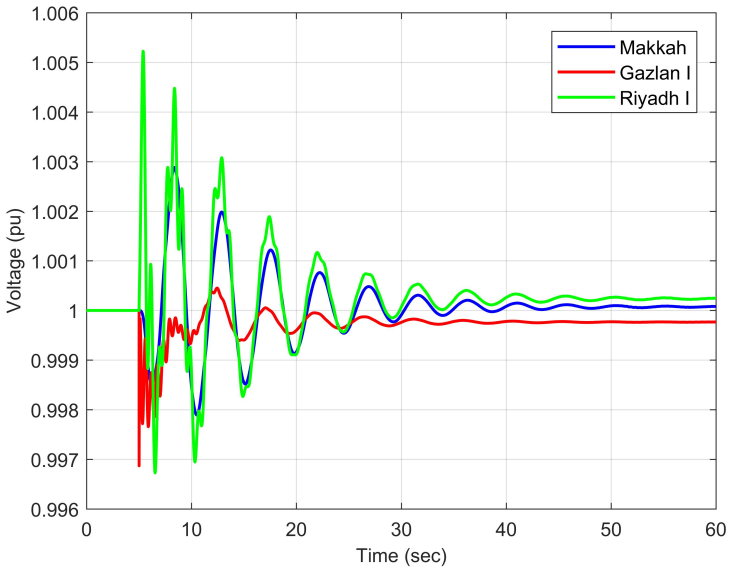


Figure 2.14: The voltage response after generator trip at bus 211.

Case 3: Generator Trip at Bus 309 in the Central Region

Another machine trip case has been studied in the central region. A gas turbine unit at bus 309 that generates 860 MW is tripped. It is noted that the frequency response dropped to 59.8 Hz as shown in Figure 2.15. On the other hand, the voltage response at bus 301, in COA, dipped to 0.985 pu after the fault, then it came back to its stable point as shown in Figure 2.16.

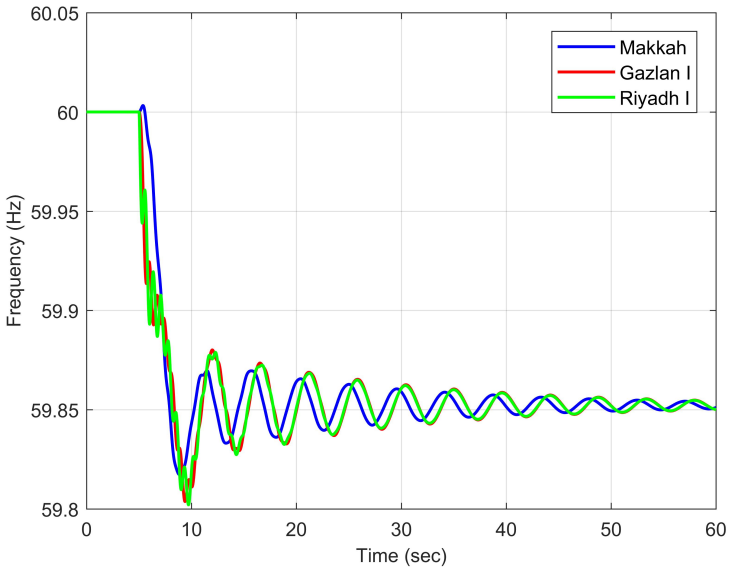


Figure 2.15: The frequency response after generator trip at bus 309.

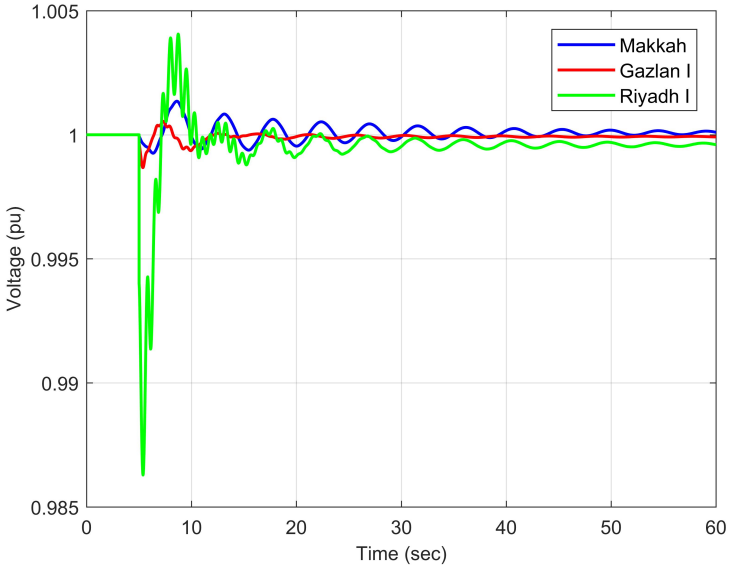


Figure 2.16: The voltage response after generator trip at bus 309.

2.4.3 Load Shedding Events

Case 1: Load Shedding at Bus 119 in the Western Region

The second scenario is to disconnect loads at certain buses. A 655 MW load at bus 119 in the western operating area is shed after five seconds. The frequency responses of different buses are depicted in Figure 2.17. It can be observed that the frequency slightly increased to reach 60.164 Hz before it damped out within 15 seconds. Figure 2.18 shows the voltage responses of the same buses after the load disconnection. It can be seen from the plot that the voltage at Makkah bus oscillated between 1.03 to 0.97 pu while the voltage responses of the other two buses: Riyadh-1 and Gazlan-1 softly oscillated before returning to 1.0 pu within a short period of time.

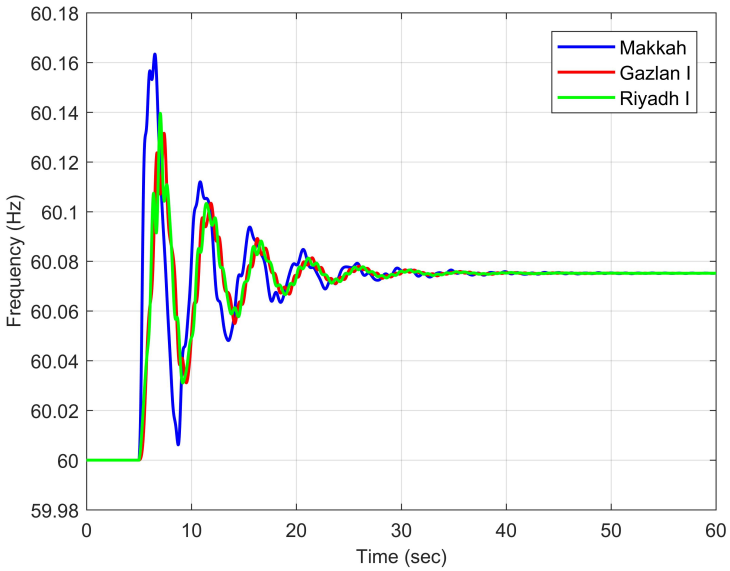


Figure 2.17: The frequency response after load shedding at bus 119.

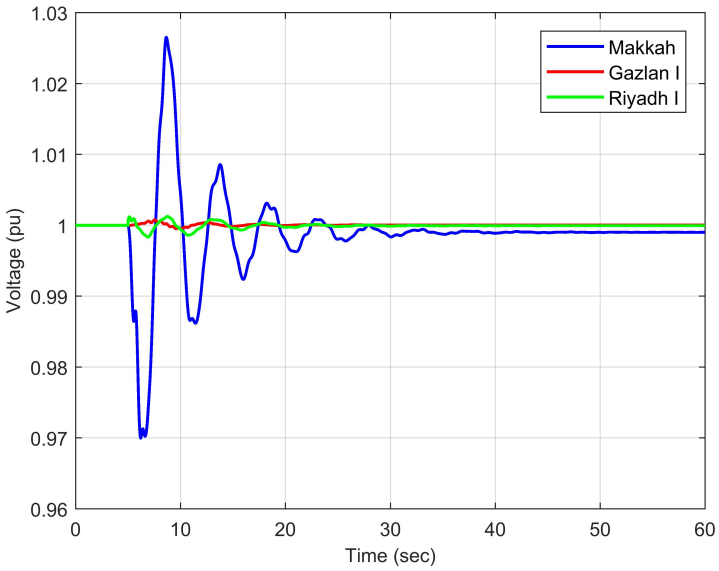


Figure 2.18: The voltage response after load shedding at bus 119.

Case 2: Load Shedding Bus 201 in the Eastern Region

In the second case, a load of 1,140 MW at bus 201, in the eastern region, is tripped and the results are shown in the Figure 2.19 and Figure 2.20 for frequency and voltage magnitudes, respectively. Similar to the previous case, the frequency responses at all selected buses increased to reach about 60.20 Hz. The voltage of Riyadh-1 bus spiked to 1.015 pu, then it settled back within a deviation of 0.0012 pu. The voltage of Gazlan-I bus increased momentarily to less than 1.008 pu after the load shedding while Makkah bus voltage returned to its original value in less than five seconds.

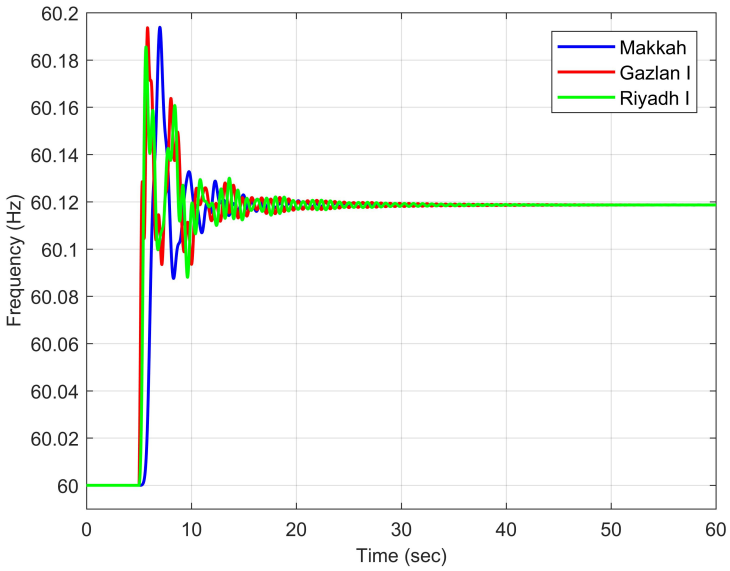


Figure 2.19: The frequency response after load shedding at bus 201.

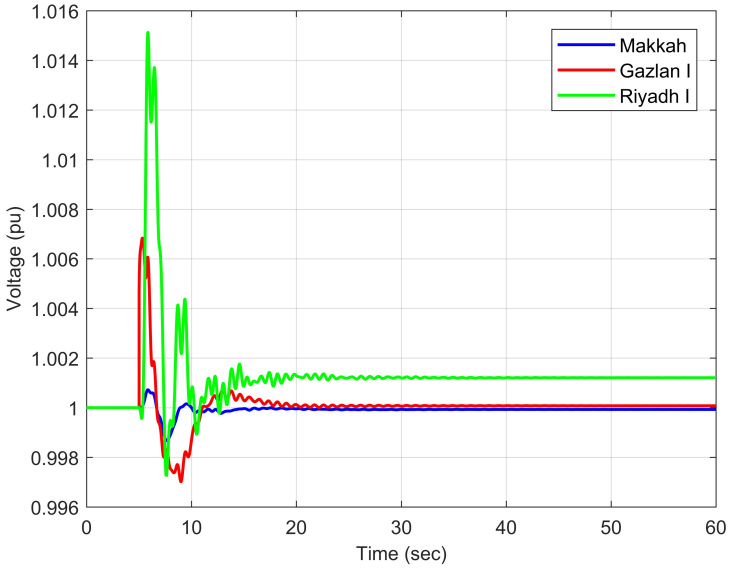


Figure 2.20: The voltage response after load shedding at bus 201.

Case 3: Load Shedding at Bus 308 in the Central Region

A load that consumes 1,329 MW and 437 Mvar at bus 308 in the central region is tripped. The event initialization time is five seconds. As shown in Figure 2.21, the frequency responses of the three selected buses increased to reach 60.24 Hz. Then, these frequency signals damped out in less than 10 seconds. Figure 2.22 shows the voltage response of the system during this load shedding event. The voltage response at Riyadh-1 bus reached 1.018 pu, then started small oscillations before it completely died out at 20 seconds. The voltage responses at the western and the eastern buses slightly oscillated for a moment then reverted back to the nominal voltage magnitude.

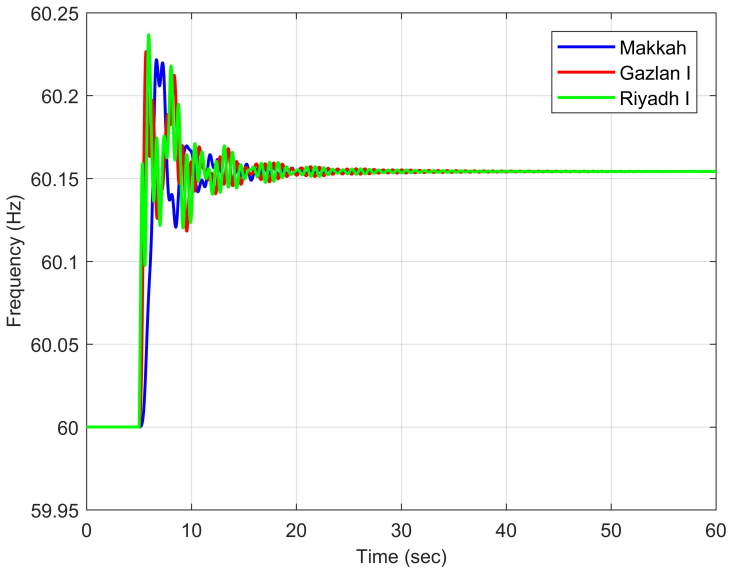


Figure 2.21: The frequency response after load shedding at bus 308.

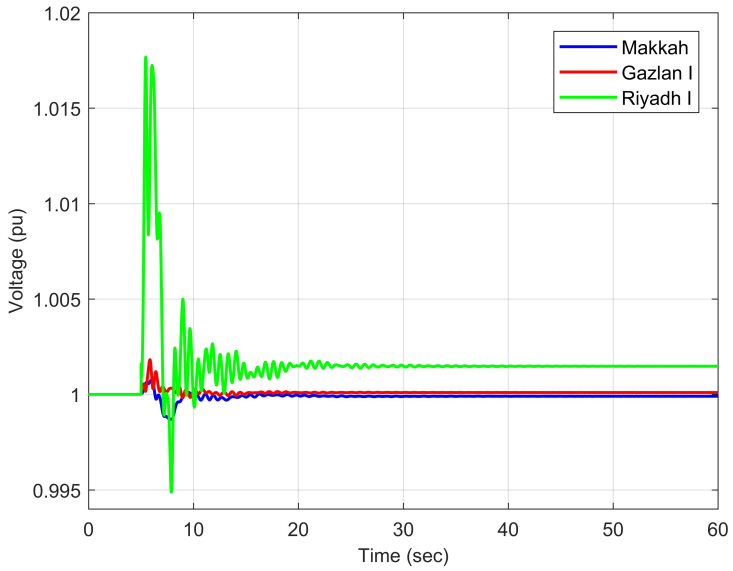


Figure 2.22: The voltage response after load shedding at bus 308.

2.4.4 Line Trip Events

Case 1: Line Trip between Buses 102-122 in the Western Region

A transmission line between bus 102 and bus 122 in the WOA is tripped after five seconds. This transmission line carried 316 MW during the fault. The simulation results of the frequency and voltage responses are shown in Figure 2.23 and Figure 2.24, respectively. Since this transmission line carried only smaller MW amount, tripping the line had a slight impact on both frequency and voltage responses of the system. The frequency encountered a small oscillation that slightly changed the stable point. Voltage, on the other hand, fluctuated between 0.997-1.002 pu for Riyadh-1 bus while Gazlan I bus showed unobserved oscillations because there is no direct connection between the EOA, where Gazlan I bus is located, and the WOA.

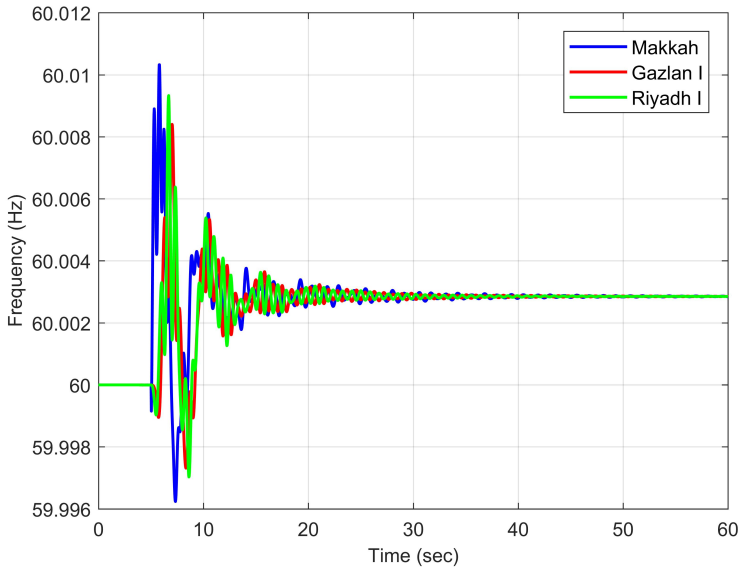


Figure 2.23: The frequency response after tripping the line between 102 and 122.

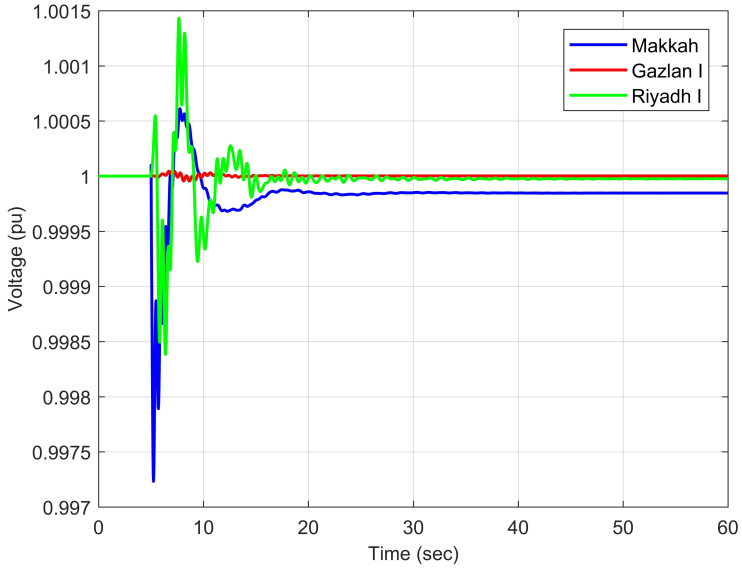


Figure 2.24: The voltage response after tripping the line between 102 and 122.

Case 2: Line Trip between Bus 108 in WOA and Bus 406 in SOA

The western operating area is connected to the southern area through two tie lines that transfer up to 300 MW. During the steady state condition, the first transmission line (Branch 1) transfers about 158 MW between buses 105 and 401 whereas the second line (Branch 2) transfers 122 MW between buses 108 and 406. That means the WOA is exporting roughly 280 MW to the SOA. In this event scenario, branch 1 is dropped after five seconds. The frequency responses at all three areas oscillated with smaller amplitudes and damped out in less than 10 seconds as shown in Figure 2.25. A similar fashion happened to the voltage profile of the same buses as depicted in Figure 2.26. As can be seen in Figure 2.27, the delivered power on the second branch increased to about 280 MW after disconnecting the first branch to keep the same transfer level as before the disturbance.

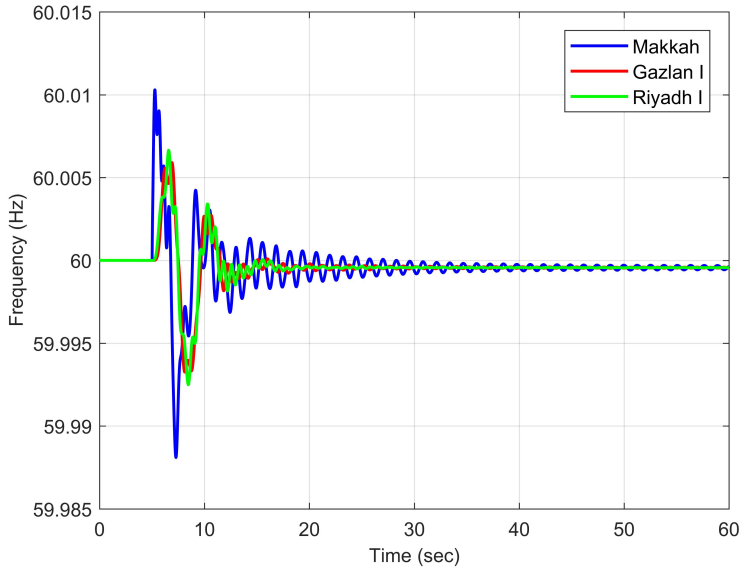


Figure 2.25: The frequency response after tripping the line between 108 and 406.

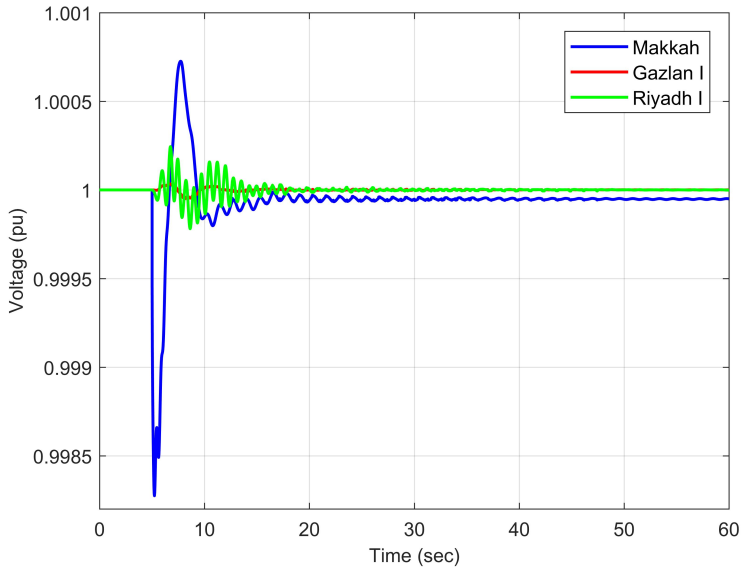


Figure 2.26: The voltage response after tripping the line between 108 and 406.

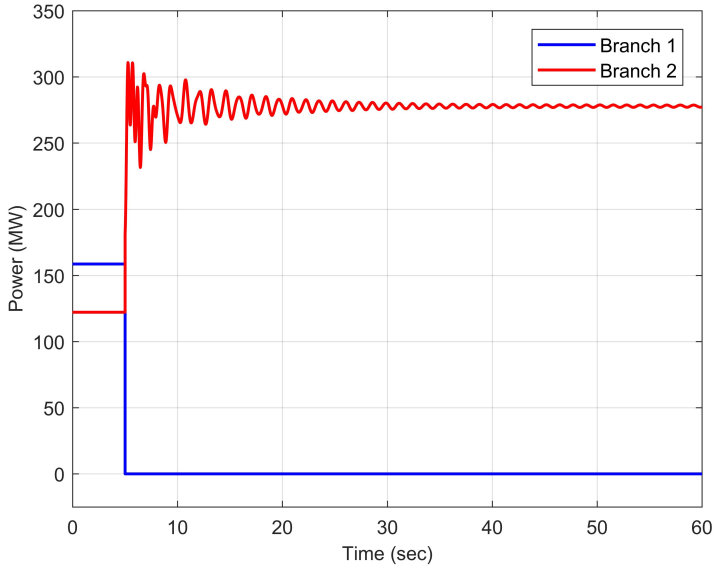


Figure 2.27: The power flow at the lines connecting WOA and SOA.

Case 3: Line Trip between Bus 211 in EOA and Bus 306 in COA

As previously stated, the eastern operating region is exporting about 4,000 MW power to the central operating region via two double circuit lines with voltage levels of 230 kV and 380 kV. In the Saudi model and after running the power flow, the following tie transmission lines are connecting the EOA with COA:

1. Branch 1 delivers 812 MW from bus 211 to bus 306.
2. Branch 2 delivers 1,266 MW from bus 215 to bus 301.
3. Branch 3 delivers 1,080 MW from bus 217 to bus 313.
4. Branch 4 delivers 1,080 MW from bus 217 to bus 313.

In this case, branch 2 that carries the highest power amount is tripped. The simulation results of the system frequency and voltage responses at different locations in the grid are shown in Figure 2.28 and Figure 2.29, respectively. The frequency responses oscillated to reach 60.13 Hz while the voltage profile of Riyadh-1 bus in COA highly fluctuated between 1.008 and 0.985 pu when the disturbance took place after five seconds. The voltage responses at all buses recovered within a very short period of time. After disconnecting branch number 2, the entire delivered power to COA was redistributed among the other three healthy transmission lines. Branch 1 carried additional 280 MW while each of branch 3 and branch 4 transferred additional 508 MW to COA to keep on the same MW amount being transferred before the disturbance occurred. This can be seen in Figure 2.30.

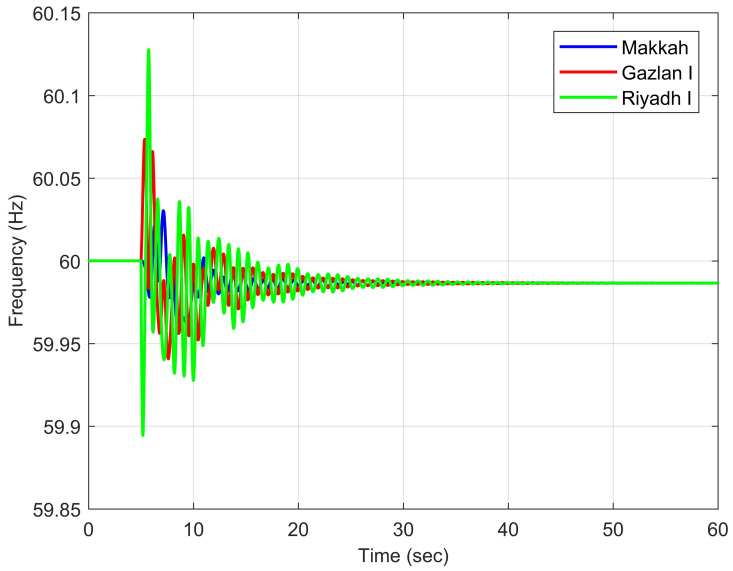


Figure 2.28: The frequency response after tripping the line between 215 and 301.

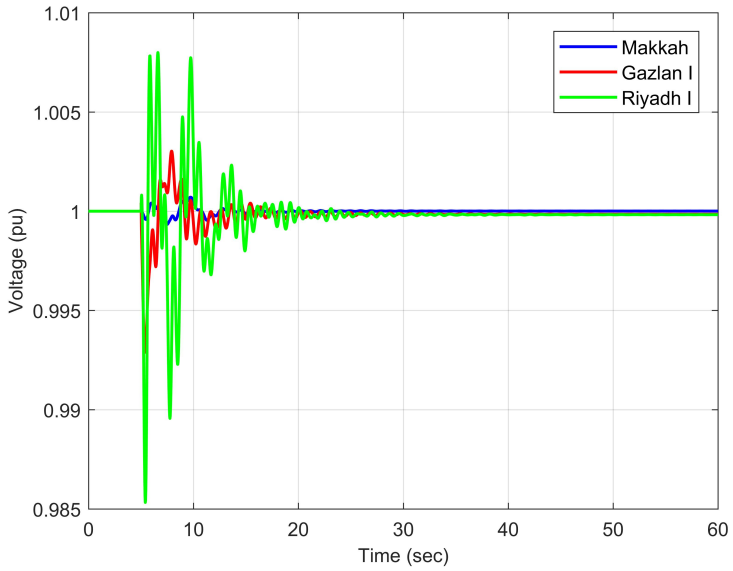


Figure 2.29: The voltage response after tripping the line between 215 and 301.

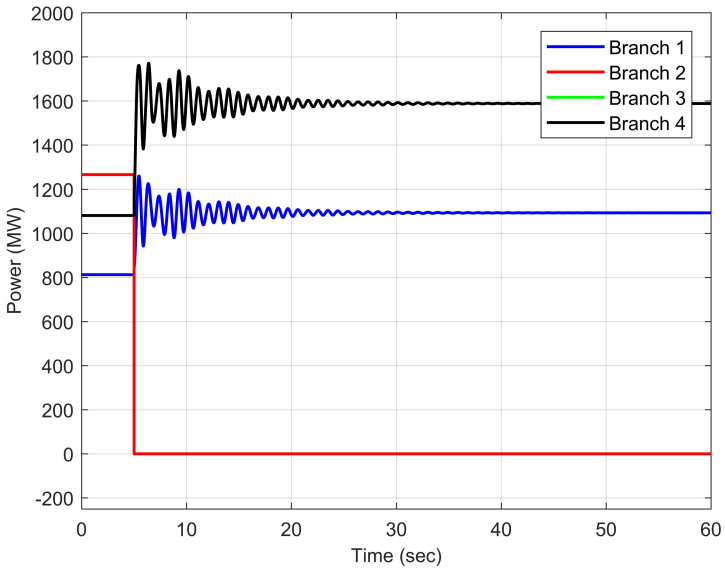


Figure 2.30: The power flow at the lines connecting EOA and COA.

2.5 Dynamic Model Validation of the Saudi Grid

Model validation is important to ensure the reliability of the power system and to assess its dynamic performance. This section presents the dynamic model validation of the Saudi national grid. Simulated frequency responses are modified and validated to match the measurements gathered by the frequency monitoring network (FNET/GridEye). The objective of this section is to have a system model that can reasonably match the output of the real system.

Three main components are needed to be studied in order to validate a specific dynamic model of a power system: load flow model, system dynamic representation, and field measurements. The power flow results should be agreed with those obtained from the real system and the dynamic model accuracy should be validated for converged solution and reasonable simulation precision [18].

2.5.1 The Frequency Monitoring Network (FNET)

Wide-area measurement systems (WAMS) make it easier to monitor and control the power system and to understand the status of the electric network in real-time. The Frequency Monitoring Network (FNET), which was invented in 2001 by Virginia Tech and started in 2004, is an online frequency monitoring network. It measures three electrical quantities from a single phase voltage outlet at a distribution system. They are frequency, voltage magnitude and voltage angle. Mainly FNET is composed of two main parts: GPS-time synchronized frequency disturbance recorders (FDRs) and an information management system (IMS). The FDRs are single-phase phasor measurement units (PMUs) that can measure voltage angle, voltage amplitude, and compute frequency from low voltage (110V) outlets while the IMS collects and stores data and provides real-time applications and web services [19].

The measured quantities are attached with GPS timestamp, and then sent over the web to a central processing server, which simultaneously analyzes and archives these data and shows them in a real-time portal [20]. Many FDRs are distributed in the United States and all over the world. Generally, they are installed at various places, such as power stations, substations, offices, and private sites. FDR locations can be simply changed when required [21].

FNET makes it easy to use phasor measurement system with stable performance and more accurate dynamic measurements that can be installed at a minimum cost. All of these advantages can be attributed to the fact that the FDRs are plugged into low voltage sockets (120/220V) [22]. The FNET provides a variety of situational awareness applications such frequency monitoring interface, event trigger, event location and visualization, interarea

oscillation trigger, modal analysis, and islanding and line trip detection. It also provides valuable data about electromechanical transients, generation-load relation, load shedding, and oscillations [19]. The main structure of the FNET system is shown in Figure 2.31.

Such monitoring system is essential to allow more investigation on the Saudi national grid and to expand the understanding of the system dynamics and control characteristics. However, phasor measurement units have not been deployed in Saudi Arabia yet. Therefore, a frequency disturbance recorder (FDR) has been installed in June 2016 in the eastern part of Saudi Arabia to obtain dynamic measurements of the Saudi power grid. The physical location of the installed FDR is shown in Figure 2.32 with the suggested locations of two additional FDRs to be installed later in Saudi Arabia. The installed FDR (Sa1191) has coordinates of 50.0527^0E and 26.5807^0N. Information about the Saudi frequency is captured from 220V/60 Hz wall socket. Several events have been captured since July 2016 with the event detection threshold of 10 mHz/sec.

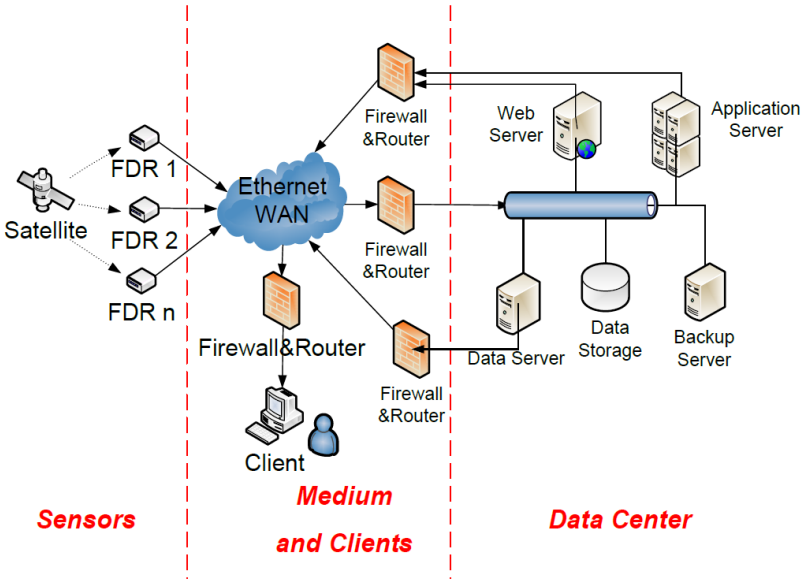


Figure 2.31: The main structure of the FNET system [23].



Figure 2.32: FDR locations for the proposed FNET system in Saudi Arabia.

2.5.2 Model Validation Cases

In order to validate the Saudi model against the actual system response, two actual events are chosen to be studied in the developed Saudi dynamic model. The fact that the information about these events is unknown in greater details makes it challenging to replicate these events exactly. If more detailed data from the Saudi Electricity Company about those events are provided, this Saudi model would show more accurate representation of the actual system.

Based on many model validation cases, it is usual that the initial validation model run may not be similar to the observed real event due to several reasons such as initial power flow conditions, mistaken sequence of events, or inaccurate model data [24].

Case 1: 333 MW Generation Trip, 2016.08.09, 14:20:48 UTC

The frequency recording taken on this date is shown in Figure 2.33. A 333.4 MW generation is tripped in the central region and the associated frequency decline is 69.20 mHz. The locations of the disturbance and the measurement are plotted in Figure 2.34.

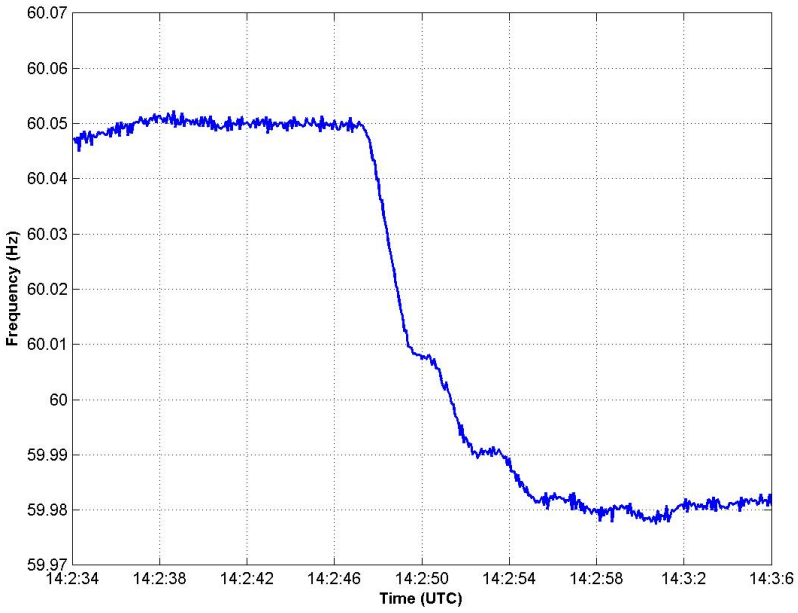


Figure 2.33: FDR frequency response after generator trip in August 2016.

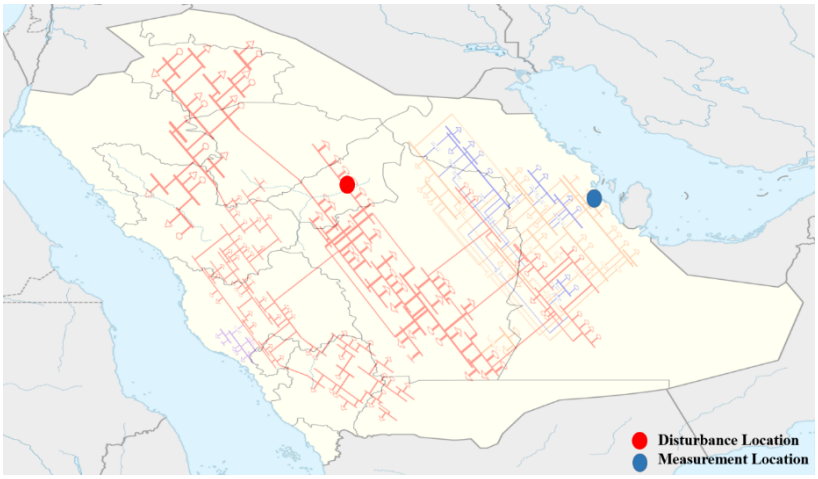


Figure 2.34: Case 1 locations.

Using the FDR recording and the tripped MW amount, the system frequency response characteristic β has been calculated. The parameter β is a constant that describes the relation between the generation loss and the change in the frequency and its unit is MW/mHz [25]. An empirical method to calculate the governing response β is presented in [21]. In addition to knowing the tripped MW amount, this method uses frequency deviation Δf to determine the frequency characteristics for the Saudi model from the following equation [21]:

$$\Delta P = \beta \Delta f \tag{2.1}$$

where ΔP is a power mismatch during the event.

In this case, as shown on Figure 2.33, the pre-disturbance frequency f_{pre} is 60.0498 Hz while the post-disturbance frequency f_{post} is 59.9856 Hz. Therefore, the average frequency deviation Δf is 64.1854 mHz. Using the above equation, with knowing the amount of the tripped generation capacity that is 333.4 MW, yield that the frequency response characteristic β is 5.195 MW/mHz.

In [26], Chen et al. summarized the main critical factors effecting the frequency response: system inertia constant, turbine-governor, and load compositions. These factors should be taken into consideration when it comes to utilizing frequency measurement to validate a system model. As stated in [26], the influence of the last two factors on the first swing of the frequency response is not high, compared with the impact of the inertia constant. Therefore, the inertia constant H is the only factor that is being changed in order to correct the simulation response to match the measurement output. In fact, the Saudi model has less

portion of turbine-governors as only 29.95% generation capacity (18.237 GW) is attached to active governors. Also, the loads in this system are modeled as a constant MVA type.

The case 1 event has been simulated in PSS®E by disconnecting a gas unit at bus 301 that generated a similar amount at a time of the disturbance. The comparison between measurement and simulation at the observation location, which is at bus 218, is presented in Figure 2.35. This plot reveals an obvious frequency difference between actual measurements and simulation results. Also, it shows that the slope of the frequency drop for the simulation response was not steeper enough like the measurement result.

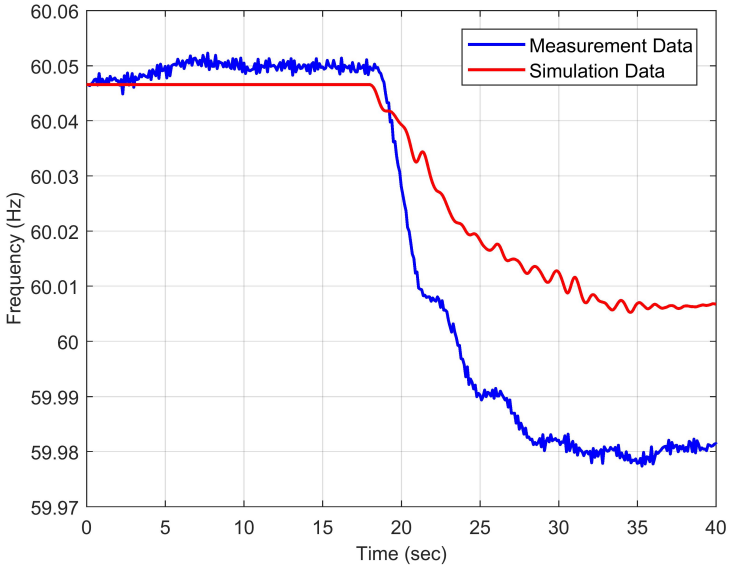


Figure 2.35: Simulation and measurement comparison of case 1 before the modification.

Therefore, the system inertia constant was decreased for all generators to about 50% of the original value. This resulted in a quite similar frequency response for both simulation results and measurements as shown in Figure 2.36. It can be noticed that the simulation frequency response resembled closely the real response after reducing the inertia constant.

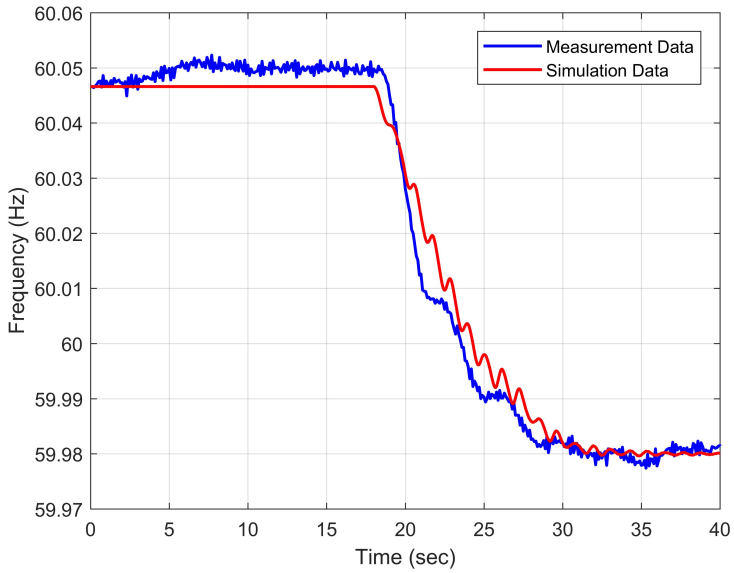


Figure 2.36: Simulation and measurement comparison of case 1 after the modification.

Case 2: 484 MW Generation Trip, 2016.07.23, 04:26:50 UTC

In this case, in July 2016 at 07:26 local time, about 483.5 MW generation was lost during a typical weekend. This resulted in a frequency drop from 60.05 to 59.945 Hz as shown in Figure 2.37. Figure 2.38 illustrates the disturbance location and the measurement unit location.

In this case, the pre-disturbance and the post-disturbance frequencies are 60.0456 Hz and 59.9519 Hz, respectively. As a result of this, the average frequency deviation is 93.7342 mHz. In addition to that, the total amount of the tripped generation capacity is 483.56 MW would lead to the frequency response characteristic β of 5.159 MW/mHz, which approximately equals that of the first case. Table 2.6 summaries the information about estimating the governing response β of the two selected cases. It can be observed that *Beta* value is somewhat lower compared to the values of β for EI and WECC as in [25]. This can be attributed to the smaller size of the Saudi grid compared to the US grid.

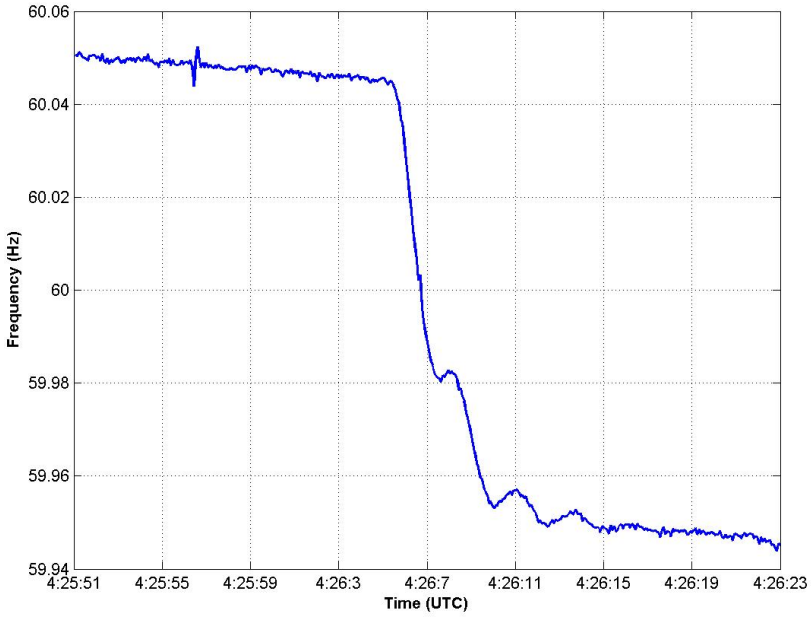


Figure 2.37: FDR frequency response after generator trip in July 2016.

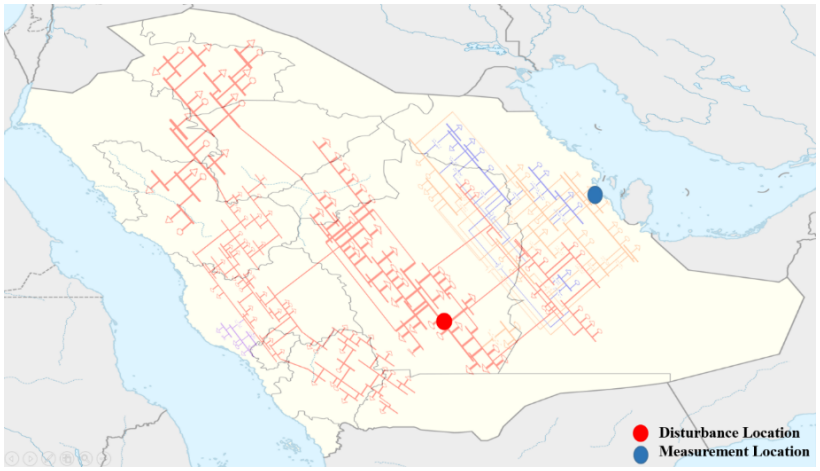


Figure 2.38: Case 2 locations.

Table 2.6: Summary of the disturbances events.

Parameter	**Case 1**	**Case 2**
Date & Time (UTC)	08/09/2016 14:20	07/23/2016 04:26
Pre-disturbance frequency (f_{pre})	60.0498 Hz	60.0456 Hz
Post-disturbance frequency (f_{post})	59.9856 Hz	59.9519 Hz
Average frequency deviation (Δf)	64.1854 mHz	93.7342 mHz
MW tripped	333.4 MW	483.5 MW
Governing response (β)	5.195 MW/mHz	5.159 MW/mHz

The second disturbance is replicated by dropping one unit at bus 308. The unit delivered the same active power when the disconnection occurred that resulted in a frequency decline. The measurement is taken at bus 218 corresponding to the FDR location. In Figure 2.39, the frequency behaviors of the original Saudi model simulation and the measurement are illustrated in a window of 40 seconds. It can be noticed that the simulation frequency response was not accurate enough to predict the real response shape for this disturbance.

As a result, the simulation model was adjusted by reducing the inertia constant values of all 70 machines uniformly in the model such that the simulation result can get closer to the real measurement. The comparison results are shown in Figure 2.40. It is observed that the simulation frequency behavior matched approximately the actual response from the FDR measurements.

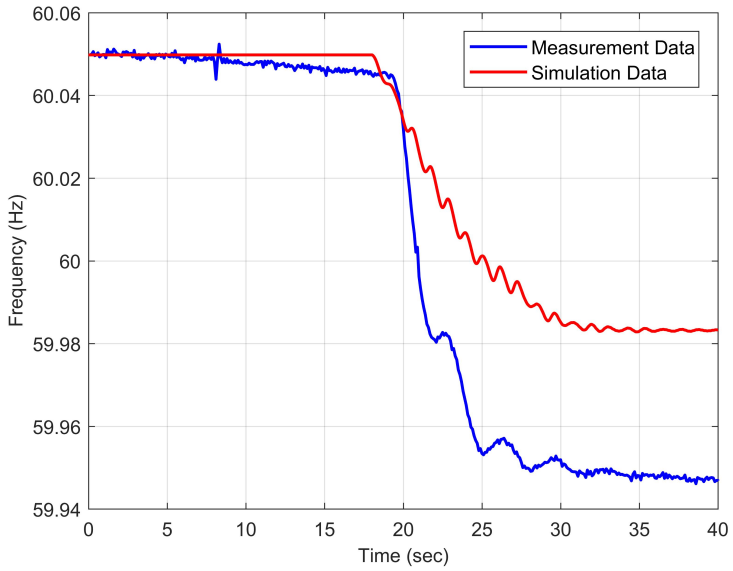


Figure 2.39: Simulation and measurement comparison of case 2 before the modification.

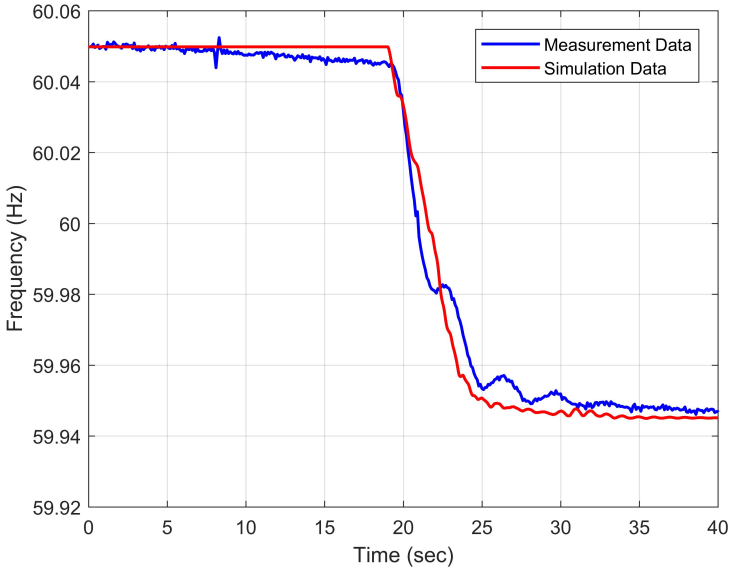


Figure 2.40: Simulation and measurement comparison of case 2 after the modification.

2.6 Summary

This chapter develops a dynamic model of the Saudi power grid based on the actual real data available from public domains. The dynamic model is built and tested against several disturbances at different parts of the system to confirm the stability of the developed model. Simulation results shown in this chapter prove that the system is dynamically stable.

In order to take this dynamic model into the next level, the model is validated with the actual recordings from the frequency disturbance recorder (FDR). Two actual events are replicated and the model is modified to show a close match between the actual and the simulated results. The observed β values for the two cases are found to be exactly the same.

As demonstrated in the validation cases, the developed Saudi model built in PSS®E after adjustment can reasonably predict the disturbances' behavior, considering the lack of precise information about the actual events. In fact, the response could be tracked much better if the exact locations and the amount of the real incidents are available. Finally, the apparent similarity of the frequency shapes between the model simulation and the measurement data increases the confidence in the developed model resembling the Saudi national grid to estimate the accurate real system behavior. It ensures that the results of the built model would highly agree with the measurements.

Chapter 3

VOLTAGE STABILITY ASSESSMENT OF THE SAUDI POWER GRID

3.1 Introduction

Voltage stability concerns increase with the increase of the complexity of a power grid. When a power system operates close to voltage stability limits, the voltage collapse incidents might occur in the network as a result of a small disturbance or even tiny increase in the loading level. As the system becomes heavily loaded, voltage instability becomes a major concern that requires immediate preventive actions. Over the last decades, the Saudi power grid has experienced a significant growth in load demand, which indicates that the system may operate near its voltage stability limits. This stimulates the interest to investigate the voltage stability status of the Saudi network using static analysis techniques.

Based on the available literature review, there is no literature analyzing the status of the voltage stability of the Saudi power grid; therefore, it is advantageous to conduct a comprehensive study to check the voltage stability condition of the Saudi grid, and to implement effective ways that can help reduce the likelihood of voltage instability occurrence. This chapter evaluates the voltage stability status of the Saudi Arabian power grid using static analyses approaches. The most probable voltage weakest buses and the overloaded transmission lines in the grid must be identified and their closeness to voltage instability point should be assessed. Further analyses are required to be done on the critical buses to study the effect of the reactive power compensation. Suitable measures to improve voltage profile are needed to be applied.

3.2 Voltage Stability

Mainly, power system stability involves three broad categories: rotor angle stability that includes small signal stability and transient stability, frequency stability, and voltage stability. Voltage stability is described as the ability of a power grid to sustain adequate and controllable voltage levels at all areas in the network during normal operation as well as after disturbances occurrence [27]. A power grid is stated to be voltage unstable if voltage at a certain bus is uncontrolled and decreases sharply after a disturbance. On the other hand, the system is claimed to be stable if the voltage levels are within normal operating predetermined ranges during normal operation as well as after disturbances [28].

It has been proved that the voltage stability is a local problem associated with the loads; however, its consequences may impact the entire network leading to a widespread blackout.

Voltage instability is known to be an issue for the heavily loaded networks as a small increase in loads would advance the system into the voltage collapse phase [29]. The main reason of voltage stability problems comes from the shortage of the reactive power reserve in the grid. This reserve is required to keep voltage levels within normal limits, especially when there is a heavy increase in the load demand [30, 31]. In fact, if increasing reactive power results in increasing bus voltage, the network can be declared as voltage stable system; otherwise, the system is voltage unstable. There are other factors contributing to voltage instability such as voltage sources are either weak or far from load centers, increase in the load demands, disturbances like generators or line trips, and reaching reactive power limits of generators or other reactive power support devices [27, 28, 31].

Regarding analysis techniques, voltage stability is sorted into large and small disturbances voltage stability. Large disturbance voltage stability is mainly examined by using nonlinear dynamic analysis methods while the other one can be investigated using static analysis techniques [27]. Further, voltage stability is considered a load driven issue that can be categorized into: long-term voltage stability dealing with slower acting components with a time that may last for few minutes and short-term voltage stability that includes quick acting load equipment with a time scale in the order of several seconds [31, 32].

Voltage instability issues have been linked to various major blackout events that happened in different parts of the world such as New York Power Pool disturbance in 1977, Japanese system disturbance in 1987, and the major USA blackout in the northeast in 2003 [27, 31]. Detailed information about these blackouts can be found in [33, 34, 35].

In the Saudi power grid, many blackouts occurred due to voltage stability problems. For instance, one of the major causes of the latest blackout event in Taif city in the western

region in June 2014 is the abnormal high voltage that damaged some electrical equipment leading to a power loss of 783 MW. Another example is when the system voltage collapsed in August 2003, leading to a total blackout in the southern region causing a total loss of load (595 MW). Furthermore, severe voltage dip was experienced in the system causing the largest power plant in the western region to drop out, then a series of generating units tripped resulting in loss of 7,143 MW on August 8th, 2003 [36].

3.2.1 Reactive Power Compensation Devices

Since it is not practical to transmit reactive power over long distances to control voltage levels, Mvars should be produced at different locations in the system depending on the demand conditions and the network topology. For the short-term voltage instability, under-voltage or selective load shedding relays can be used to control the voltage. However, when it comes to long-term voltage instability, reactive power support should be installed close to the load center to regulate the system voltage [31]. Therefore, there are several reactive power compensators that differ in their operating characteristics and costs. Practically, most of them can simultaneously generate and absorb reactive power to control voltage profile at heavy and light loads. Examples of these compensators to control voltages profiles: synchronous generators, synchronous condensers, shunt and series capacitors, shunt reactors, under load tap changing transformers (ULTC), and fixable AC transmission systems (FACTS). Some of these devices are briefly reviewed next.

Synchronous generators can supply or consume reactive power depending mainly on the generator excitation. When an alternator operates in overexcited mode, it generates reactive

power, while in under-excited mode, it absorbs reactive power with leading current. The automatic voltage regulator (AVR) adjusts excitation to control the output of reactive power to keep a constant armature voltage. Generally, a synchronous generator requires a minimum amount of reactive power to support the transmission of the generated active power [37].

Synchronous condensers, sometimes called synchronous compensators, run without prime movers and they are not attached to a mechanical loads. They provide reactive power without producing active power; however, they take active power from the power network to compensate for the loss. Depending on field excitation, these condensers can operate as continuous variable Vars sources or sinks. The main feature of the synchronous condensers is that they do not depend on the system voltage to produce the required Vars [27, 38].

As their name implies, shunt and series capacitors are connected in parallel or in series to the transmission lines to control the voltage level by injecting more reactive power to the network. Shunt capacitors, which are widely implemented in the distribution systems, are used to compensate for the line losses and to minimize the voltage drops by supplying reactive power. They can be connected to a grid as fixed or switched shunt capacitors with different sizes and cheap prices. The main drawback of shunt capacitors is that their reactive power production depends on the system voltage squared, which means the Mvar values are significantly reduced at lower voltage levels [27]. On the other hand, series capacitors, which are self-regulating, are used to reduce the inductive reactance of the power lines to increase the maximum power transfer, which leads to increasing the reactive power [27]. It is worth mentioning that the combination of shunt and series capacitors would provide better Var compensation as well as voltage profile improvement.

Shunt reactors are desirable to absorb reactive power at lightly loaded buses to limit voltage rise. They can be connected either directly to the line or tertiary winding of transformers [38]. An application of shunt reactors is that they are used for EHV long transmission lines and short overhead lines when not connected to a strong system to resolve the "Ferranti" effect [27].

Overhead Lines can produce reactive power when the load is less than the surge impedance load (SIL) and can absorb reactive power if the load is greater than the SIL. In case of underground cables, the generated reactive power is usually higher than the absorbed reactive power because cables have high SIL due to a large capacitance. Thus, they are considered reactive power sources [38]. Usually, transformers operate as sinks of the reactive power due to the shunt magnetizing reactance and the series leakage inductance. The more current drawn from the system, the higher reactive power absorption by the transformers [38]. Loads can either absorb or generate reactive power depending on their characteristics. Industrial loads such as motors absorb reactive power whereas some consumers' loads like fluorescent lighting produce reactive power. So, industrial customers are required to install capacitor banks close to their load to improve the system power factor and decrease the drawn reactive power [38].

Recently, FACTS have been used extensively to control voltage levels by controlling the supplying, absorption, and flow of Vars in the grid. They can adjust the absorbed or produced reactive power automatically by adjusting the firing angle. There are different types of FACTS, including static Var compensator (SVC), static synchronous compensator (STATCOM), static synchronous series compensator (SSSC), and thyristor-controlled series

capacitor (TCSC) that can be attached to different locations in the system. They also differ in their characteristics, types of connection, cost, and contribution to the grid.

3.2.2 Impact of Load Characteristics

Although modeling power loads is a complicated task, it is one of the key factors effecting the analysis of voltage stability because it mainly depends on the amount of load current. Therefore, voltage stability studies require modeling the loads and how they respond to voltage variations [27, 39]. In general, electrical loads are categorized into constant power, constant current, or constant impedance. However, in a large power grid, it is not easy to characterize the load type due to the complications of the large grid. Thus, for voltage stability studies, a typical exponential load characteristic usually has the following general description at any bus in the grid [27, 31]:

$$P = P_0(\frac{V}{V_0})^a \tag{3.1}$$

$$Q = Q_0(\frac{V}{V_0})^b \tag{3.2}$$

where P_0, Q_0, and V_0 are the initial operating conditions of real power, reactive power, and voltage, respectively of a selected bus. The exponents a and b values determine the type of the load, e.g., both values can be 0.0, 1.0, or 2.0 to represent constant power, constant current, and constant impedance load types, respectively. Different values of these exponents for several load types can be found in [40].

ZIP or polynomial load model is a special case of the exponential model that includes both constant impedance 'Z', constant current 'I' and constant power 'P' [27]. Mainly, modeling power system loads can be either component based or measurement based load model. [27, 41]. The first method is called 'bottom-up' approach. Its mechanism works by lumping loads based on their types such as residential, commercial, industrial, and agriculture. Then, pre-determined values of each load type are used. In the measurement based approach, based on the field measurements, the load behavior is estimated by using identification methods at various voltage levels. The main drawback of this method is that it cannot predict the load characteristics when the voltage sharply decreases.

The residential load will be reduced when the voltage decreases, which results in transmission line Vars loss. Moreover, the load may be disconnected when the system voltage sharply decreases below a certain threshold while the industrial loads might be changed a little as a result of voltage drop [27, 31]. Due to the load components uncertainty and the lack of information about the load models in the Saudi power grid, a typical static P-Q load model has been used in the developed Saudi power model.

3.3 Voltage Stability Analysis

Many voltage stability issues can be efficiently examined by steady state analysis techniques because the dynamics of the system effecting voltage stability are typically quite slow [27]. This section presents literature reviews on some static analysis approaches used in this study to assess the status of the voltage stability of the Saudi grid and to pinpoint the voltage weakest nodes and lines. These approaches are V-Q sensitivity analysis and Q-V modal

analysis to identify the weak buses and overloaded lines, and PV and QV curves methods to estimate the active and reactive power margins.

3.3.1 *V-Q* Sensitivity Analysis

According to [27], the power flow problem can be formed as:

$$\begin{bmatrix} \Delta P \\ \Delta Q \end{bmatrix} = \begin{bmatrix} J_{P\theta} & J_{PV} \\ J_{Q\theta} & J_{QV} \end{bmatrix} \begin{bmatrix} \Delta\theta \\ \Delta V \end{bmatrix} \tag{3.3}$$

where ΔP, ΔQ, $\Delta\theta$ and ΔV for a certain bus are small changes in active power, reactive power, voltage phase angle, and voltage amplitude, respectively. The 2×2 matrix is the Jacobian matrix that shows the relation between power flow and the changes in bus voltages. To solve the above equation based on the reactive power, by letting $\Delta P = 0$, the reduced Jacobian matrix of the network is expressed as:

$$J_R = \left[J_{QV} - J_{Q\theta} J_{P\theta}^{-1} J_{PV}\right] \tag{3.4}$$

The reduced Jacobian matrix elements $[J_R]$ are employed to find the sensitivity between bus voltage changes and the reactive power. This means that the V-Q sensitivity of a certain load bus is the corresponding diagonal element of the matrix $[J_R]^{-1}$. A positive sensitivity value at a bus is associated with a stable operation while the negative sensitivity is a signal of an unstable system. For stable operation, the stability is reduced as the sensitivity value gets larger whereas the opposite applies for the unstable operation, i.e., very unstable operation has a smaller negative sensitivity value [27].

3.3.2 *Q-V* Modal Analysis

The eigenvalues and eigenvectors of the reduced Jacobian matrix $[J_R]$ are used to get insight about the voltage stability condition of the grid. $[J_R]$ can be reformulated as:

$$J_R = \xi \Lambda \eta \tag{3.5}$$

where ξ and η are the eigenvectors matrices (right and left) while Λ is the diagonal eigenvalues matrix of $[J_R]$ [27].

$$\Delta V = \xi \Lambda^{-1} \eta \Delta Q = \sum_i \frac{\xi_i \eta_i}{\lambda_i} \Delta Q \tag{3.6}$$

where ξ_i and η_i are the right eigenvector column and the left eigenvector row of the i^{th} model, respectively. The i^{th} mode of the Q-V profile can be represented by the eigenvalue λ_i and its associated right and left eigenvectors. Therefore, for the i^{th} mode:

$$V_i = \frac{1}{\lambda_i} q_i \tag{3.7}$$

The magnitudes of eigenvalues determine the degree of stability of different modes in the system. A positive λ_i implies the stability of the system whereas the system is voltage unstable when λ_i is negative. However, if λ_i is zero, any variation in the reactive power would cause unbounded deviations in the modal voltage, which leads to the i^{th} modal voltage collapse. Practically, it is unnecessary to find more than ten of the smallest eigenvalues to determine all critical modes [27]. It is important to notice that the reduced Jacobian matrix

$[J_R]$ can be symmetric if the line resistances are ignored. This means that both right and left eigenvectors are real and equal [27].

Bus Participation Factors

Bus participation factors are used to identify which bus contributes heavily in a certain mode of instability. This can help identify the weakest buses associated with each mode. The participation of bus n in the i$^{\text{th}}$ mode is determined by:

$$P_{ni} = \xi_{ni}\eta_{ni} \tag{3.8}$$

A high magnitude of P_{ni} at bus n for the i$^{\text{th}}$ mode indicates that this bus is near voltage instability in the i$^{\text{th}}$ mode [27]. The localized modes, which happen when a load is attached to a strong system via lengthy lines, have a small number of buses with high participation factors. Conversely, the non-localized modes, which occur when an area in a large system is loaded with less reactive power support, have buses with small participation factors [27].

Branch Participation Factors

The relative participation of branch j in the i$^{\text{th}}$ mode can be found by using the following participation factor:

$$P_{ji} = \frac{\Delta Q_{loss} for\ branch\ j}{Maximum Q_{loss} for\ all\ branches} \tag{3.9}$$

Branch participation factors identify which branch absorbs more Vars as a result of change in reactive load for each mode. The branches that have larger participation factors can be indicated as either weak branches or heavily loaded lines [27].

3.3.3 *PV* Curve Analysis

The *'PV'* (Power-Voltage) curve shows how the voltage of a critical node varies as the load level changes. It displays the voltage collapse point "knee point" for load buses in the power network. This point is known as the maximum power transfer capability that limits the amount of power being transferred to a bus. Voltage instability happens at the nose of the curve where the voltage is dramatically decreased when the transferred power slightly increases.

As an indication of instability, standards power flow solution cannot converge beyond the knee point. Therefore, operation near or at the voltage collapse point would make the system susceptible to a large-scale blackout. A satisfactory operating condition requires a sufficient "power margin" that must be maintained to accommodate for unpredictable disturbances. The active power margin for a specific bus can be calculated as the distance between the real power at the operating point and the maximum transfer real power at the collapse point. The PV curve of a load bus can be created by gradually increasing the real power and running a series of power flow solutions until the limit of the power transfer is reached [27, 28, 42].

3.3.4 *QV* Curve Analysis

QV curve shows the relation between the voltage magnitude and the reactive power injection at the same bus. It is used to determine how much of reactive power reserve exists for a given operating condition and to determine how much further injected reactive power is needed to keep the voltage level within acceptable ranges. QV curve could be utilized as an index of voltage stability as the sensitivity gets large close to the nose point of the curve [27].

For unstable operation, the voltage amplitude is reduced sharply as more reactive power is injected.

Figure 3.1 shows a standard QV curve. As illustrated, the region on the left of the critical point is an unstable region whereas the stable area is represented by the region on the right side of the critical point. This curve can be created by applying a factious Q source at the bus where the curve needs to be obtained and gradually increasing the reactive power and performing power flow solution until the voltage stability limit is reached where dQ/dV is zero. The reactive power reserve is calculated as the difference between the amount of reactive power at the current operating point and the nose point of the QV curve. As long as the critical point is below the horizontal line, representing bus voltage, the system has adequate Mvar reserve. Unlike PV curves, QV curves are easier to be obtained using only a standard power flow solution because it will solve at and beyond the nose point of the QV curve [43].

3.4 Saudi Grid Voltage Stability Analysis

The developed Saudi grid model described in chapter 2 is used to evaluate the status of the voltage stability of the Saudi power system. The aforementioned static voltage stability analysis techniques are utilized to estimate the grid proximity to voltage stability limits.

After conducting the power flow simulation using the Newton Raphson method with five iterations for the base operating condition, the power flow Jacobian matrix is determined and reduced as described in section 3.3.1.

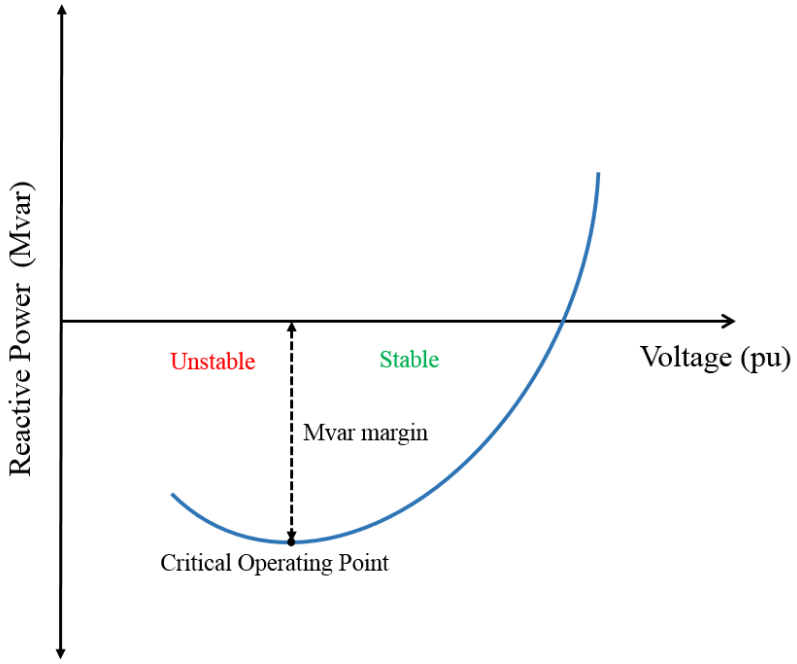


Figure 3.1: Standard QV curve.

3.4.1 Load Bus Voltages

After the power flow is converged, five load buses have voltage levels that are closer to the lower limit of the voltage recommended limits, based on the criteria that the voltage level must be within ±5% of the nominal [44]. Table 3.1 gives the buses with the lowest voltage magnitudes. It can be noticed that the first buses with the lowest voltage magnitudes are located in the central area, which has the highest load demand (∼ 19 GW). Followed by two buses (bus 221 and bus 222) in the eastern area that consumes about 17.8 GW load. Finally, the last bus is located at the edge of the western area, which demands about 27% of the total Saudi load. The remaining two operating areas (southern and northern) do not consume much load as their overall consumption does not exceed 12%; therefore, their load buses operating voltage levels are always maintained within a range of 1.0097 and 0.9862 pu.

Table 3.1: Load buses voltage magnitudes.

Bus number	**Voltage magnitude**
303	0.9526
306	0.9605
221	0.9625
222	0.9659
105	0.9682

3.4.2 *V-Q* Sensitivity Analysis

The *V-Q* sensitivity of the load buses in the Saudi grid is investigated by calculating the sensitivity factors. As mentioned earlier, the sensitivity factors are the diagonal entries of the inverse of the reduced Jacobian matrix $[J_R]$. Table 3.2 indicates that the group of buses with the highest sensitivity factors involves the buses with lower voltage magnitudes defined in the previous table. This points that the first buses with the highest *V-Q* sensitivity are the weakest buses in the system, in terms of voltage stability, and their operating points might be closer to the stability limit of their QV curves.

3.4.3 *Q-V* Modal Analysis

The reduced Jacobian matrix $[J_R]$ characteristics are determined in order to examine the system voltage stability modes. Table 3.3 summarizes the least five eigenvalues of $[J_R]$ for the base operating case. It has been found that the smallest eigenvalue of $[J_R]$ is $\lambda_0 = 0.49$ in the mode 28, which is the critical mode that is just close to voltage stability limit.

Table 3.2: Highest V-Q sensitivities.

Bus number	***V*-*Q* sensitivity**
303	0.867
306	0.680
221	0.658
105	0.615
222	0.609
106	0.591
311	0.328

Table 3.3: The smallest eigenvalues of $[J_R]$.

Mode	**Eigenvalue**
28	0.490
40	1.054
31	1.135
41	2.057
32	2.429

This implies that the system is vulnerable to voltage instability during this mode and it will become zero at the bifurcation point.

Bus and Branches Participation Factors

Only the critical mode in the network (mode 28) is used to analyze the participation factors of buses and branches in the Saudi grid. The nodes that have large participation factors for the least stable mode with eigenvalue of $\lambda_0 = 0.49$ are given in Table 3.4 while the remaining buses have close to zero factors. These buses with the highest participation factors are the same buses with minimum voltage values and maximum sensitivity factors; hence, they can be declared as the voltage weakest buses in the Saudi model.

Table 3.4: Highest bus participation factors.

Bus number	**Participation factor**
303	0.3872
221	0.3143
306	0.2566
222	0.1747
105	0.1582

The areas around the voltage weakest buses that are determined in the previous tables are analyzed to check the transmission lines that might be heavily loaded and could create voltage stability problems. To achieve this, the Mvar losses at each branch are computed and then taken as ratio to the maximum reactive power loss in the critical mode. Table 3.5 shows the branches with the highest participation factors for the least stable mode.

These branches consume too much reactive power and could be easily overloaded leading to disastrous voltage collapse. Figure 3.2 shows the identified buses and branches with the highest participation factors.

3.4.4 Active Power and Reactive Power Margins

Table 3.6 gives the active and reactive power margins, expressed in percentage for the load buses with the smallest margins to the stability limits.

The PV curve for bus 303, which has the smallest active power margin is presented in Figure 3.3 to show how the voltage profile varies with the loading level. Figure 3.4 shows the QV curves of the five selected buses with the highest V-Q sensitivities. It can be noticed that buses in the central and the eastern operating areas have the minimum active and reactive power margins among the weakest load buses.

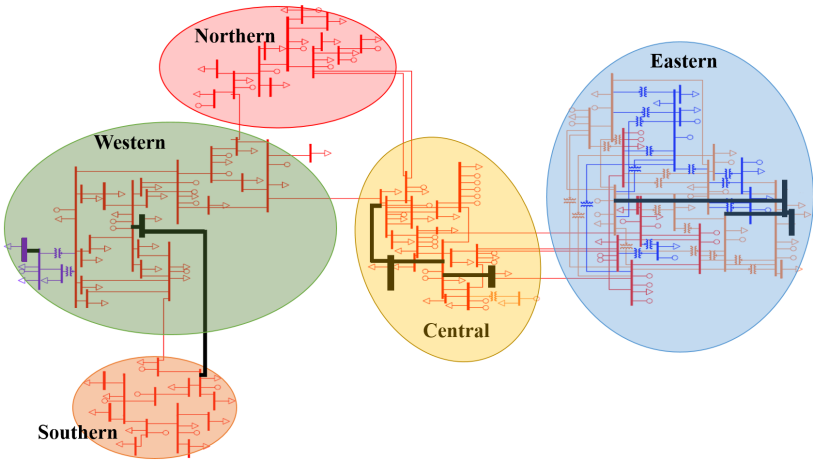


Figure 3.2: Buses and branches with the highest participation factors.

Table 3.5: Highest branch participation factors.

Branch	**Participation factor**
302-303	1.0000
221-222	0.8623
302-306	0.8226
303-311	0.7517
102-105	0.6625
105-401	0.5335
213-222	0.2320
210-222	0.1749
103-106	0.1563

Table 3.6: Active and reactive power margins.

Bus number	**Active power margin (%)**	**Reactive power margin (%)**
303	43.2892	10.3126
306	46.6085	20.1071
221	59.0380	24.5946
222	65.0743	46.0024
105	68.6296	54.2151

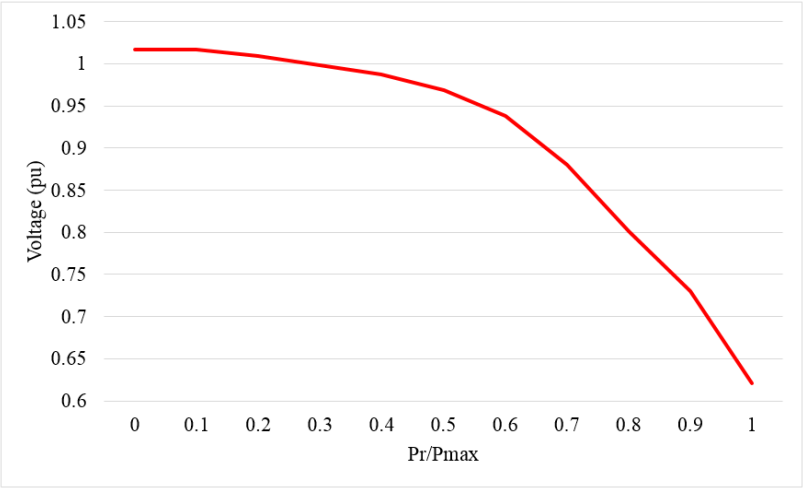


Figure 3.3: PV curve for bus 303.

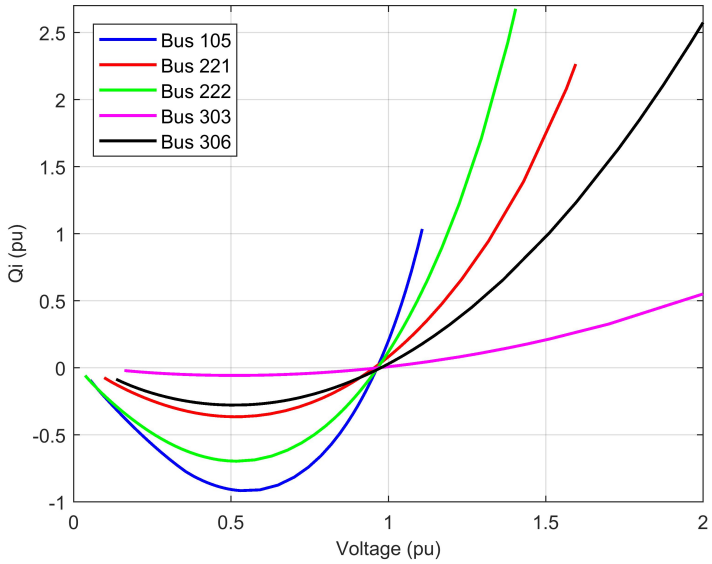


Figure 3.4: QV curves for all five load buses.

3.4.5 Remedial Measures

It is clear from the above results that the five buses (303, 306, 221, 222, and 105) are identified as the critical buses in the Saudi model in terms of voltage stability. Therefore, it is required to prevent voltage collapse by adding mitigation measures close or at these critical buses.

Since the branches identified in Table 3.5 contribute the most of reactive power loss in the system, the first suggested remedy is to insert series capacitors to reduce the series reactance between the generation and load buses [31, 45]. Therefore, 50% series compensation is added to the branches adjacent to the buses 303 and 306 while 25% of series compensation is added to the branches connecting to buses 221 and 222. Additionally, 5-10% of series capacitors are injected to the identified weak lines in the western area. After inserting all these capacitors, the voltage profile and the active as well the reactive power margins for all five buses are improved as shown in Table 3.7. Figure 3.5 presents a comparison of the PV curves before and after inserting the series capacitors into the overloaded branches in the grid for bus 303. The QV curves of the critical buses after implementing the suggested remedial action are shown in Figure 3.6.

Table 3.7: Critical buses profiles after adding series capacitors.

Bus number	**Voltage level (pu)**	**Active power margin (%)**	**Reactive power margin (%)**
303	0.9576	51.837	17.3970
306	0.9699	56.790	34.8397
221	0.9707	68.892	40.1055
222	0.9713	70.559	61.0305
105	0.9704	75.770	72.7970

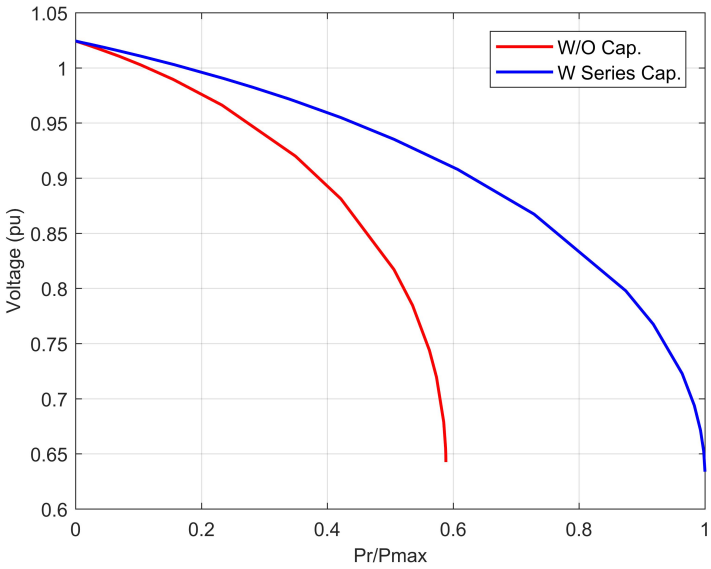


Figure 3.5: PV curves for bus 303 after inserting series capacitors.

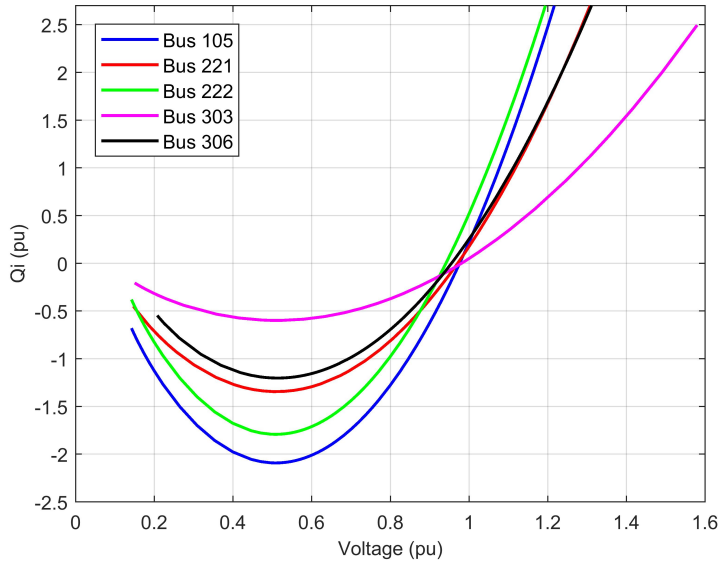


Figure 3.6: QV curves for all five load buses after inserting series capacitors.

As shown in Table 3.7, the voltage profiles of some buses are still close to the lower limit of the permissible voltage level; thus, another recommended and economic practice is to add adequate shunt capacitors near these buses to improve the voltage stability margins. To achieve this, shunt capacitors with different ratings are connected to the five buses based on their voltage magnitudes in order to get the most reasonable voltage magnitudes within the standards enforced by the SEC (0.95 to 1.05 pu) [44]. Table 3.8 shows the rating of Mvars added to each bus and the voltage profiles improvement after this remedial measure is being applied.

Table 3.8: Final critical buses profiles.

Bus number	**Added Mvars (Mvar)**	**Voltage level (pu)**
303	200	0.9759
306	150	0.9777
221	50	0.9802
222	30	0.9799
105	5	0.9750

3.5 Summary

Saudi power grid is expanding in its size and demand, which makes voltage stability analysis becomes a major need to avoid voltage collapse. This chapter examines the voltage stability status of the Saudi grid using static analysis methods. It has been observed that five load buses are identified as critical buses where voltage instability phenomenon might occur.

Both V-Q sensitivity and Q-V modal analysis provide useful practical information about the voltage weakest buses and most stressed branches while PV and QV curves estimate the system proximity to voltage collapse limits.

Practical remedial actions have been suggested in this chapter to improve the voltage stability situation and to increase the distance to the collapse points for the critical buses as the loading levels and the grid topology change. This study considers the most economical way to resolve voltage stability issues by adding series and shunt capacitors to the vulnerable buses to counter the voltage instability. This has been done to prevent the cascading blackouts in the Saudi grid. Additional studies are recommended to compare the impact and the cost of different reactive power support applications. Finally, further voltage stability studies are required to be conducted with more realistic representation of the load models to assess the stability status with higher accuracy.

Chapter 4

SOLAR ENERGY IN SAUDI ARABIA

4.1 Introduction

Saudi Arabia is conveniently bounded by the latitudes of 31^0N and 17.5^0N and longitudes of 50^0E and 36.6^0E. This strategic location lies in the center of the "sunbelt" zone that receives a huge amount of sunshine. Thus, Saudi Arabia experiences high average annual solar radiation of approximately 2,200 kWh/m^2 and larger sunlight duration with an average of 8.89 hours, especially in the summer season [46, 47]. This ideal geographical area leads Saudi Arabia to be one of the countries that have high natural potential for taking an advantage of the solar energy. In addition to the vast flat desert land and the clear skies around the year, this location enables Saudi Arabia to be the world leader in producing and exporting solar energy [48, 49]. The total amount of solar energy received in the country is ten times the Saudi electrical requirements and it is sufficient to electrify Saudi Arabia for more than

70 years [50, 51]. The average daily solar radiation in Saudi Arabia is about 250 W/m^2, compared with the solar radiation in Europe and other North America countries that only receive between 100-200 W/m^2 daily. Moreover, Saudi Arabia is part of the rainless region in the Middle East that has a very high rate of sunny days over the course of the year for most parts of the country [52].

Saudi Arabia is the world's leading petroleum supplier as it supplies more than 13% of the world oil, more than any other country in the Organization of the Petroleum Exporting Countries (OPEC) [52]. However, the oil production and prices have already started to decrease in the last years due to different factors. This decline mode in the oil production, coupled with the extraordinary increase in electrical demand and the high potential of solar energy, qualifies Saudi Arabia to become the main candidate to utilize solar energy in its energy resources [52]. Since the electricity production in Saudi Arabia heavily relies on nonrenewable fossil fuel based power units to supply the increasing demand, more than half of the produced oil and natural gas are used as fuels for these conventional generation plants [47]. Even though Saudi Arabia consumes that much of oil, fuel cost is not an issue for the Saudi government. However, it is interested in taking the lead in harvesting solar energy and using oil revenue to create convenient infrastructure for the penetration of solar panels. If Saudi Arabia utilizes the significant potential of the solar energy efficiently, the power can be exported to the neighboring countries and even to some European countries that receive less amount of sunlight with affordable cost [52].

Based on the aforementioned facts, the Saudi government launched King Abdullah City for Atomic and Renewable Energy (K.A.CARE) in 2010. Its main goal is to create sustainable energy for the Saudi future by incorporating reliable renewable energy resources

supported by modern local industries. K.A.CARE plans to resolve load growth and the environment challenges by supporting the existing traditional power plants with a mixture of sustainable resources that can generate clean power without pollution. The plan targets to have 41 GW of solar capacity, including 16 GW photovoltaic (PV) and 25 GW consecrated solar power (CSP), to be installed by 2030 [5]. Later on, this plan was postponed to 2040 and the Saudi Vision 2030 has changed the plan as it targets generating 9.5 GW of renewable energy by 2030 [53, 54]. Even though this plan mysteriously does not provide enough details, most of this energy would be met through solar technology.

4.2 Advantages of Solar Penetration in the Saudi Grid

It is well-known that generating electricity from the traditional power plants is the main reason for polluting the environment with the emission of harmful gases like Carbon Oxides (CO & CO_2), Nitrogen Oxides (NO, NO_2 & N_2O), and Sulfur Oxides (SO_2 & SO_3) [55]. As a matter of fact, all power plants in the SEC are fossil fuel based power plants because the price of the fuel is very cheap in Saudi Arabia, and the SEC takes the low cost as an incentive to not consider renewable energy sources yet [50]. This results in enormous increasing in greenhouses gases emissions, which leads Saudi Arabia to be ranked as the 14^{th} among the countries that have high CO_2 emissions from burning fuel to generate electricity, according to International Energy Agency (IEA) [56]. CO_2 emission levels reached more than 200 million metric tons in 2010 and it is expected to increase to approximately 1,380 million metric tons in 2030, considering the electricity generation will still be from the conventional power units [50]. This increase in green houses gases has detrimental impacts on human health as well

as the global warming. To overcome all of these issues, a switch to renewable solar energy sources is vital for countries that have great potential of solar energy. Using solar plants as an alternative to generate electricity has several benefits for Saudi Arabia environment as it reduces the air emission, minimizes the atmospheric pollution, improves public health, and has less noise pollution. Saudi government plan to install 41 GW of solar energy will save more than 1,000 million barrels of oil and reduce 410 million tons of CO_2 per year [52].

In General, compared with the traditional power plants, the solar energy has tremendous features as it has no fuel cost and requires fairly less maintenance [50, 57]. Therefore, solar generation has been increasing worldwide in the last decade. The low operational cost, the fast development in the solar industry, and the increased efficiency have made the solar power is the most promising renewable energy to replace the coal-fired power plants. It becomes easy to deploy and integrate solar plants [58]. Moreover, the price of oil is increasing, which results in increasing the cost of electricity production from oil based power units. Therefore, Saudi Arabia has significant economic incentives as its consumption of petroleum and natural gas will be much reduced when replacing some of the existing conventional power plants with photovoltaic and consecrated solar power units [48, 59]. Consequently, extra oil and natural gas could be exported and more revenue would be gained. Additionally, using solar power in the sparsely populated remote rural areas in the far north and south terrain regions of Saudi Arabia is important to avoid any extra cost of constructing new transmission lines and to reduce the transmission losses amount [47, 50]. Furthermore, country's expansion into solar energy would create more jobs for Saudi citizens.

Further, thanks to the abundant potential of sunshine, Saudi Arabia may exploit the solar energy that can help with shaving the peak demand from the national grid, especially, the

peak-load demand that is associated with the extensive use of air conditioner (AC) units that coincides with the maximum solar radiation in the summer season [60]. Hence, using solar energy in Saudi Arabia will assure both economic and environmentally friendly electricity generation [47].

On the other hand, Saudi Arabia usually goes through harsh and extreme environmental conditions that might impact the performance of the PV system. For example, dust may accumulate on the PV panels, which would reduce the efficiency by 10-20% [49, 50]. Also, as previously stated, Saudi Arabia receives less rain throughout the year that makes it difficult to naturally clean the accumulated dust and bring extra cost [61]. Moreover, the extreme high temperature, that reaches more than 50 ^{0}C during summer months, could result in lowering PV performance as voltage drops due to conversion efficiency [50, 62].

4.3 History of Solar Energy in Saudi Arabia

In 1960s, Saudi Arabia started the first solar project when a small photovoltaic beacon was installed at Madinah airport [48]. Since 1970s, the Energy Research Institute (ERI) at King Abdul Aziz City for Science and Technology (KACST) has started several solar research activities [59]. In 1977, Saudi Arabia cooperated with the United States to launch a joint solar energy program known as Solar Energy Research American Saudi (SOLERAS). Both the US Department of Energy and the Saudi government invested $50 million to this program [48]. One of the outcomes of this joint program was the "Solar Village" to supply energy to remote regions from solar power in 1980. The 350 kW photovoltaic Solar Village electrified two rural areas in the northwest of Riyadh that were not connected to the main power grid:

Al-Jubaila and Al-Uyaina, serving more than 3,000 citizens [48, 52]. This project was the largest solar project in its type during that time and the first independent solar project in the Middle East [47, 48]. It costed about $18 million to generate 1.0 to 1.5 MWh per day of energy [55]. The 'SOLERAS' program ended in 1997 after addressing the economic and technological difficulties of utilizing solar energy in the region [48].

Another collaborative international program was established with the Federal Republic of Germany in 1986 and finished in 1991. This program, which was called 'HYSOLAR', investigated and developed hydrogen production and utilization technologies [48].

Later on, another joint collaboration between the ERI and the National Research Energy Laboratory (NREL) in the U.S was established in 1994 and resulted in Saudi Atlas Project [63]. It focused mainly on the determination of the convenient locations to measure the solar radiation in Saudi Arabia. The project selected twelve locations throughout the country for the measurement stations that can measure the solar horizontal, direct beam, and diffuse radiation. The measurements are then sent to a central unit that calibrated the radiation data to get more accurate and reliable data [48].

In May 2010, at the King Abdullah University of Science and Technology (KAUST) in Thuwal in the western part of the country, two megawatts PV rooftop mounted array system was installed. The total number of installed panels is 9,300 that are distributed on the school roof with an area of 11,600 mi^2. It is estimated that this project can supply around 3,281 MWh and save 1,700 tons of CO_2 emissions per year. The cost of this rooftop project was more than $17 million [48, 55].

The first stand-alone solar power plant was built to electrify Farasan Island in the Red Sea in the southwest of Saudi Arabia. This power plant, which started operation in June

2011, has a capacity of 500 kWp and it covers an area of 7,700 square meters. The solar power plant cut off shipping about 28,000 barrels of diesel to the island to generate electricity using diesel power plants [47, 55]. It provides clean energy (864 MWh/year) to about 200 houses [54].

A 25 MW thermal power plant has been installed at Princess Noura University for Women (PNUW) in Riyadh in April 2012. The plant utilizes about 36,160 m^2 of large flat plate solar collectors to heat the water for the university students. Throughout the expected lifespan of this plant, it is estimated that 52 million liters of fossil fuel and 125,000 metric tons of CO_2 emission would be reduced [47]. Furthermore, a large solar parking project with a capacity of 10.5 MW has been constructed by Saudi Aramco to cover 4,500 parking space with an area of 200,000 m^2 of the North park of its headquarter in Dhahran in the eastern region of Saudi Arabia in 2012 [55]. About 120 thousand Copper Indium Selenide photovoltaic panels are used to provide shades and generate clean energy [47]. Another 200 kW rooftop PV project has been launched at King Abdullah Financial District (KAFD) in Riyadh in 2012. It can provide 330 MWh/year of energy using about 800 PV modules that cover an area of 1,300 m^2 [47, 54]. In 2013, a 3.5 MW solar park was built in King Abdullah Petroleum Studies and Research Center (KAPSARC) in Riyadh and a 4.5 MW solar farm was commissioned at King Abdulaziz International Airport in Jaddah [54]. There are several solar projects that are planned to be built in different cities in Saudi Arabia for different purposes: 10 MW at Khafji, 50 MW at Alaflaj, 50 MW at Jouf, 50 MW at Rafha, 550 MW at Duba, and 100 MW at Makkah [47, 54, 64].

Although the Saudi government has started pioneering initiatives in solar energy, the country still does not have considerable progress in the solar power industry. This can be

attributed to the lack of governments solar incentive programs and abundance of oil reserve and its relatively low cost. Yet, the entire solar energy capacity installed in Saudi Arabia is only 22 MW [59]. This number is relatively small comparing to the amount of sunshine received in the region. As a point of reference, the installed solar capacity in Germany is more than 40 GW while receiving only half of the solar radiation in Saudi Arabia [64].

4.4 Solar Irradiance in Saudi Arabia

According to [46, 48, 55], the daily global solar radiation in Saudi Arabia ranges from 4.5 kWh/m^2 in Tabuk in the northern region to 7.0 kWh/m^2 in Bishah in the southern area with an average radiation of 5.6 kWh/m^2. Since 1970, there have been 40 measurement stations throughout the country to collect data about the global solar radiation and the bright sunshine duration. Hepbasli and Alsuhaibani in [48] analyzed these data and observed that the solar radiation is higher in most of the southern cities while the northern cities received relatively low radiation. They found that the sunlight duration ranges from 7.4 to 9.4 hours. They also concluded that Bishah has the best location to install a solar power plant. In the middle of the summer season, the daily solar radiation reaches 7.09 kWh/m^2 whereas it could reach only 3.82 kWh/m^2 in the winter [49].

According to [65], the best ten cites for solar irradiance in Saudi Arabia are shown in Figure 4.1. As can be seen in the figure, these locations are distributed among three operating areas: western, central, and southern. The solar energy productivity is observed to be higher in both the northern and the southern regions of Saudi Arabia due to low average temperature in the north and high average solar radiation in the south [66]. Furthermore,

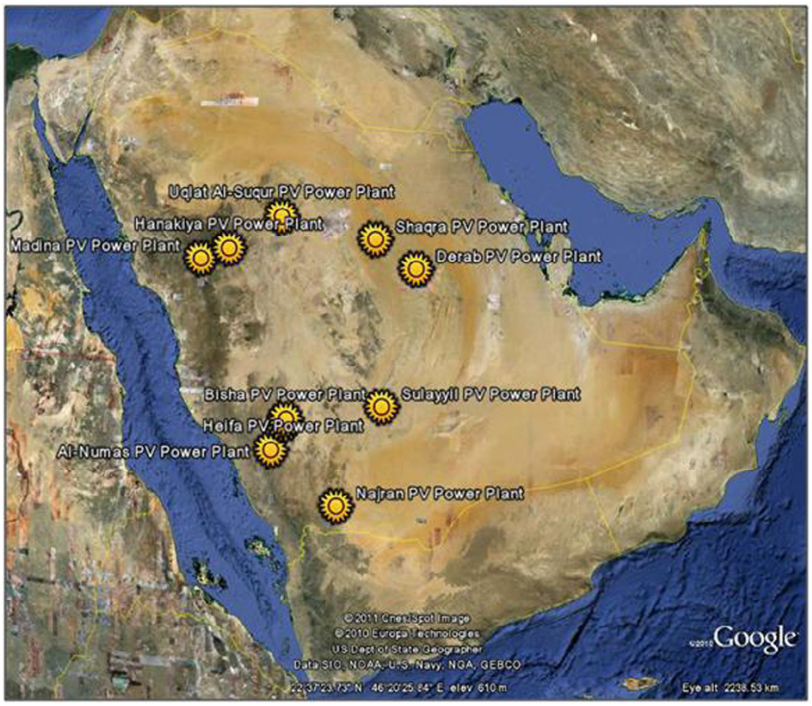


Figure 4.1: Best ten cites for solar irradiance in Saudi Arabia [55].

the east and the west coasts as well as the central parts of the country receive higher solar irradiance in the summer months [62].

In July 2014, the renewable resources atlas found that the direct norm irradiance (DNI) had the highest average of 9 kWh/m^2 in Tabuk city [59]. The DNI values range from 7.0 to 4.0 kWh/m^2 in January and from 9.5 to 4.0 kWh/m^2 in July in the west and east costs, respectively [67].

4.4.1 Solar Irradiance in Saudi Arabia from December 2015 to November 2017

It is believed that the solar irradiance information in Saudi Arabia was limited in the past. However, the available data from a historic measurement network clearly indicate that generating electricity from solar energy is a promising solution in the country. To

confirm that and gather more accurate data about the solar irradiance and the environmental conditions, K.A.CARE has established a unique solar measurement network known as the Renewable Resource Atlas through the Renewable Resource Monitoring and Mapping program (RRMM). It is deployed in most areas of the country in January 2013. Until November 2017, the network has 46 meteorological stations distributed throughout the country.

The 46 stations record the required solar and wind quantities: Global Horizontal Irradiance (GHI), Diffuse Horizontal Irradiance (DHI), Direct Normal Irradiance (DNI), wind directions and wind speed at different elevation levels, and the associated atmospheric data. These measurements are then sent to the central data management system, and they become available to the public and can be reached through an interactive online portal, Saudi Arabia Renewable Resource Atlas [68].

As shown in Figure 4.2, the Renewable Resource Atlas utilizes three types of the instrument configurations (Tiers): Tier 1- Research station installed at 28 stations, Tier 2- Mid-Range station installed at 18 stations, and Tier 3- Simple station. Tier 1 has three configurations; A, B, and C based on the available instrument. Further details about the differences between these types and the selection criteria of each type are summarized in [69]. The elevation of each station and the associated instrument configuration are presented in Table A.1 in Appendix A.

The data used here, which are DNI, DHI, GHI and the ambient temperature, are collected from 40 locations with serially completed data for a period of 24 months from December 2015 to November 2017. The remaining six stations have more than eight missing data, so they have been neglected.



Figure 4.2: Map of the solar monitoring network in Saudi Arabia [68].

The average monthly total radiation (for DNI, DHI, and GHI) and the average temperature are calculated to analyze the overall solar irradiance information at every station location and within every operating zone. They are summarized in Table A.2 in Appendix A. The selected 40 stations are carefully divided into groups based on their geographical locations to identify the radiation patterns among the operating regions specified by the SEC. The number of measurement stations at every area varies as the central region has 12 stations while the eastern region has only five measurement stations.

The plot in Figure 4.3 shows the average monthly irradiance for some of the locations. For the selected 40 stations, the average monthly GHI ranges from about 5.537 kWh/m^2 at Dhahran in the eastern area to 6.696 kWh/m^2 at Najran in the southern area of Saudi Arabia. It is also noticed that the DHI and DNI show variations of 1,179 Wh/m^2 and 3,201 Wh/m^2, respectively.

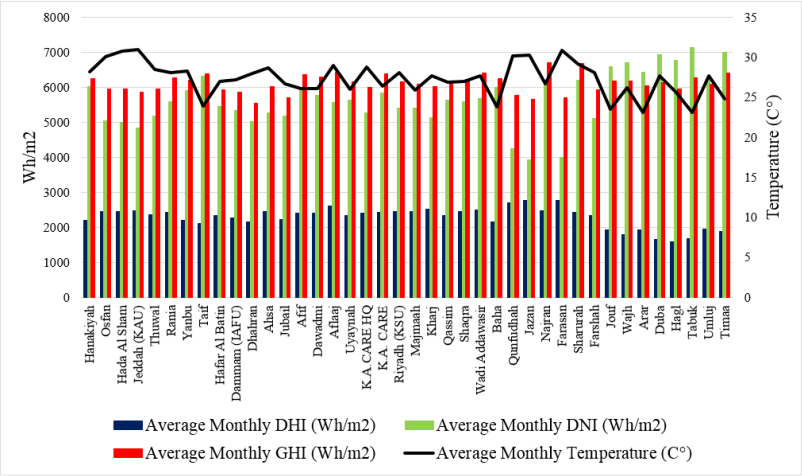


Figure 4.3: Summary of the average solar irradiance and temperature in all sites.

It can be seen that the stations in the southern operating region of Saudi Arabia have the highest average monthly GHI at Najran and Sharurah. In terms of average monthly DNI, all stations in the northern region have recorded the highest DNI across the country. This fact can be linked to the highest number of cloudless days that have been experienced in the northern area. On the other hand, the stations in northern Saudi Arabia have the lowest values of DHI, which is the totally opposite of the pattern of the DNI due to the lower scattering of the radiation [69]. In fact, the highest average value of DHI (2,775.55 Wh/m^2) is observed at Jazan (in the southern region), which has the lowest monthly average value of DNI (3,934.4 Wh/m^2). For each station, the maximum ambient temperature recorded in the summer months, July and August, as the highest temperature in this 24-months period was recorded at Hafar Albatin in the eastern province. It was 39.9 ^{0}C in August 2017.

Comparing the solar irradiance among the operating regions, Figure 4.4 presents the overall magnitude of the solar resources at each region. It can be seen that the central region has the highest average monthly GHI (6,216.3 Wh/m^2) whereas the eastern region has the

lowest GHI. This can confirm the results found by [69] for the period from October 2013 to September 2014. For the selected period in this study, the variations of the average monthly DHI, DNI and GHI are 0.714 kWh/m^2, 1.63 kWh/m^2, and 0.41 kWh/m^2, respectively. This variation can be linked to several factors such as amount of sunshine, humidity, and aerosols. However, the relatively small variability indicates that the solar irradiance is consistent throughout Saudi Arabia.

Regarding the continuity of the solar radiation, all stations in the southern region, for example, never record a GHI value below 4,000 Wh/m^2 as shown in Figure 4.5. The maximum values of GHI in all stations occurred in the months of May and June of the two years while the peak average monthly DNI recorded in July 2017 in the northern part, and in October 2017 in the central and the southern areas.

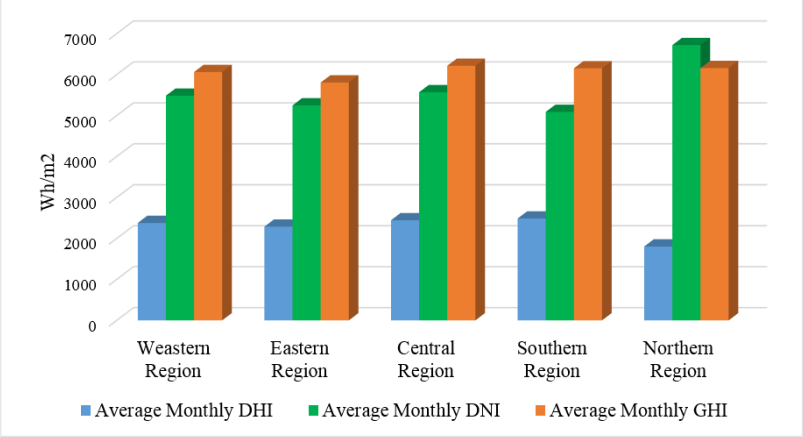


Figure 4.4: Average monthly solar irradiance for all regions.

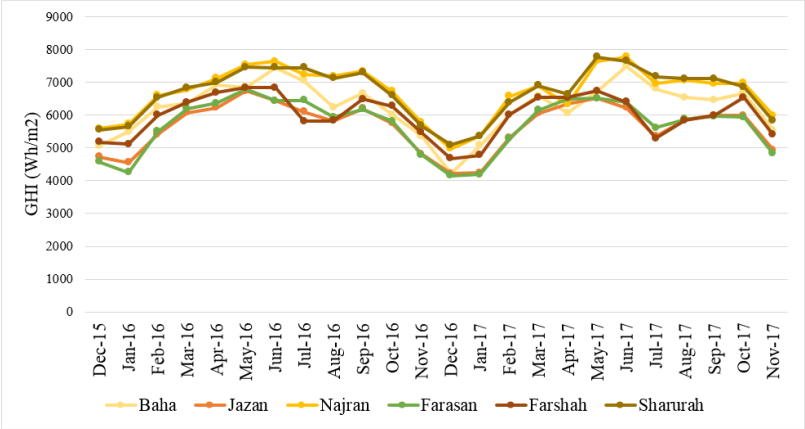


Figure 4.5: Average global horizontal irradiance in the southern region.

The diffuse fraction is defined as an indication of the amount of clouds during a specific period of time [70]. It can be described by the ratio of direct horizontal irradiance to global horizontal irradiance. Figure 4.6 shows the monthly average diffuse fraction for all five regions. The five regions are ranked based on the clearest sky as follows, northern, eastern, central, western and southern areas with a difference of 0.012 among the last four areas. In terms of individual stations, the diffuse fraction varies from about 0.27 at Tabuk in the northern area to 0.49 at Jazan in the southern portion of Saudi Arabia. In fact, about half of the stations across the country have the diffuse factor between 0.35 and 0.40 as can be seen in Table A.3 in Appendix A.

In Summary, the global horizontal irradiance is high in all areas across the country. This indicates that most of the locations in Saudi Arabia are convenient to install photovoltaic to harvest the energy from the sun. However, the relatively high ambient temperature, which reaches more than 40 ^{0}C in some cities in Saudi Arabia during the summer season, could deteriorate the efficiency of the PVs. Both three measures used here; DHI, DNI, and GHI clearly reinforce the fact that the solar energy potential is strong in Saudi Arabia and is

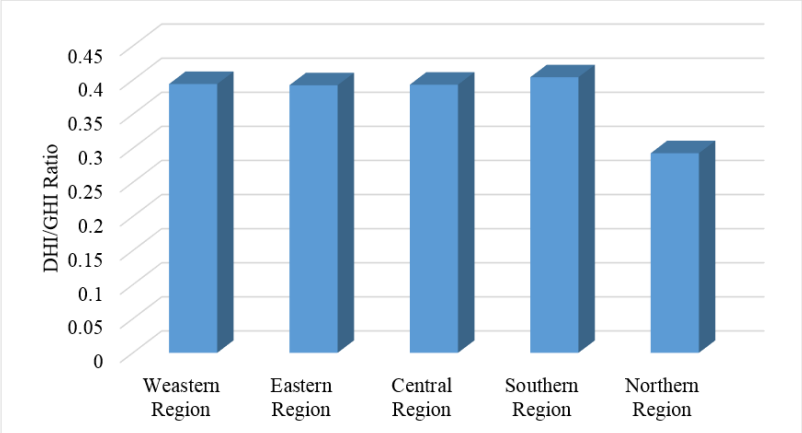


Figure 4.6: Averages monthly DHI/GHI ratio for each region.

sufficient to generate clean electricity as their minimum values are far above the minimum accepted threshold for PV and CSP.

4.5 Summary

This chapter provides a general overview about the solar energy resources in Saudi Arabia. It summarizes the advantages, obstacles, and the history of solar energy in the country. The solar irradiance in Saudi Arabia are studied using the available data of the last two years. It is found that there is adequate solar radiation all over the country throughout the year. This confirms the fact that locating Solar panels in any area is a rational decision based on the locations of the load centers.

Chapter 5

IMPACT OF THE SOLAR PENETRATION ON THE FREQUENCY STABILITY OF THE SAUDI POWER GRID

5.1 Introduction

To the extent of the author's knowledge, most of the studies related to solar energy in Saudi Arabia investigated the availability of solar irradiance and the best locations for installing PV plants based on the available irradiation information. However, many of the stability and operation issues regarding solar PV grid integration have not yet been investigated and fully explored. The expanding of using Solar PV raises the concerns about the power system

stability. Thus, the effect of PV penetration on the Saudi network stability and reliability deserves a comprehensive investigation. It is important to study the behavior of the grid during PV integration to ensure that the grid reliability and security must not be jeopardized. This chapter focuses on the impact of high PV solar penetration on the frequency stability of the Saudi grid. Before this, this chapter describes, with considerable details, the procedure of developing high solar penetration model of the Saudi grid.

5.2 Solar PV Penetration in the Saudi Grid

5.2.1 Solar PV Model

The general structure of a solar PV plant that is linked to a grid is shown in Figure 5.1. It comprises a PV module, a DC/DC power electronic converter, a DC/AC power electronic inverter, a power transformer to be connected to the grid, and a control system. In some cases, a storage system is integrated into a grid connected PV plant.

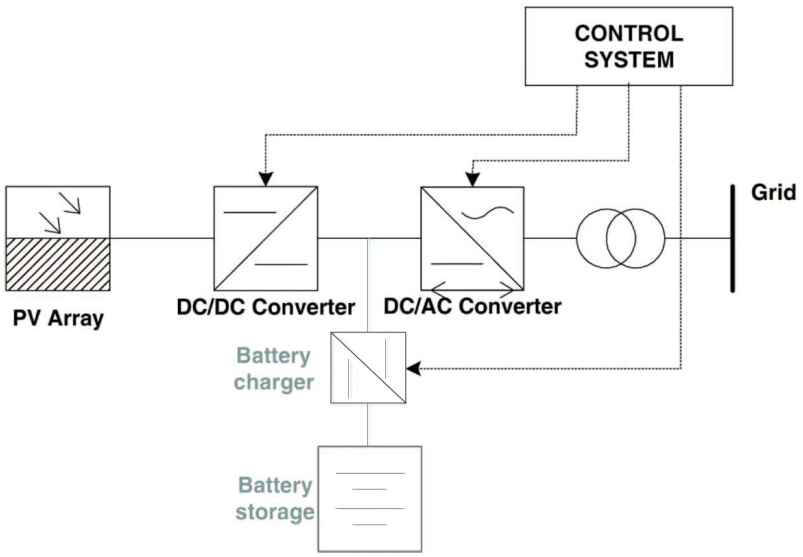


Figure 5.1: General structure of a grid connected solar PV plant [71].

For the load flow model, the solar plant is represented by a conventional generator and a transformer connected to the grid as can be seen in Figure 5.2. It is important to ensure that the MVA rating of the generator must match the PV device ratings [72, 73].

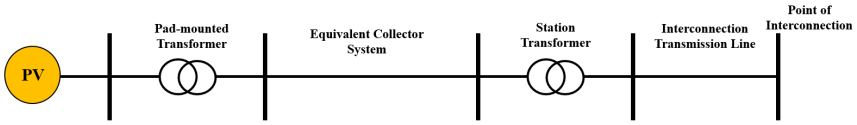


Figure 5.2: Load flow representation of large scale PV unit.

To represent the dynamic performance of the solar PV plant, the GE solar photovoltaic plant model is used. This model is designed to be used with PSS®E. It is accurate enough to capture the dynamics of the PV. The GE PV model is superior to the built-in PSS®E PV model due to the unlimited number of the PV units to be used [17].

The GE PV model is prepared to show the dynamic behavior of a solar plant when any disturbance occurs in the grid; however, it is not built for short circuit or electromagnetic studies [72]. It is difficult to analyze the disturbances that occur through the solar plant local grid. In fact, the rapid dynamics of the control response are modeled using algebraic equations [72]. In real system, the inverters of several solar PV units are aggregated and injected into a power grid at a single point. In the simulation, the identical inverters are represented by one equivalent large inverter. In addition, the presented GE model assumes that the supplied power from all inverters are the same, which means the solar irradiance is uniform throughout the PV plants [72].

Regarding the GE PV dynamic model, it has two main components: inverter and electrical control as shown in Figure 5.3. Based on the control commands being provided from

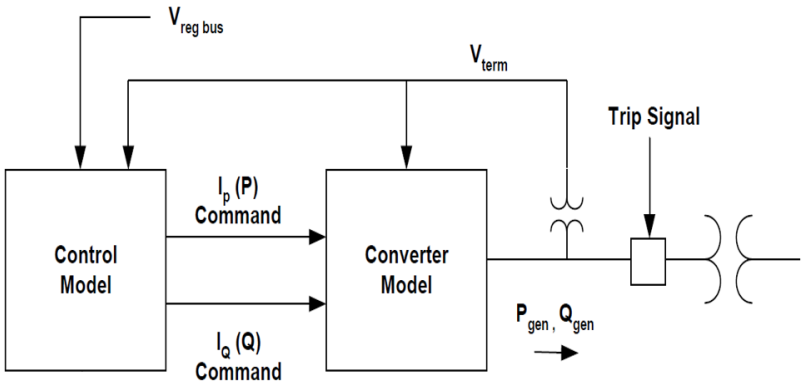


Figure 5.3: GE solar PV model dynamic model overview [72].

the electrical control (GEPVE), the inverter (GEPVG) supplies real and reactive currents into the grid. Also, the inverter model, which fully mimics the dynamic response of a large scale PV unit, has under/over voltage and under/over frequency protective functions. It represents the interface between the power network and the solar plant [72, 73].

The control model initiates the active and reactive current commands based on the actual terminal voltage. It also controls the amount of active and reactive power transmitted to the grid according to the power flow initial conditions and the reactive power control methods, including voltage regulation (VRS), fixed power factor, and fixed reactive power. It has mainly four control strategies as summarized in Table B.1 in Appendix B. The control has converter current limiter that limits the total real and reactive currents from going beyond the converter capacity based on a user-specified flag (PQFLG), which can be either real power priority or reactive power priority mode [17, 72]. The parameters of both GEPVE and GEPVG for one of the PV units used in this study are summarized in Table B.2 and Table B.3 in Appendix B, respectively.

5.2.2 Solar PV Plants Locations and Penetration Levels

The locations of the PV plants should be selected effectively such that each chosen location must receive adequate amount of the average solar radiation throughout the year and should be close to the load centers. It has been stated earlier in section 4.4.1 that most areas in Saudi Arabia are exposed to higher levels of solar irradiance. This means that all of the five operating regions are suitable to install solar PV plants.

Since conventional generators in the Saudi model will be gradually replaced by PV plants as the solar penetration level increases, a proposed selection criteria in [17] is applied in this study. Due to the fact that the solar plants are operated at higher power factor values, the conventional machines with higher power factor are chosen to be displaced first.

According to the Saudi Arabian Grid Code [44, 74], the System frequency must be maintained in the range of 59.9 and 60.1 Hz during the normal operation. As long as the frequency deviations are kept within these limits and the system is still stable after applying any type of disturbance, more PV plants can be added to the developed Saudi model.

PV plants are gradually added to the system with the following penetration levels: 10%, 30%, 50%, and 65%. Any addition of PV plants more than 65% to the current grid results in losing stability of the system. The locations of the PV plants are shown in Figure 5.4 through Figure 5.7. The amount of solar generation for each penetration scenario is summarized in Table 5.1. Tables C.1-C.4 in Appendix C list the generators that have been displaced to accommodate for PV units within the studied area for all four penetration levels.

Table 5.1: The generation amount for each of the solar PV penetration levels.

Solar PV penetration level	PV generation (MW)
10% PV penetration	3,081.40
30% PV penetration	18,270.58
50% PV penetration	30,463.25
65% PV penetration	39,654.68

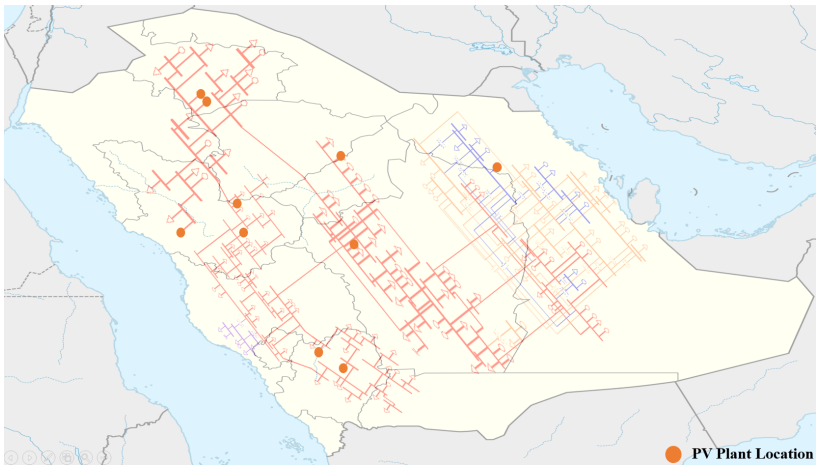


Figure 5.4: 10% PV penetration map.

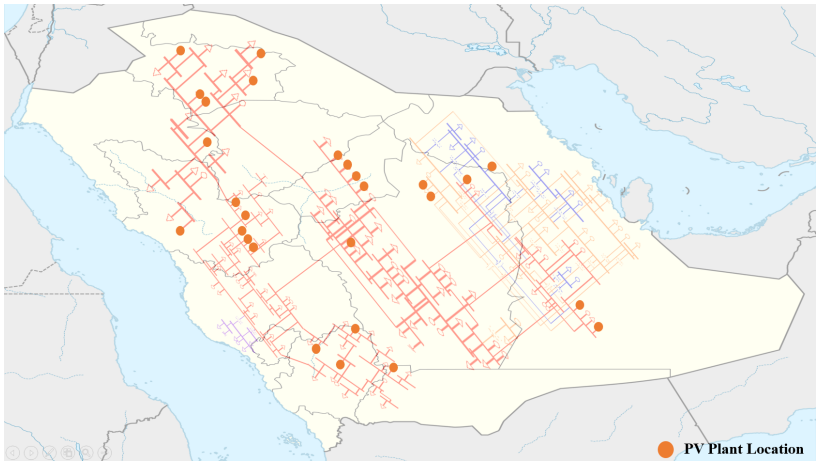


Figure 5.5: 30% PV penetration map.

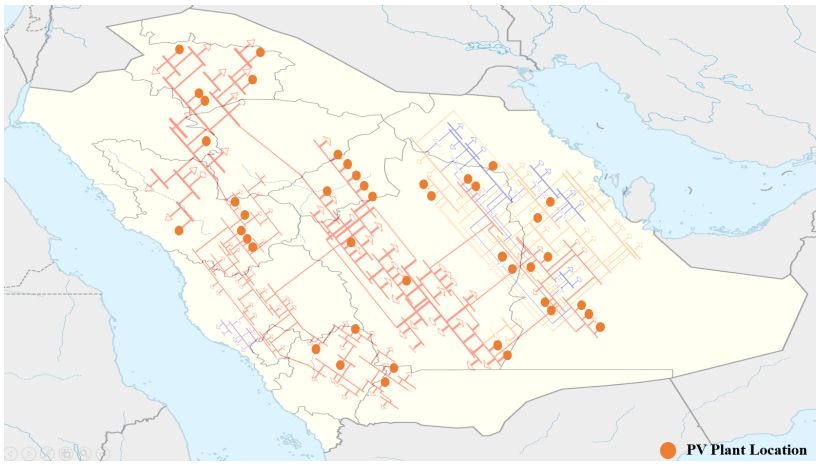


Figure 5.6: 50% PV penetration map.

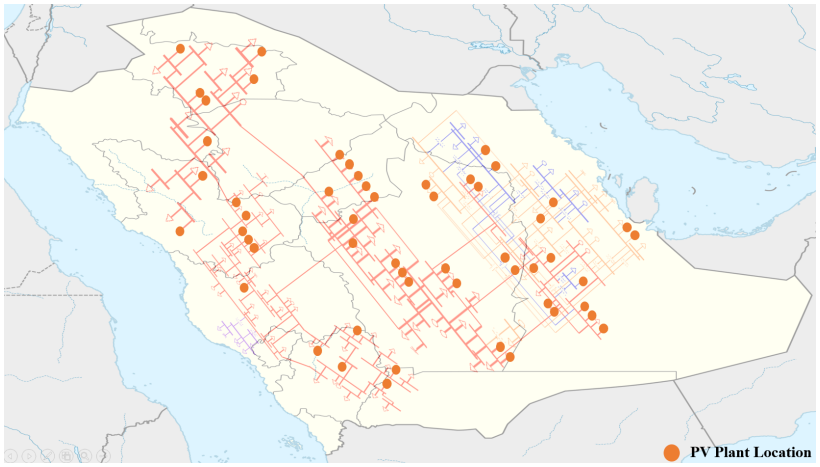


Figure 5.7: 65% PV penetration map.

5.2.3 Flat Run Simulation with High PV Penetration

After integrating the PV dynamic model into the developed Saudi grid, it is important to ensure dynamic and numerical stability of the model and the readiness of the model for dynamic studies. In order to do so, a no-disturbance simulation that lasts for 40 seconds is applied. The simulation results of frequency response for all proposed PV penetration cases are shown in Figure 5.8. It can be observed that the system dynamic simulations for all PV

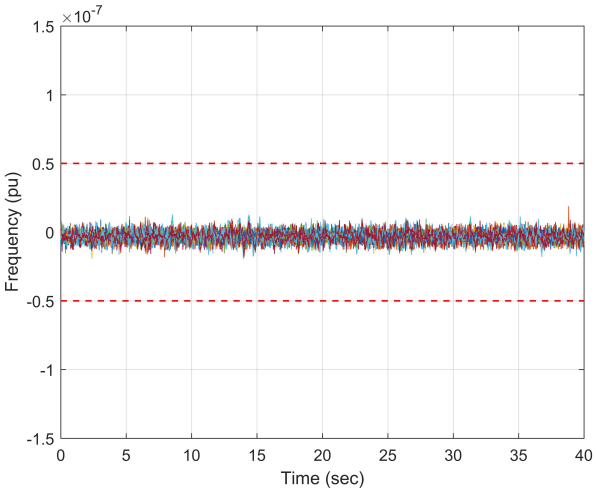
penetration levels are converged with very small numerical oscillations that fall in the range between 5×10^{-8} and -5×10^{-8}.

5.3 Impact of High PV Penetration in the Saudi Grid on Frequency Response

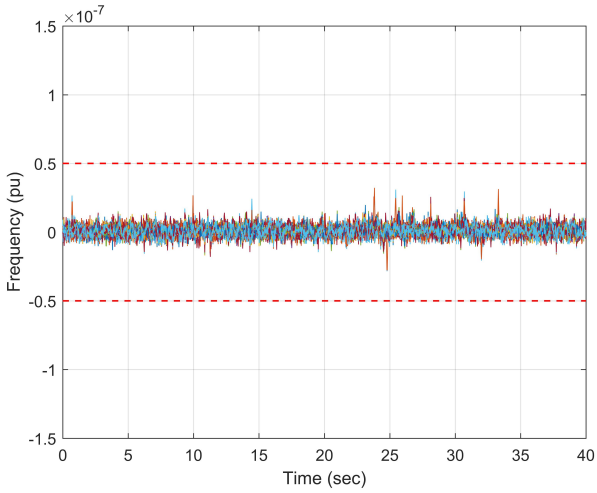
Frequency response can be defined as the behavior of the system frequency after being subjected to an event that disturbs the balance between power generation and demands. Generally, synchronous machines have inertia that provides frequency support for a few seconds after generator trip events. It has been determined that the settling frequency is associated with the governor ratio in the system as the higher governor ratio reduces the frequency deviation [17]. Frequency deviation needs to be mitigated to avoid system security and stability issues.

It is known that displacing conventional coal-fired machines with renewable units can result in reducing the overall system inertia as they have low or zero inertia. Further, most solar units cannot provide extra active power for frequency support as they run at their maximum power tracking condition. Thus, when an event happens in a grid having much renewable generation, the system frequency may deviate too much and result in losing the stability of the system.

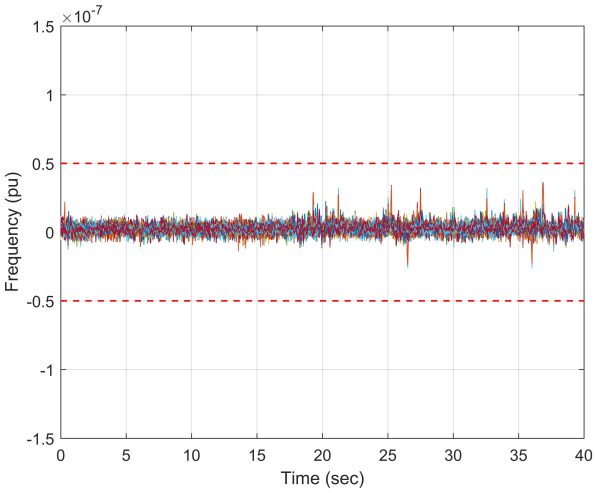
In this section, a dynamic simulation is performed to observe how the system frequency behaves after different types of disturbances as more PV units are added to the grid.



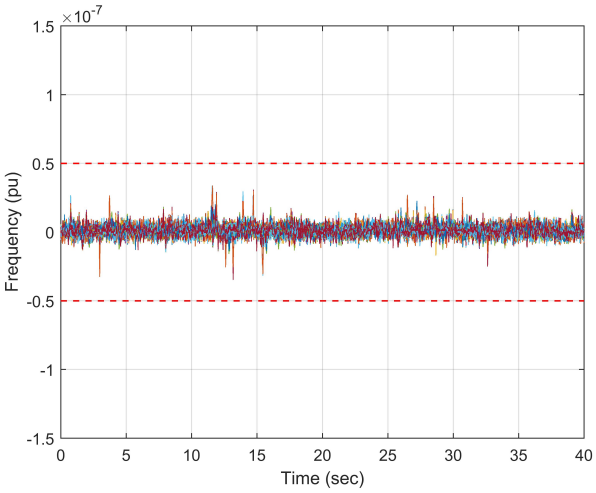
(a) 10% PV



(b) 30% PV



(c) 50% PV



(d) 65% PV

Figure 5.8: Frequency deviations without disturbance.

5.3.1 Impact of Losing a Conventional Generator

It is well-known that losing a conventional machine affects the system stability based on the machine's generated power amount as well as its location in the grid. However, high level of PV penetration in the grid could exaggerate the impact of losing synchronous generators that occurs due to several reasons such as operational errors or maintenance.

This study investigates the influence of sudden loss of a large conventional machine with the integration of solar PV plants by simulating two different cases in the western and the central operating areas in the Saudi grid. These two generators are selected here because they supply the highest power among the remaining conventional facilities in the studied system.

Case 1:

The largest gas turbine unit located in the western operating area (WOA) that generates 1,683 MW at bus 102 is tripped offline. The same bus has another PV power plant that is proposed to deliver a similar amount of active solar power in Jeddah City. Therefore, this case could be an excellent example to show the effect of the high level of solar penetration on the system response due to a loss of a conventional machine. Figure 5.9 presents the single line diagram of the WOA showing the location of the tripped generator and the PV plants.

This machine (J2) is taken out at a simulation time t=5 sec and the frequency response, shown in Figure 5.10, is recorded at bus 108 for the four PV penetration levels with the case of no PVs integrated into the grid.

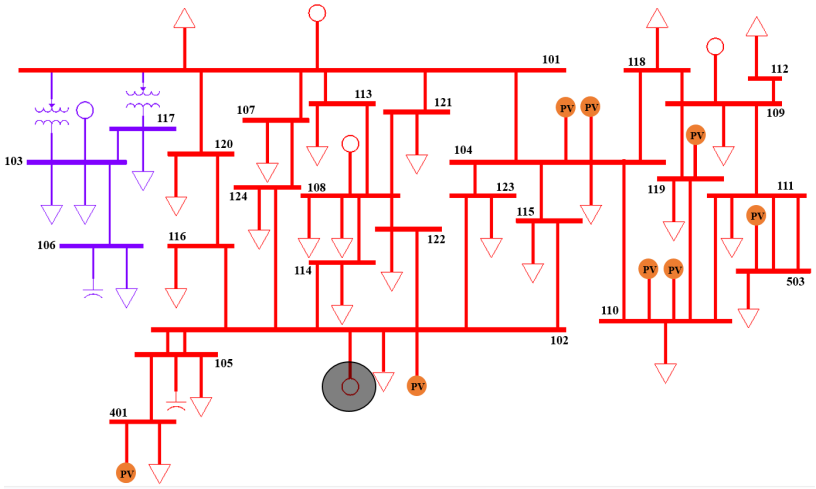


Figure 5.9: Single line diagram of the western operating system.

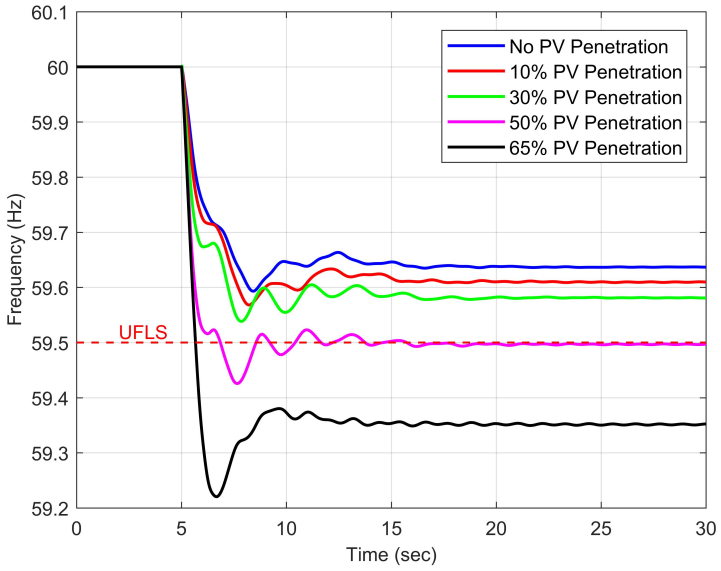


Figure 5.10: Frequency response after tripping a conventional generator in the WOA.

Simulation results show that losing this machine caused frequency drop and noticeable oscillations in the frequency response. As the amount of the PV generation increased, the frequency drop tended to be faster. It can be seen that the under-frequency load shedding (UFLS) might be triggered for both 50% and 65% PV penetration levels. The settling frequency showed considerable differences among all PV penetration levels. It can be seen that the settling frequency decreased from 59.64 Hz to 59.61 Hz and 59.35 Hz for the cases of 10% and 65% PV, respectively.

Case 2:

The gas turbine unit (Y1) at bus 302 in the central operating area (COA) is chosen for this study. The reason for selecting this machine is that it generates about 860 MW, which is found to be the largest conventional machine after displacing most of the machines in the COA with PV plants. As can be seen in the single line diagram of the COA in Figure 5.11, the bus 302 is surrounded by more PV plants for the 65% PV case. In fact, more than 83% of the generation in COA comes from solar PV units at this penetration level.

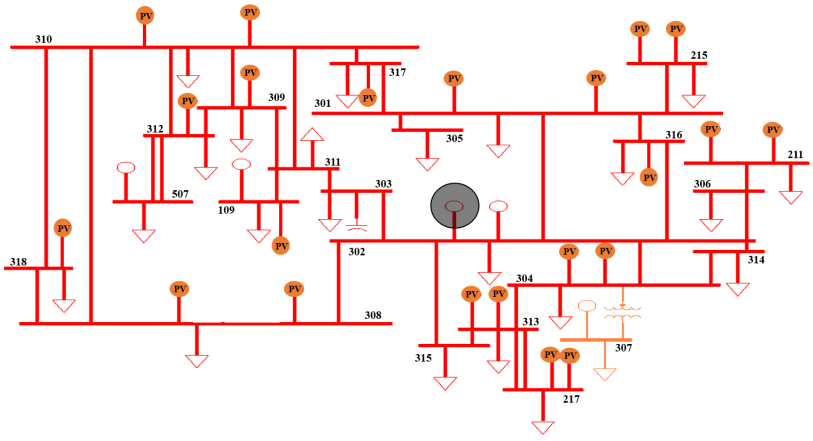


Figure 5.11: Single line diagram of the central operating system.

The similar procedure that is used in case 1 is applied here. The generator is switched off the service at five seconds into the run and the frequency behavior at the adjacent bus 307 is captured and shown in Figure 5.12 for all PV penetration levels.

The frequency response showed small oscillations that are damped within a short period of time. Although the frequency nadir never went below 0.3305 Hz from the nominal system frequency, this drop increased as the PV penetration level increased due to the decrease in the overall system average inertia. The frequency of the 65% PV settled at much lower value with about 0.15 Hz deviation from the settling frequency of the case without PV.

From the previous two cases, it can be concluded that losing a single conventional generator during normal operating conditions with high levels of solar penetration results in significant deviations and causes severe frequency stability impact in the system. Therefore, these noticed impacts must be taken into consideration during system planning for solar energy interconnection.

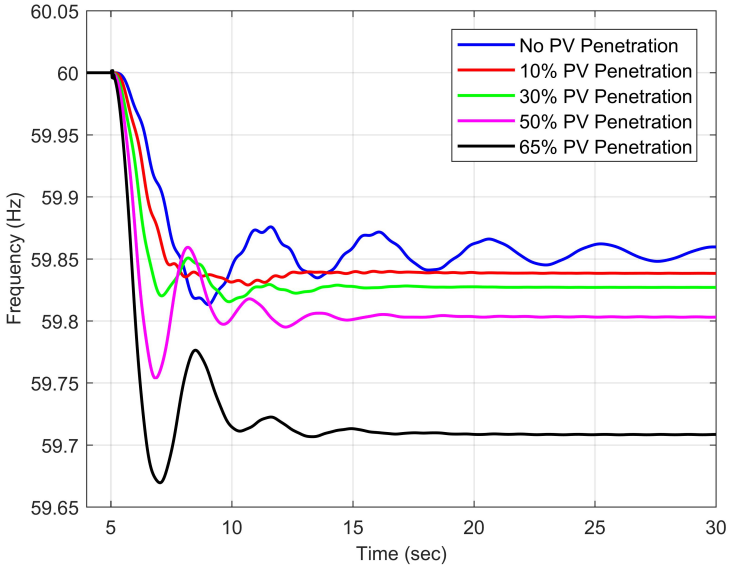


Figure 5.12: Frequency response after tripping a conventional generator in the COA.

5.3.2 Impact of Tripping a Large PV Plant

The amount of power that comes from photovoltaic system heavily depends on weather conditions; thus, cloudy or rainy weather may result in fluctuating the delivered power from the PVs or even leading to loss a considerable number of PV plants. Moreover, PV plants could trip due to different types of disturbances or protection errors. Therefore, the worst case scenario of losing a PV plant is simulated in this section to study the dynamic behavior of the grid under 10%, 30%, 50% and 65% PV penetration levels.

The PV plant at bus 310 in the central region is tripped out at t=5 sec. The PV plant generated about 860 MW at the time of disconnection. Figure 5.13 shows the frequency response at bus 218 when the solar plant is dropped with several PV penetration levels.

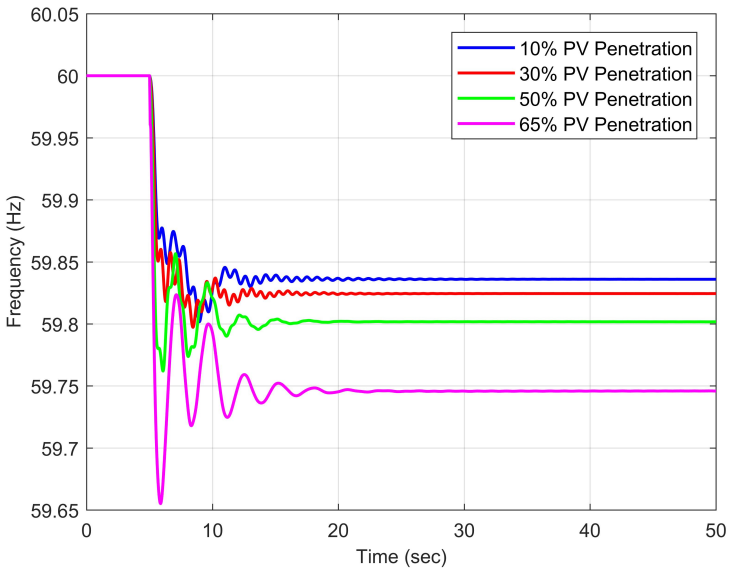


Figure 5.13: Frequency response after tripping a large PV plant.

It can be seen that the increasing number of the solar panels exhibited a clear effect on the frequency response. Tripping this PV plant generated momentary oscillations in the system frequency and its value was affected by the penetration level as more PV penetration

resulted in higher oscillation magnitudes. The magnitude of the frequency decreased to almost 59.65 Hz for 65% of PV penetration level, which denotes the risk of PV penetration on the frequency stability of the grid.

5.3.3 Impact on Frequency Response Characteristic

In order to observe the effect of the high PV penetration on the frequency response characteristic (β), 20 conventional machines are tripped throughout the five operating areas with different PV penetration levels. Then, the average *Beta* value for all cases for each penetration level is calculated. It has been noticed that the Saudi grid *Beta* value declined from 5.195 MW/mHz for the no-PV case to about 2.5 MW/mHz as the PV penetration level reached 65% as can be seen in Figure 5.14. This can be explained by the fact that the average system inertia is reduced as the system includes more renewable resources.

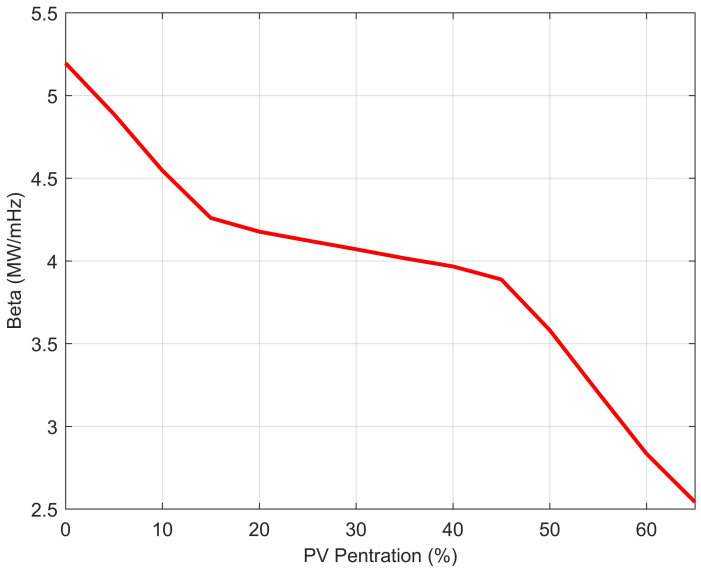


Figure 5.14: Saudi grid *Beta* value with different PV penetration levels.

5.3.4 Impact on Frequency Metrics

This section aims to study the power system frequency metrics changes due to a synchronous generator outage with the increased penetration of solar energy.

The frequency metrics are used as indicators to measure the primary frequency response after a disturbance. The following metrics are used here to assess the impact of the high PV penetration on the system frequency response of the Saudi grid:

- **The rate of change of frequency (ROCOF):** It is the frequency decline rate of the first 0.5 second after a contingency, and it is measured by Hz/second. It can be determined by the stored kinetic energy in the grid. Higher values of ROCOF could lead synchronous machines to be disconnected due to triggering ROCOF relays. 0.5 Hz/s is the ROCOF threshold standard in the grid code in Ireland [75]. In Great Britain, the ROCOF standard should not be more than 0.25 Hz/s [76]. The ROCOF values should be between -4 Hz/s to 4 Hz/s in Australia [77].

- **The frequency nadir:** It is the lower frequency level that a frequency response can reach in a frequency decrease after an event [78].

- **The frequency nadir time:** It is the time taken for the frequency response to get to the frequency nadir [77].

- **The settling frequency:** It is the steady state frequency value when the frequency settles down and stabilizes after a disturbance. Some security standards defined the settling frequency as the frequency value at 60 seconds after the event [76, 77].

- **The settling frequency time:** It is the time when the frequency settles down after a disturbance.

In order to estimate the impact of the PV penetration on the above metrics, a machine (or a group of machines) that generates about 870 MW in each operating area is tripped at t= 5 sec under different PV penetration levels and the frequency metrics are calculated.

Only two cases are presented here to show the frequency response when the contingencies are applied in the WOA and the SOA as shown in Figure 5.15 and Figure 5.16, respectively. The frequency responses when the conventional machines are tripped in the remaining three areas (EOA, COA, and NOA) are presented Figure D.1 through Figure D.3 in Appendix D. The five frequency response metrics are shown in Figure 5.17 through Figure 5.21 for the five events in each operating area under different PV penetration scenarios.

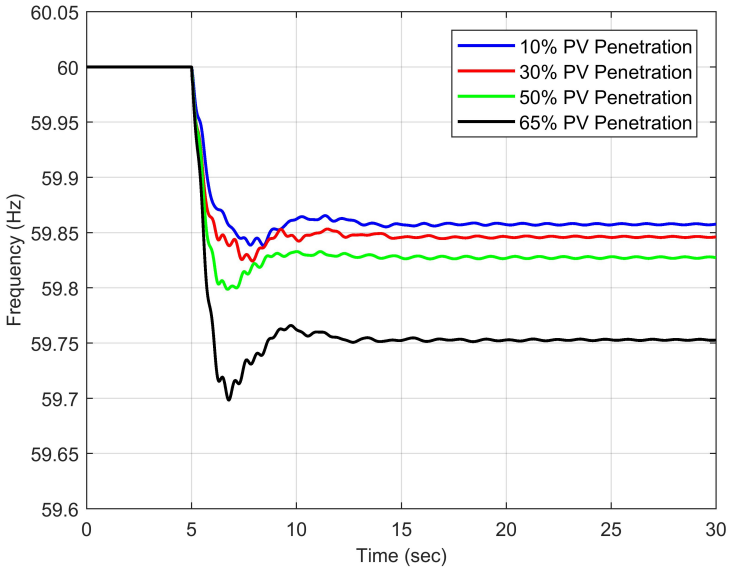


Figure 5.15: Frequency responses with different PV levels after a contingency in the WOA.

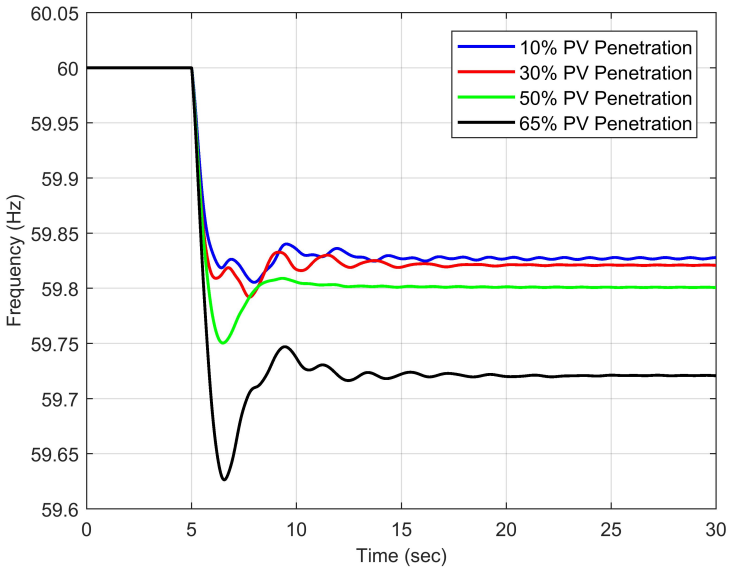


Figure 5.16: Frequency responses with different PV levels after a contingency in the SOA.

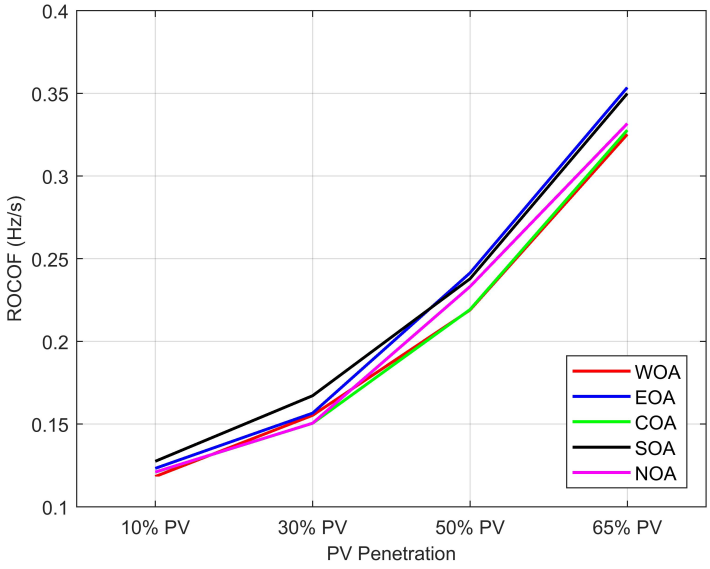


Figure 5.17: ROCOF change due to increased PV penetration level.

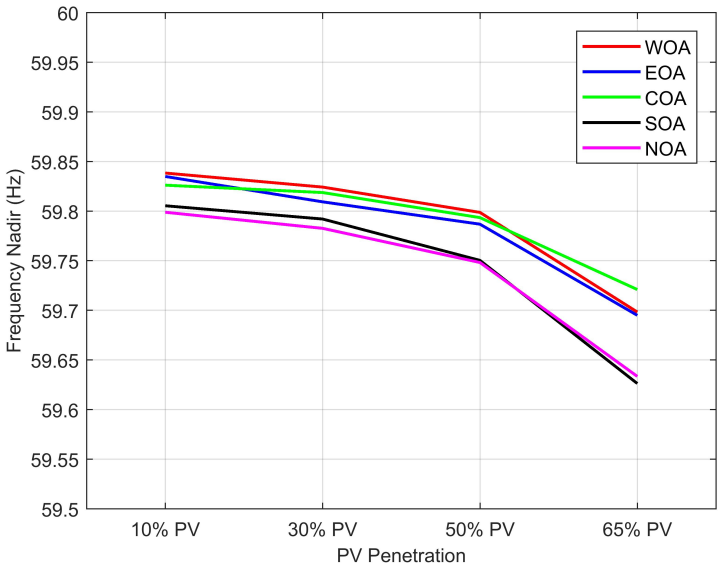


Figure 5.18: Frequency nadir change due to increased PV penetration level.

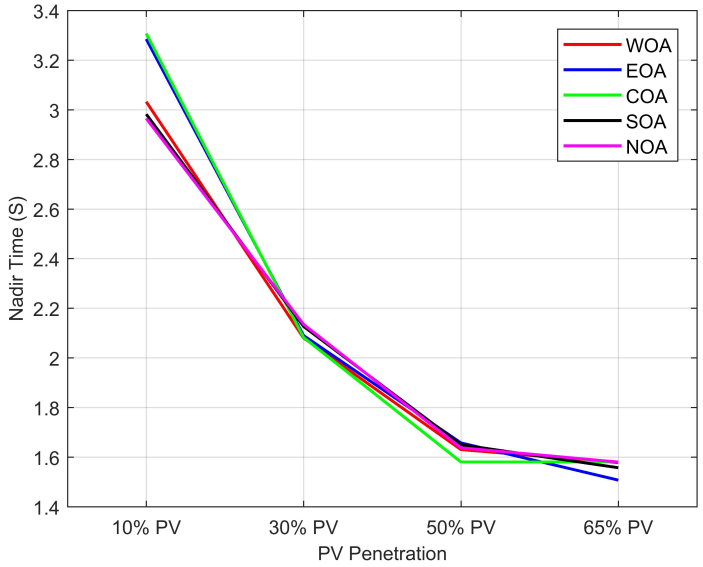


Figure 5.19: Nadir time change due to increased PV penetration level.

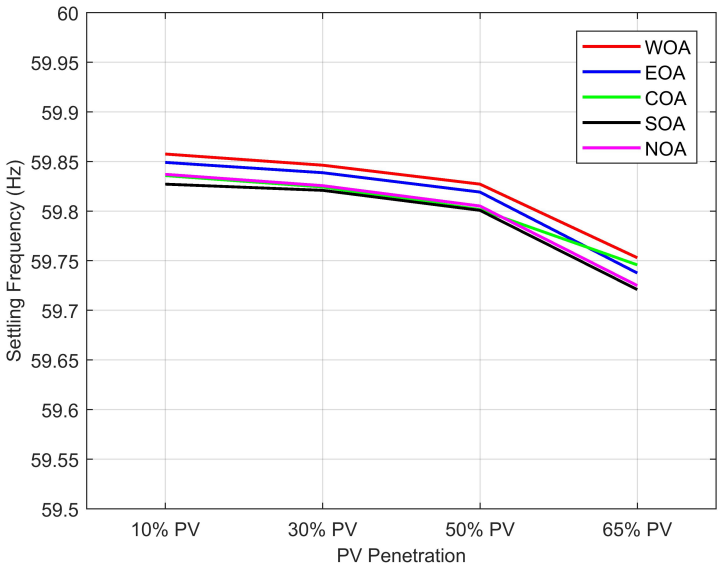


Figure 5.20: Settling frequency change due to increased PV penetration level.

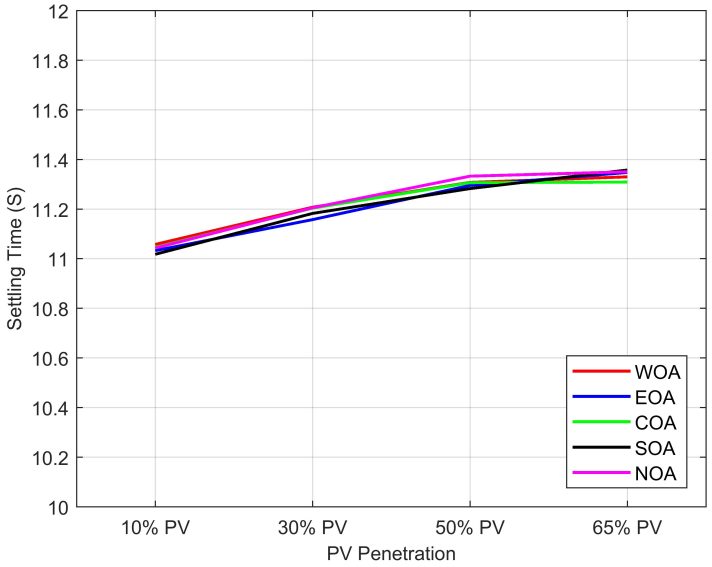


Figure 5.21: Settling time change due to increased PV penetration level.

It can be seen that the ROCOF increased significantly with the increasing PV penetration even though its values did not exceed 0.36 Hz/s. Figure 5.18 shows that the frequency nadir decreased slightly by 0.205 Hz between the 10% and the 65% PV levels. However, the frequency nadir time, as demonstrated in Figure 5.19, experienced a sharp decrease as more PV plants are being added. 1.77 second is the nadir time difference between the 10% and 65% PV penetration cases.

It can be seen that the settling frequency showed a decline trend due to 870 MW generation loss as the PV penetration level increased. The settling frequency was 59.86 Hz of the 10% PV level while it dropped to 59.72 Hz for the 65% PV level. On the other hand, no considerable change can be observed in the settling time as the frequency response always settled around 11.0 seconds when the disturbance was applied at 5.0 seconds.

In terms of the prediction uncertainty for all frequency response metrics for the five similar events, it has been found that all frequency response measures are within ±5% of their average values as shown in Figure 5.22.

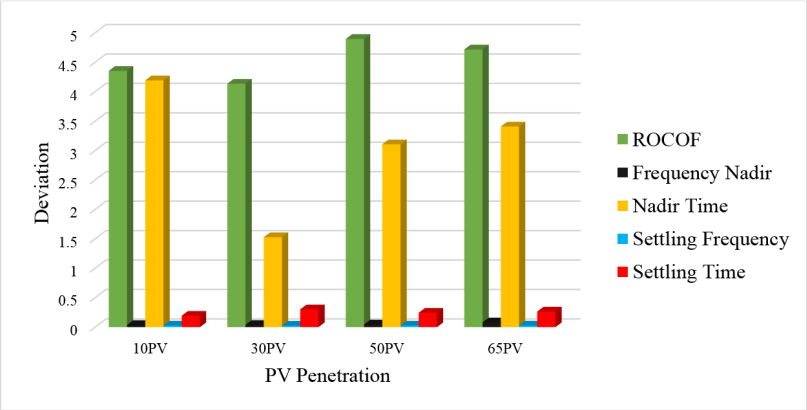


Figure 5.22: Maximum deviation for all frequency metrics from the mean value with different PV penetration levels.

It can be concluded that the ROCOF noticeably increases while the frequency nadir and the settling frequency decrease consistently with the increase of solar generation. This is due to the fact that the higher solar PV units replace the conventional machines, which results in lower system inertia. In addition, it has been discovered that the event location does not change frequency response metrics significantly due to the smaller size of the grid.

5.3.5 Impact on Under-Frequency Load Shedding

Under-frequency load shedding is used to maintain the power system frequency within nominal limits when the frequency drops due to a generation loss. The main principle of UFLS is to disconnect an appropriate amount of loads to restore the frequency to the nominal value before a complete system collapse occurs. The UFLS threshold assumed in this study is 59.5 Hz.

This section investigates the impact of the high solar penetration on the UFLS in the Saudi grid. In each of the five operating areas in the Saudi grid, a typical contingency is applied and the frequency response is recorded. Table 5.2 summarizes the information about these contingencies. Each of the contingencies is simulated at time t=5 sec and the frequency response along with UFLS threshold are shown in Figure 5.23 through Figure 5.27 for all cases at the five operating regions.

In the WOA, results show that the UFLS might be triggered for the 50% and 65% PV penetration cases when losing 1,683 MW generation.

Table 5.2: Typical contingencies at each operating area.

Area	Tripped power amount (MW)
West operating area (WOA)	1,683.95
East operating area (EOA)	1,236.80
Central operating area (COA)	1,722.20
South operating area (SOA)	1,258.50
North operating area (NOA)	1,282.20

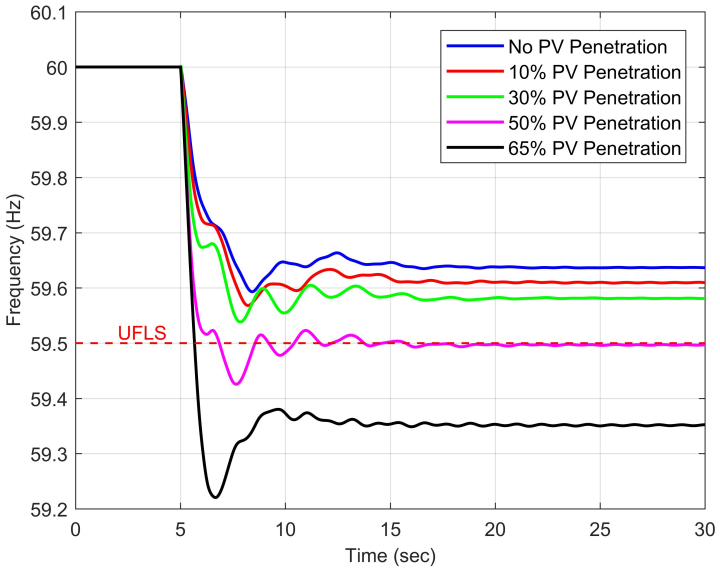


Figure 5.23: Frequency responses after 1,684 MW generator loss in the WOA.

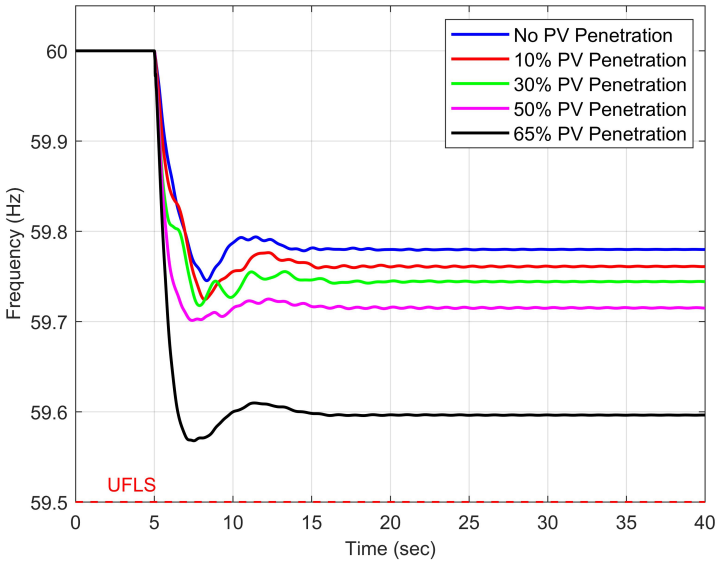


Figure 5.24: Frequency responses after 1,237 MW generator loss in the EOA.

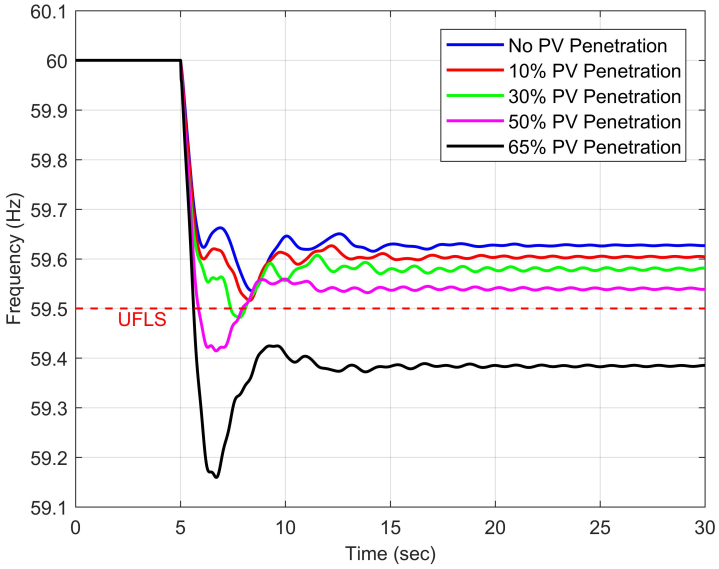


Figure 5.25: Frequency responses after 1,722 MW generator loss in the COA.

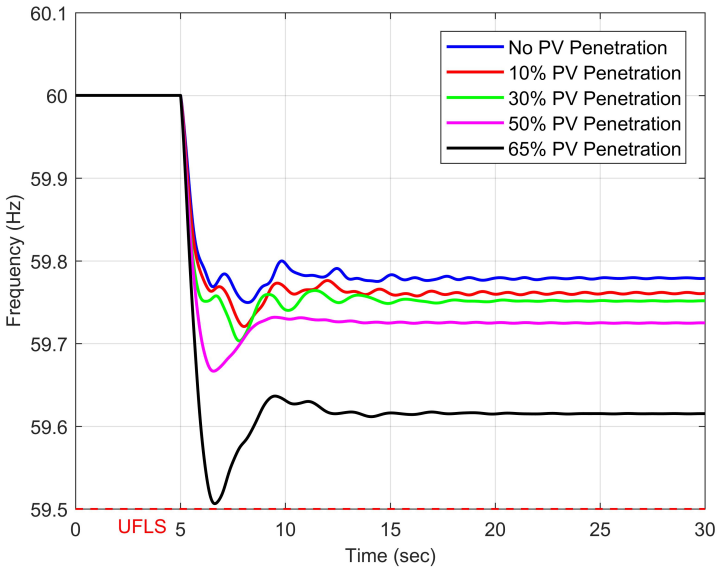


Figure 5.26: Frequency responses after 1,259 MW generator loss in the SOA.

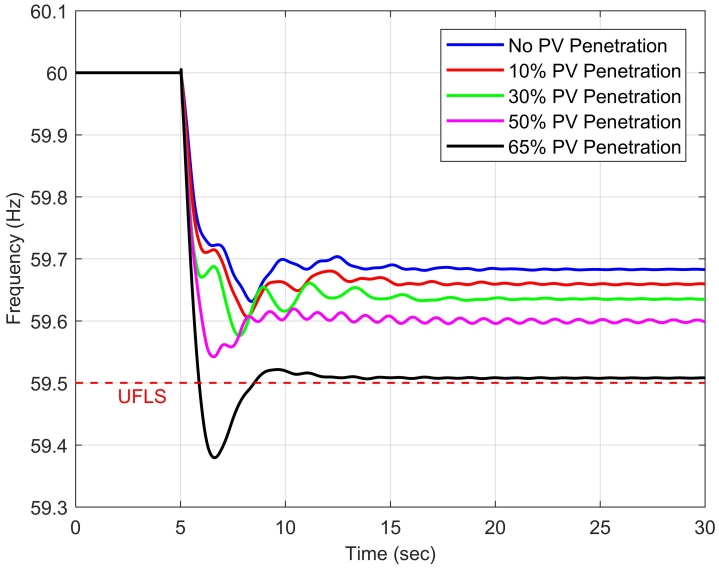


Figure 5.27: Frequency responses after 1,282 MW generator loss in the NOA.

On the other hand, the frequency nadirs for all PV penetration scenarios in the EOA were far above the UFLS threshold. This large margin can be attributed to the smaller contingency amount and the higher generation capacity in the region compared to the load demand. Therefore, the increased PV penetration may not pose a real risk on the UFLS for such an event in this area.

It can be observed in Figure 5.25 that the frequency nadir in the COA associated with the 10% PV penetration case was slightly higher than 59.5 Hz, while the nadirs of the other three penetration scenarios were lower than 59.5 Hz, which led to triggering the UFLS and shedding some amount of load. This is due to the fact that the central region has the highest load demand and the amount of the tripped power is the highest. In fact, this would create higher risk for losing larger generators in the COA with 30% or more PV integration.

Even though the frequency response decreased dramatically in the 65% PV penetration case (Figure 5.26), its frequency nadir did not reach the UFLS threshold. However, this disturbance in the SOA under such penetration makes the frequency nadir close to the UFLS threshold.

The frequency nadir as a result of a generator trip in the NOA was higher than 59.5 Hz for all PV penetration cases except for the 65% PV penetration case. In other words, the grid is vulnerable to UFLS actions in the NOA.

In Appendix D, the average frequency responses for each operating area are shown with different PV penetration scenarios after a contingency at the central region is applied.

It can be concluded that the scheme of the current UFLS implemented in the Saudi grid needs to be readjusted when considering high solar penetration.

5.3.6 Impact of 100% PV Penetration at One Area

Electrifying an entire area with renewable energy is the ultimate goal for utilities seeking clean electric power. In addition, some small areas in Saudi Arabia (e.g., Northern and Southern) receive higher solar irradiance, which makes it possible to power the whole operating area with solar power. However, there might be some obstacles associated with the grid depending totally on the solar energy that need to be addressed. An interesting study is to see how the system response looks like when applying a disturbance in a totally solar powered area. Additional study is conducted to find out how much solar generation can be tripped without effecting the overall stability of the grid.

The northern operating area (NOA) is chosen for this study. All conventional machines in the NOA are replaced with PV solar plants. Therefore, the total solar generation in this region becomes more than three gigawatts, which is about 5% of the total installed capacity of the Saudi grid.

A generator trip event is applied in the northern area and the average frequency response of both regional and national grid are recorded and depicted in Figure 5.28 and Figure 5.29 for the 10% and 65% PV penetration levels nationwide, respectively.

Even though the average frequency response for the NOA showed small oscillations, it followed the path of the average national grid frequency for all PV penetration levels. It can be observed that both responses had quite similar ROCOF, frequency nadir and settling frequency. These results demonstrate that electrifying small areas in the Saudi grid totally with solar power would not raise serious concerns with regard to frequency stability, considering the fact that they can receive enough power from adjacent areas.

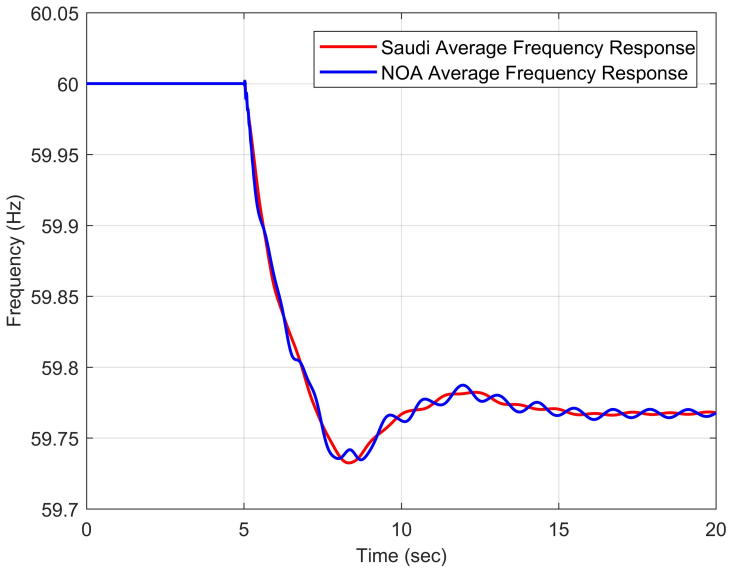


Figure 5.28: Regional and national frequency responses for 10% PV penetration level.

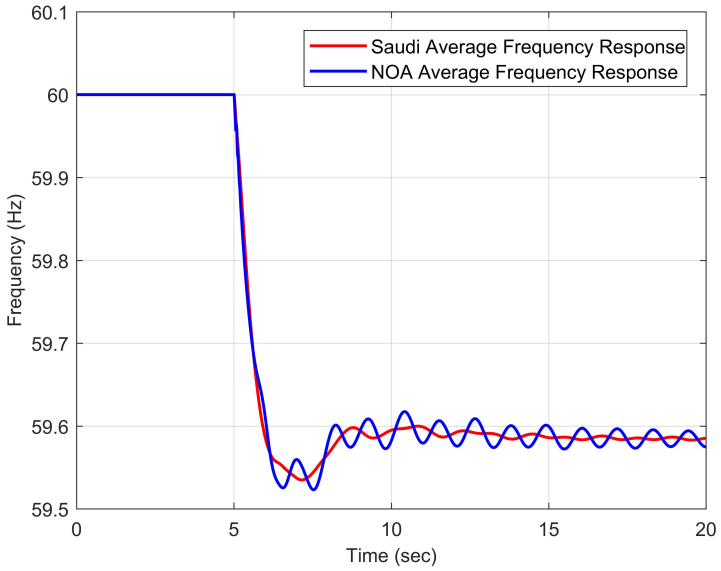


Figure 5.29: Regional and national frequency responses for 65% PV penetration level.

It is found that the Saudi system can tolerate tripping about 35% of the solar generation in the NOA without losing its stability. More than one gigawatts of the PV generation in the NOA are tripped out simultaneously at time t = 5 sec. Figure 5.30 shows the system frequency when five of the PV solar units in the NOA are tripped.

It can be noticed that tripping such PV plants generated noticeable oscillations in both the frequency response. Although the frequency response in Figure 5.30 is significantly reduced, there is still enough margin for the grid to avoid Under-frequency load shedding actions.

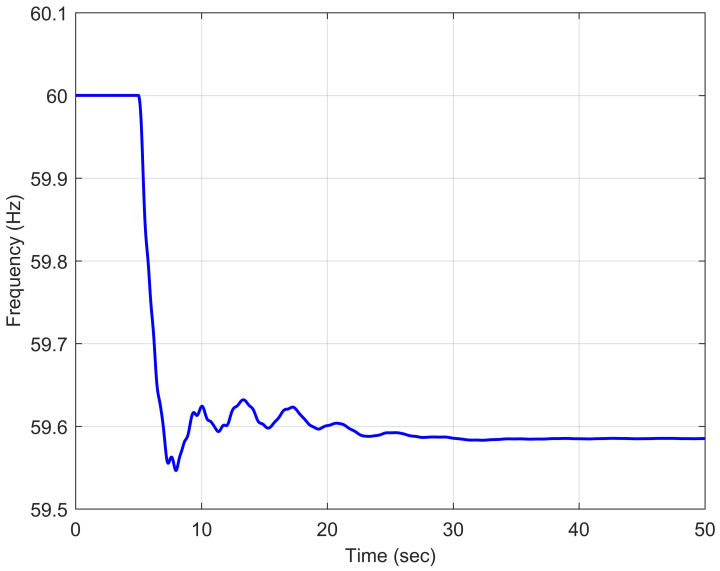


Figure 5.30: Frequency response after tripping 1 GW of PV units in the NOA.

Even though cloudy days are rarely observed in the northern part of Saudi Arabia, this scenario (i.e., all of PVs trip offline) is likely to happen in the winter season for a few days. It is important to anticipate losing all PV plants at the same time and prepare preventive actions to alleviate the associated impact, and hence improve system reliability. One recommended practice is to increase the generation in the NOA by building other renewable

power plants (e.g., wind plants) or at least keeping some of the existing conventional generation units. However, this action might not be financially feasible. Another suggested way to prevent this situation is taking advantage of the proposed HVDC link that will connect the Saudi and the Egyptian grids. This line can be used to transport extra power from the western operating area to the NOA. Transferring adequate power to the NOA to reinforce the reliability and security of the NOA grid must be considered one of the main objectives of the HVDC line between Saudi Arabian and Egyptian grids. It is worth mentioning that the NOA will be the most beneficiary of the power exchange between the two countries.

5.3.7 Improving the Frequency Response by Using Mitigation Methods

As previously mentioned, in the higher PV integration case, solar generation units cannot provide any frequency support. In order to improve the frequency response decline that results in triggering the under frequency load shedding relays as shown in section 5.3.5 for high PV penetration scenarios, two frequency control practices are applied here.

The first practice is to increase the number of generators that are attached to active governor. As stated earlier, the original Saudi model has a total generation capacity of about 61 GW with more than 18 GW generated by machines connected with active governors. However, adding more PV units replaces the existing conventional machines and some of these displaced machines have governor response function.

According to [79], the ratio of the generation capacity that are attached to governor response to the overall system generation capacity is known as the factor K_t. The smaller

value of K_t means only few machines can respond to a grid disturbance. The fraction K_t is substantially reduced as the PV penetration level increases. For instant, the original Saudi model has a governor ratio of 29.95% that has been reduced to about 14% when most of the conventional units are dispatched to reach the 65% PV penetration scenario. At that stage, there was no consideration whether these replaced units were attached to active governors.

Most of the machines in the Saudi model are either simple-cycle or combined cycle gas units that can easily respond to under-frequency events [80]. Therefore, the number of machines that can provide governor response is increased and the governor ratio is modified as those machines put into service to restore the governor ratio to 30%. Table 5.3 summarizes the suggested cases of the governor ratios with their capacity.

Table 5.3: Governor responsive generation capacity.

Case	**Governor capacity (MW)**	**Governor ratio (%)**
Case 1	8,512.368	14
Case 2	13,397.618	22
Case 3	18,333.769	30

A plant at bus 501 in the NOA that generates 1,282 MW is tripped at five seconds and the impact of changing governor ratio is investigated. Figures 5.31 and 5.32 show the frequency responses for the three governor ratios (14%, 22%, and 30%), with 30% PV and 65% PV, respectively.

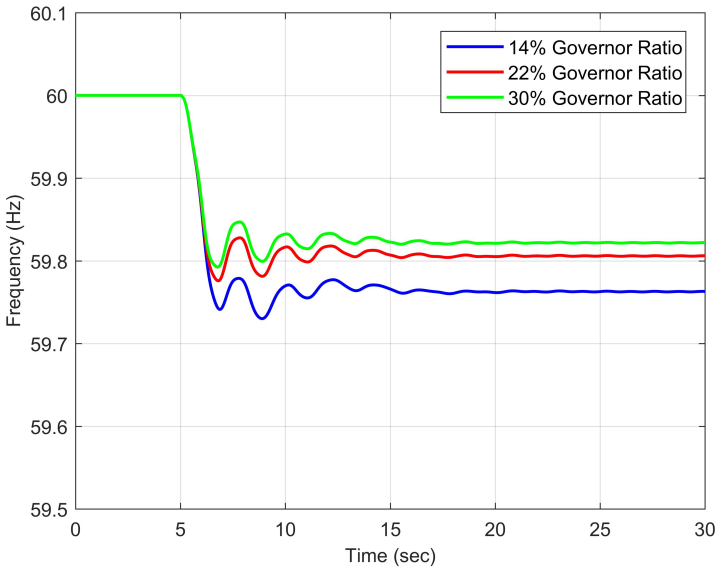


Figure 5.31: Frequency response with various governor ratios for the 30% PV case.

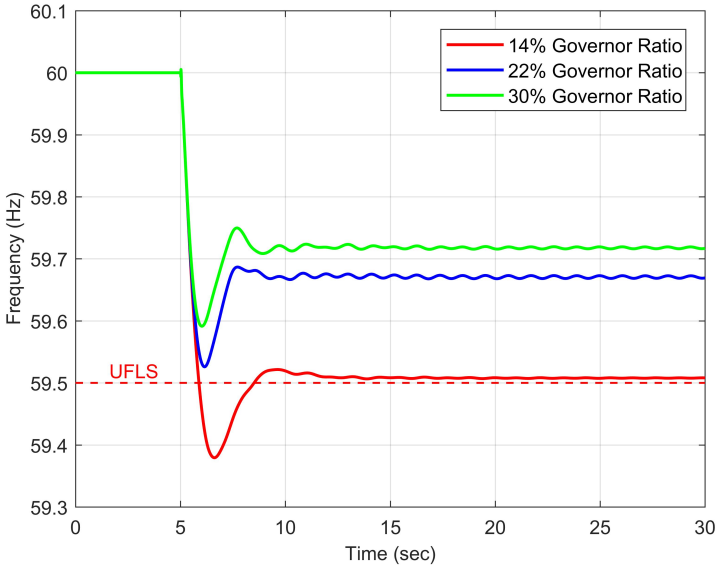


Figure 5.32: Frequency response with various governor ratios for the 65% PV case.

Compared to the original Saudi model with 65% PV when K_t is about 14%, it can be seen that increasing K_t to 30% improved both frequency nadir and the settling frequency by slightly more than 0.2 Hz as shown in Figure 5.32. This is due to the fact that more governors provide frequency support in this case.

Another possible mitigation measure of the frequency response decline would be changing governor droop of the remaining synchronous machines. The governor droop is used to speed the active governor response after an event occurs. As the value of the droop control decreases, the governor response becomes stronger.

When a power mismatch occurs due to a disturbance, frequency would drift away from the nominal value and the governor modifies the mechanical power input as required to keep the machine synchronized. Consequently, the governor droop control is used to share the loads between synchronous generators before the power system frequency goes through abnormal excursions [17, 81]. The concept of the governor droop control rate (R) is represented by:

$$R = -\frac{\Delta f}{\Delta P} \tag{5.1}$$

Where Δf and ΔP are the deviations in the system frequency and power, respectively.

In this section, the governor droop in the Saudi model is decreased from 5% to 3% for all conventional machines to investigate the impact of reduced droop control on improving the frequency response.

The same contingency is applied and the simulation results with two governor droop settings are shown in Figure 5.33 and Figure 5.34 for 30% and 65% PV penetration cases, respectively.

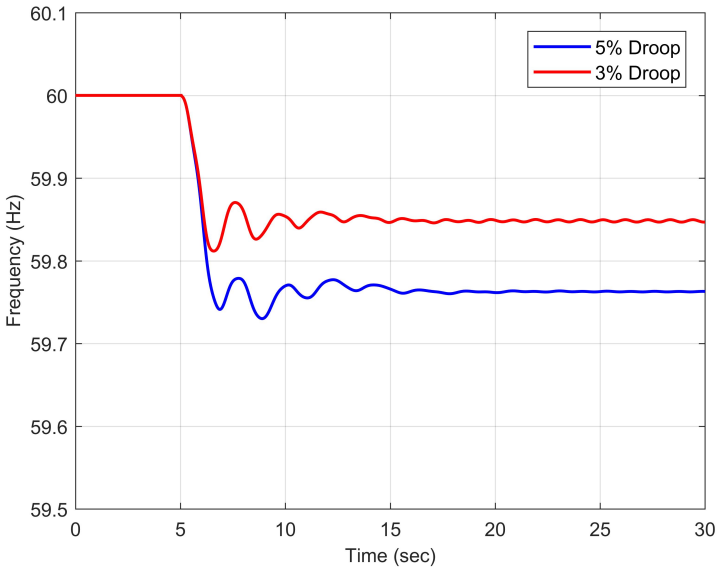


Figure 5.33: Frequency response with various governor droops for the 30% PV case.

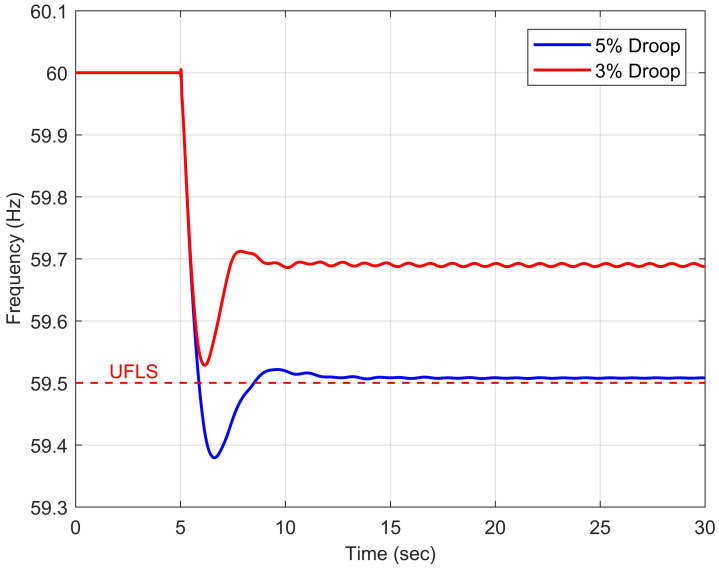


Figure 5.34: Frequency response with various governor droops for the 65% PV case.

Regarding the 65% PV penetration case, for the 3% droop case, the trip resulted in a frequency nadir of 59.53 Hz that happened at 1.16 sec after the event initiation. Clearly, the frequency nadir was improved by 0.15 Hz compared to the 5% droop.

Additionally, the settling frequency increased by 0.18 Hz when reducing the governor response speed. This can be attributed to the quick frequency support provided by responsive governors attached to the conventional units. It should be noticed that the governor droop must not be reduced below 3% or increased above 5%. Setting governor droop outside this range could result in other system instability problems [82].

The combination of the two techniques (e.g., K_t=30% and 3% droop) showed a remarkable improvement in the frequency response as can be observed in Figure 5.35 and Figure 5.36 for the two PV penetration levels. It is clear that, for the 30% PV case, the frequency nadir increased to reach 59.85 Hz and settled around 59.89 Hz, much higher than the base case. A similar scenario was experienced for the 65% PV when the frequency nadir and the settling frequency increased by 0.26 Hz.

The frequency response metrics are measured for the above techniques: increasing governor ratio and decreasing governor droop, and summarized in Tables 5.4 and 5.5. It is obvious that both techniques improved the calculated frequency metrics. The governor ratio increase and the governor droop decrease improved the system frequency nadir and the settling frequency, especially for the 65% PV penetration case. The other frequency metrics including nadir time and ROCOF were slightly decreased. Further, both measures largely improved the frequency response for the higher PV penetration case.

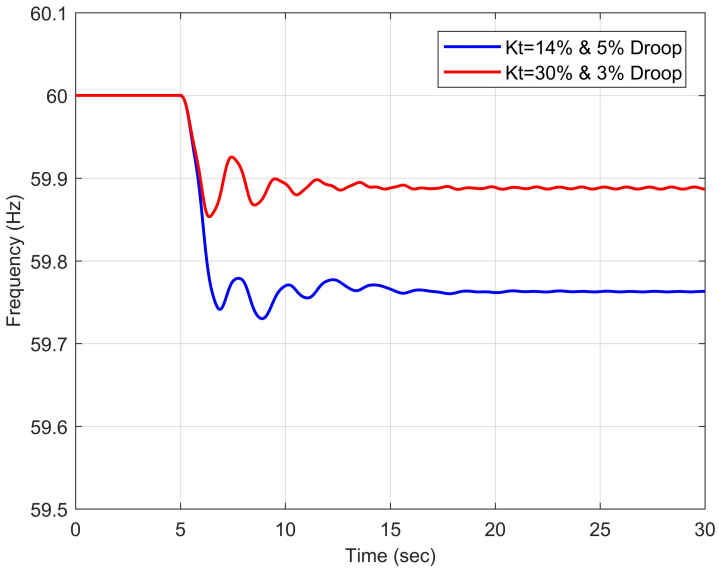


Figure 5.35: Frequency response with various governor ratios and droops for the 30% PV case.

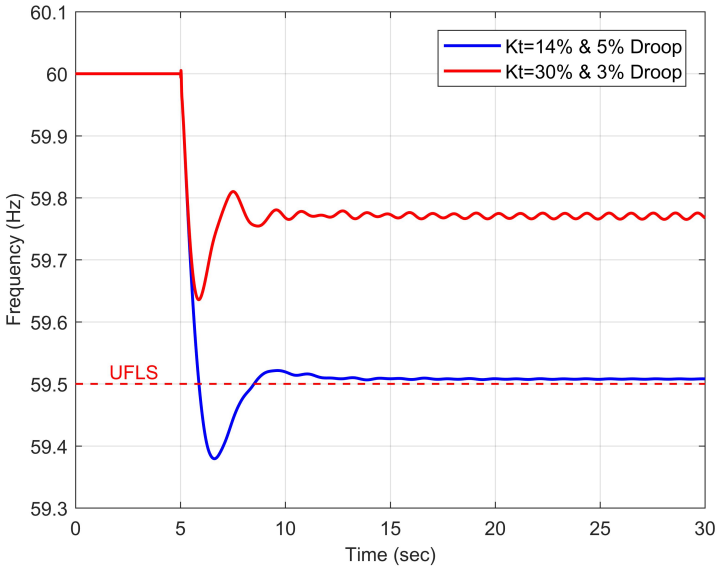


Figure 5.36: Frequency response with various governor ratios and droops for the 65% PV case.

Table 5.4: Impact of adjusting governor ratio on the frequency response metrics.

	30% PV			65% PV		
Governor ratio	**14%**	**22%**	**30%**	**14%**	**22%**	**30%**
Frequency nadir (Hz)	59.735	59.786	59.806	59.38	59.509	59.581
Settling frequency (Hz)	59.763	59.806	59.822	59.508	59.67	59.719
ROCOF (mHz/s)	0.268	0.268	0.268	0.636	0.611	0.5892
Nadir time (s)	2.825	2.742	2.758	1.617	1.258	1.208

Table 5.5: Impact of adjusting governor droop on the frequency response metrics.

	30% PV		65% PV	
Governor droop	**5%**	**3%**	**5%**	**3%**
Frequency nadir (Hz)	59.735	59.812	59.379	59.528
Settling frequency (Hz)	59.763	59.844	59.508	59.688
ROCOF (mHz/s)	0.268	0.087	0.636	0.616
Nadir time (s)	2.825	1.625	1.617	1.158

It can be concluded that increasing governor ratio (K_t) or adjusting droop control would be helpful in enhancing the primary frequency response for the higher PV integration cases. Therefore, the governor ratio must be kept above the minimum level to lessen the incremental effects of solar generation. The governor droops could be adjusted if required.

5.3.8 Energy Storage for Frequency Regulation

This section is motivated by the planned solar power project that will be finished by 2030 in Saudi Arabia. Investing in battery technology will be part of the project goals. Although the economic study of the energy storage system (ESS) is beyond the scope of this study, it is essential to appraise the proper size of energy storage capacity for some of the power system applications. The main purpose of this study is to demonstrate the effect of ESS on the system frequency under large-scale solar PV penetration and to quantify how the energy storage can provide grid frequency regulation.

As mentioned in the previous sections that a power grid operates under low system inertia constant when having high renewable energy resources due to the displacement of the conventional machines. Hence, the power system stability, specifically frequency stability, might be deteriorated leading into grid security and reliability challenges. For example, the remaining conventional units in the studied Saudi model, when reaching 65% PV penetration level, cannot provide enough frequency support, which results in activating the UFLS and shedding some loads to avoid total frequency collapse. Moreover, the intermittent power supply from PV solar units may increase the frequency deviations and further weaken the frequency stability.

There are several approaches can be used to mitigate these adverse impacts such as HVDC control and keeping the conventional units online; however, the latter is not cost effective and environment-friendly option. Therefore, Grid-scale energy storage system emerges as a contracting measure in order to enhance the frequency stability and improve the system

reliability and resiliency. Lately, the decreasing cost of ESS makes them one of the most economical and feasible solutions [83].

Generally, ESS can be utilized to store and deliver or absorb energy from or to the power grid in a very short time frame to perform useful functions. There are different types of battery technologies such as compressed air, pumped water, flywheel, and chemical batteries that include lead-acid, lithium ion, nickel cadmium, and many others. They can be placed carefully at several locations like transmission and distribution substations or near load centers [84]. ESS can provide various ancillary services; for instance, they can help in balancing generation and load, peak demand shaving, voltage regulation, spinning and non-spinning reserves, and renewable energy resources smoothing [84, 85]. However, in most system applications, ESS main function is grid frequency regulation. It can quickly control the active power transfer into and from the power grid to regulate system frequency when a disturbance occurs [86]. The response to the first frequency oscillation is crucial to maintain grid stability before UFLS intervenes; therefore, restoring the frequency stability in the first seconds after an event requires high speed ramping storage capability [87]. The response of ESS to control the frequency is quicker than thermal and hydro power plants, conventional governors, and automatic generation control (AGC) responses [81, 88]. Thus, it can rapidly reduce larger frequency deviations. Since the primary frequency regulation can be provided by a limited storage capacity [88], this study will focus on the primary frequency response.

In this study, the EPRI CBEST model in PSS®E is used to demonstrate the dynamic characteristics of the energy storage system. In power flow, the ESS is represented as a single generator connected to a selected bus. The single line diagram of the active power control of the CBEST battery model is shown in Figure 5.37. As shown in the figure, the

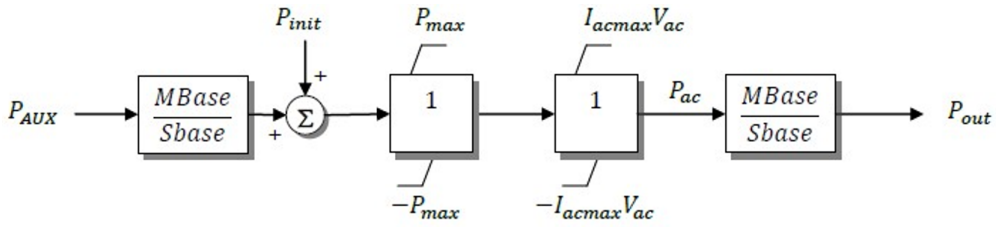


Figure 5.37: Single line diagram of active power control of the CBEST model [16].

battery power output is controlled by P_{AUX} and P_{INIT} where P_{AUX} is the input active power signal and P_{INIT} is the initial value of active power provided by power flow initials. Both quantities, expressed in MW, are used with the shown power and current limiters to provide the active power output P_{out}. In this study, P_{INIT} value is set equal to zero during power flow simulation whereas the P_{AUX} value is determined through an auxiliary signal based on the frequency deviations experiencing in the grid during a contingency (e.g., difference between measured and reference frequencies) [16, 89, 90, 91]. Typical values are used for the rest of the parameters. More details about this model can be found in [16].

In this study, a machine that generated 1.4 GW at bus 110 in the western area of the Saudi grid is tripped offline at t=1 sec with 65% of PV penetrated. First, the event is applied in the Saudi grid without ESS, then the ESS is integrated into the grid with different amounts of energy storage capacity. The first scenario is assuming that there is no limitation on the ESS stored energy. The output energy is only limited by the maximum power rating. Six battery energy storage systems (BESSs) are installed at six buses in the WOA with power ratings of 50, 100, 150, and 200 MW for each case.

The event is applied for these capacities and the system average frequency is monitored and shown in Figure 5.38. It can be seen that the BESS significantly reduced the frequency decline as expected. As compared to the original case, the frequency nadir for 1,200 MW

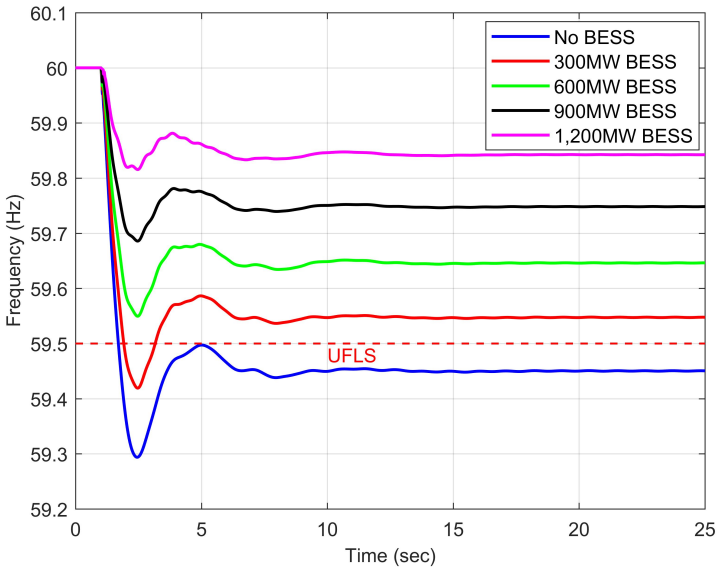
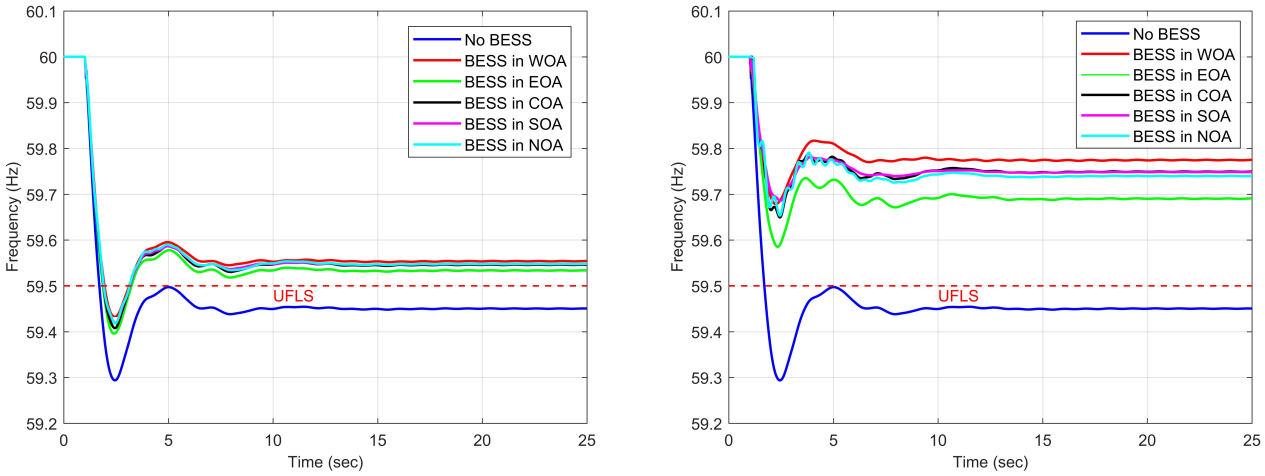


Figure 5.38: Frequency responses with unlimited BESS capacitates in the WOA.

BESS decreased by 0.52 Hz and the settling frequency was improved by 0.4 Hz. Even though all frequency profiles associated with the suggested BESS sizes showed noticeable improvements over the no-BESS case, the BESS with power ratings of 300 MW did not stop the frequency nadir from falling below the UFLS threshold. Therefore, the BESS must be sized to have power ratings of at least 30% of the largest contingency amount occurs in the area to avoid undesirable UFLS actions. In fact, it may not be economical to install more than this capacity for such an event for primary frequency control.

To determine whether the locations of the BESS influence the frequency response, the same contingency is applied while the six BESSs are installed each time in one of the four remaining operating areas (EOA, COA, SOA, and NOA). For illustrative purpose, the frequency responses of only two cases (300 MW and 900 MW BESS) are shown here in Figure 5.39. It is clear that the location of BESSs did not show major differences in the frequency behavior. This can be attributed to the small size of the Saudi grid.



(a) 300 MW BESS

(b) 900 MW BESS

Figure 5.39: Frequency responses with unlimited BESS capacity at different locations.

In order to analytically assess the impact of BESS on the system frequency stability and to compare the different BESS capacities and locations, the frequency metrics are calculated and the results are shown in Figure 5.40 through Figure 5.42 for frequency nadir, nadir time, and settling frequency, respectively. It can be observed that the incremental increase of the BESS ratings from 300 to 1,200 MW considerably improved the frequency nadir and the settling frequency while the nadir time slightly changed. It can be concluded that implementing ESS in the high solar populated grid tremendously enhances the system frequency stability.

Even though the previous scenario has shown effective improvements in the frequency response, in the real system, BESS cannot provide sustainable energy storage for permanent primary frequency regulation. Therefore, the BESS energy limitation is considered in the following scenario.

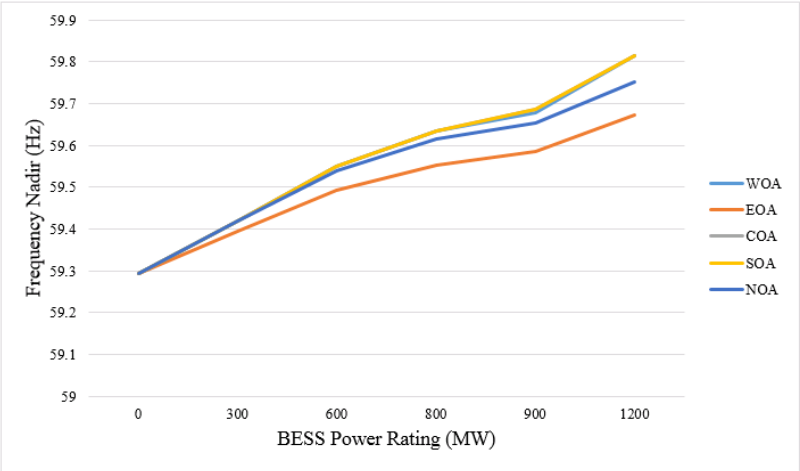


Figure 5.40: Frequency nadir with unlimited BESS capacitates at different locations.

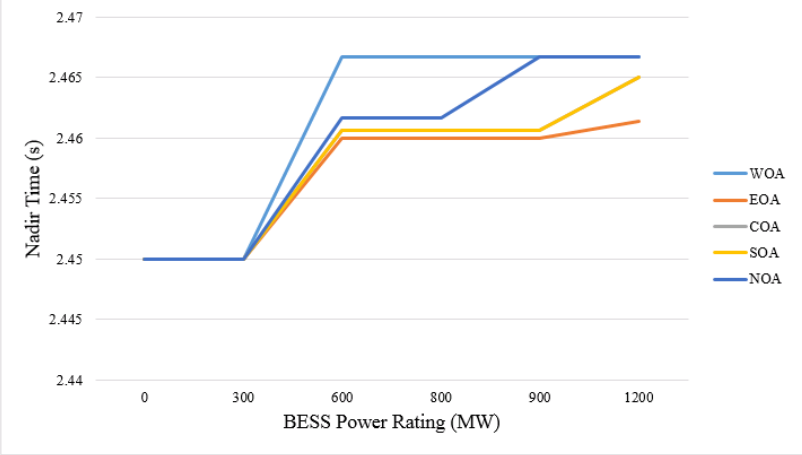


Figure 5.41: Nadir time with unlimited BESS capacitates at different locations.

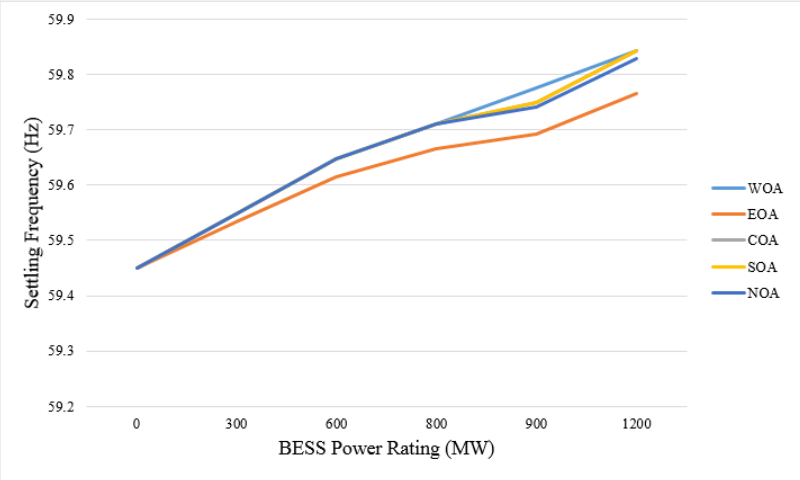


Figure 5.42: Settling frequency with unlimited BESS capacitates at different locations.

The same disturbance is applied with limited BESS power ratings and the results are shown in Figure 5.43 and Figure 5.44. During this transient, without BESS in service, the frequency nadir fell down to reach 59.29 Hz and resulted in triggering the UFLS. On the other hand, with the limited BESS, the frequency response experienced a second drop immediately after the battery ran out of its stored energy capacity. Interestingly, the frequency nadir of the second drop reduced as the amount of BESS power rating increased. Despite the fact that the frequency nadirs of all BESS power ratings were slightly higher than that of the base case, both frequency responses failed to recover above the UFLS threshold and the final steady state frequency of all cases stabilized around the same value, 59.45 Hz.

The frequency metrics of the second scenario are depicted in Figure 5.45 through Figure 5.47. It can be noticed that the frequency nadir started increasing until the frequency nadir of the second drop exceeded that of the first drop, then the frequency nadir experienced a decreased trend.

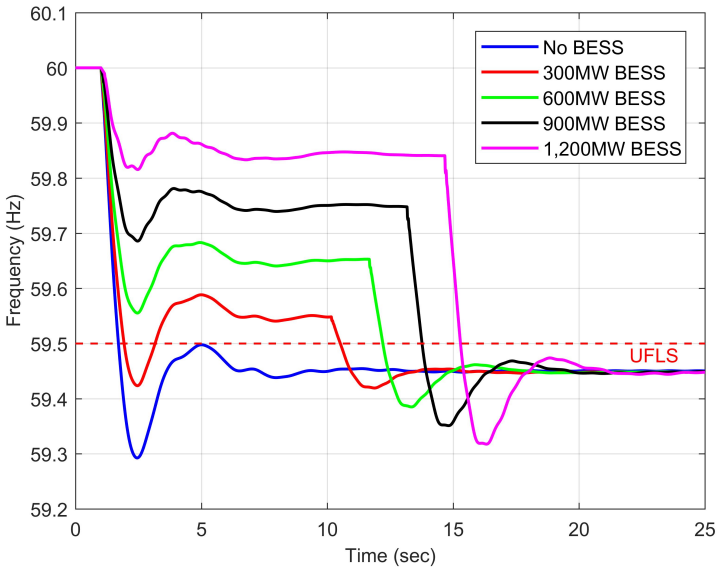
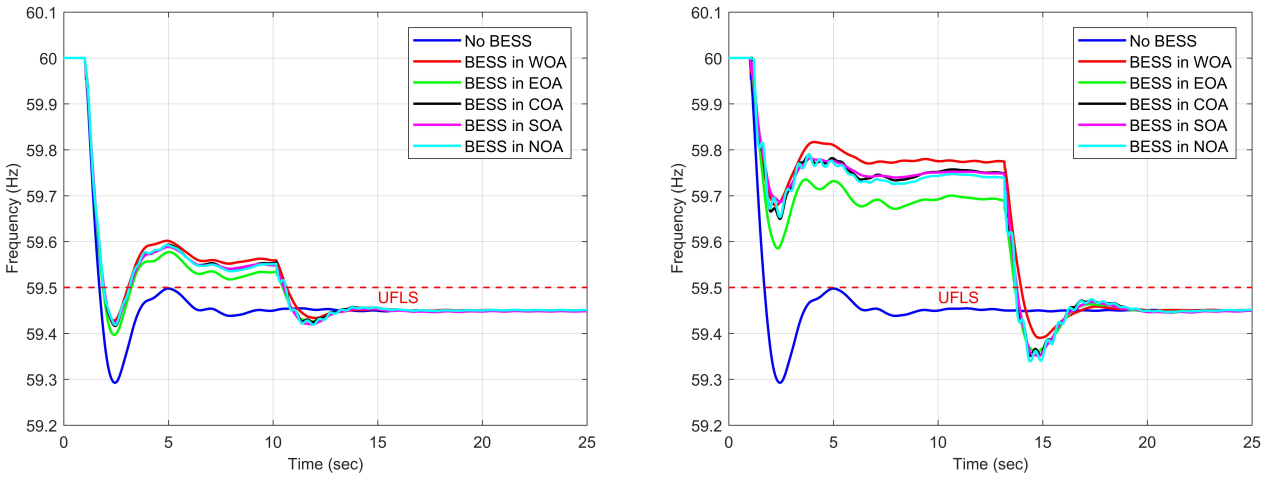


Figure 5.43: Frequency responses with limited BESS capacitates in the WOA.



(a) 300 MW BESS

(b) 900 MW BESS

Figure 5.44: Frequency responses with limited BESS capacity at different locations.

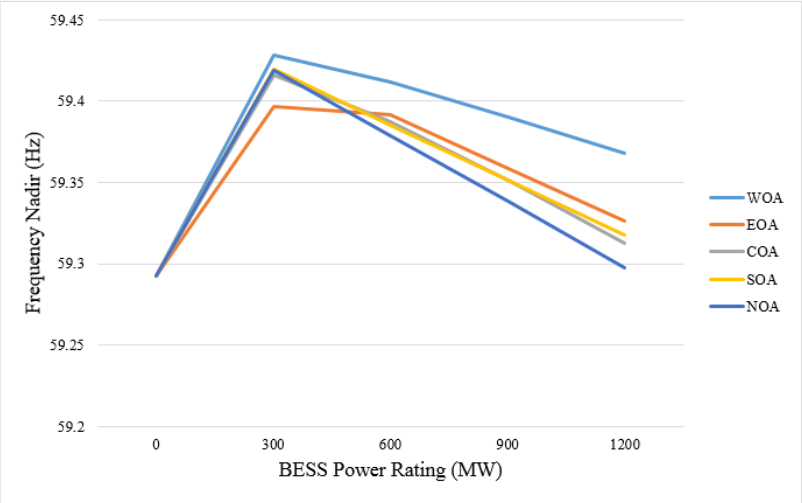


Figure 5.45: Frequency nadir with limited BESS capacitates at different locations.

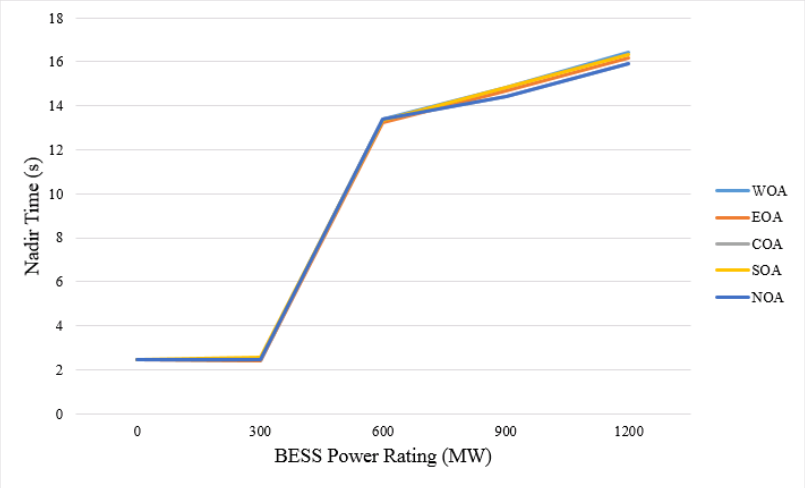


Figure 5.46: Nadir time with limited BESS capacitates at different locations.

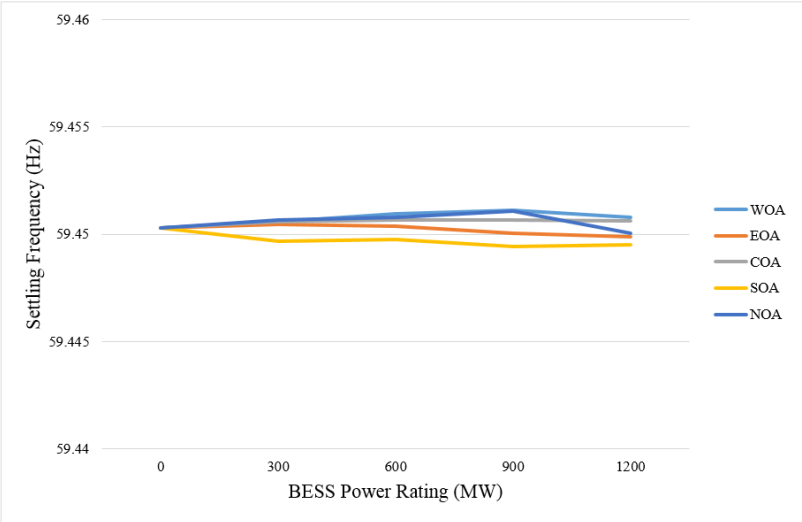


Figure 5.47: Settling frequency with limited BESS capacitates at different locations.

The nadir time was around 2.45 sec for the frequency profiles associated with small BESS capacity and increased to reach 16.5 sec for the higher BESS capacities when the second dip showed lower frequency deviation. In addition, the settling frequency of all cases fluctuated around the steady state value of 59.45 Hz, which means that the settling frequency is not sensitive to the BESS capacities when the stored energy is finite.

The effectiveness of utilizing the BESS here is that it can postpone the frequency nadir occurrence to allow some time for other frequency controls to take over such as governor response. Accordingly, this might reduce the cost of relying on expensive primary frequency control, particularly in a grid of high renewable resources. It can be concluded that the energy storage system can be a potential solution to alleviate the frequency stability challenges associated with higher PV integration. However, limited ESS shows limited frequency improvement. In fact, due to their fast actions, ESSs can be used to support the actions of the governor to restore primary frequency response right after disturbances. Further work

can be done to study the economic feasibility of incorporating ESS into the grid to provide primary frequency regulation.

5.4 Summary

This chapter explores the impact of the high solar penetration on the frequency stability of the Saudi power grid. Four PV penetration levels are introduced into the Saudi grid (10%, 30%, 50%, and 65%). The PV plants are distributed among all the operating areas by displacing the existing conventional generators. The GE PV model is utilized to illustrate the dynamic performance of the solar PV plant.

Several case studies are analyzed to show the impact of integrating high solar energy into the Saudi grid on the system frequency response:

- It has been found that tripping either large PV plant or large conventional generator during the normal operation with the high level of PV penetration could cause significant frequency stability issues in the system.

- It has been observed that the frequency response characteristic (β) decreases as the PV penetration increases due to the lower system inertia.

- It has been demonstrated that adding more renewable energy sources affects the frequency metrics as they increase the ROCOF while reducing the frequency nadir and the settling frequency. In addition, it has been found that the event location does not change the frequency response metrics significantly.

- When the system is highly populated with the solar plants, tripping large machines could impact the grid security as these events tend to trigger the under-frequency load shedding, especially in the high loaded regions.

- The northern area of the Saudi grid is assumed to be totally powered by solar energy. The local frequency response seems to follow the path of the interconnection average frequency behavior. It has been observed that about one gigawatts (e.g., 35% of the total energy) of the solar power in the NOA can be tripped at the same time without effecting the system stability significantly.

- The degradation of the frequency response can be alleviated by maximizing the number of machines with active governors and reducing the governor droop of synchronous generators.

- It has been seen that the unlimited energy storage system can successfully reduce the frequency decline and improve the frequency stability. Limited energy storage system can provide ancillary service to control the primary frequency response for a short period of time.

Chapter 6

IMPACT OF THE SOLAR PENETRATION ON THE ROTOR ANGLE STABILITY OF THE SAUDI POWER GRID

6.1 Introduction

Rotor angle stability can be defined as the ability of synchronous machines in a power grid to maintain synchronism when a disturbance occurs. It can be divided into transient stability and small signal stability. Transient stability can be defined as the system stability when a large disturbance occurs while small signal stability is the system stability after a small disturbance such as a tiny change in generation or load [92]. This instability usually occurs

due to inadequacy of either damping torque or synchronizing torque. Inadequate damping torque leads to increasing oscillations while the shortage of synchronizing torque causes increasing in rotor angles [27].

Even though the rotor angle stability challenges are not associated with solar planets, their impact of reducing the overall system inertia could change the operating point and influence the rotor angle stability margin for the other synchronous machines. Thus, this chapter sheds light mainly on the possible impact on the Saudi power grid rotor angle stability after introducing different levels of PV penetration. The transient stability of the Saudi grid under high solar is studied in terms of critical clearing time index and power angle-based stability margin. Further, the influence of the higher PV integration on the inter-area oscillation modes is analyzed in this chapter.

6.2 Impact on Critical Clearing Time

The purpose of this section is to analyze the transient stability of Saudi power grid using Critical Clearing Time (CCT) approach to measure the contingency severity applied to the system when integrating large-scale solar power units.

CCT index is used to assess the limit of system transient stability under different types of disturbances and to ensure the system is capable of maintaining synchronism after these events. CCT can be defined as the largest allowable duration for a disturbance to sustain before it is cleared such that the system does not lose its synchronization [93, 94]. CCT is determined by monitoring the rotor angle deviation of a synchronous generator. Therefore,

it is the time just before the rotor speed dramatically accelerates and does not return to a stable point [95].

Recently, power grid is going through a process of development, such as the retirement of the conventional generation units and the increase of renewable energy sources, which changes its dynamic behavior. These developments would create security and stability challenges that may affect the transient stability of a network. As a result, the rotor angle stability characterized through the CCT could be influenced with the increase of PV penetration that may cause protection system issues and impact network security.

In the recent literature, the relationship between the CCT and wind power has been studied in some research [96, 97, 98, 99, 100, 101]. Most of these studies recommended alteration in the critical clearing time when more wind energy is penetrated in the grid. In [99], the CCT is investigated in an isolated grid with wind power. The study found that the CCT values decreased as the wind power increased. Studies in [102, 103] demonstrated that the CCT value improved with more wind turbines integrated. A study by Y. Wua et al. examined the impact of integrating large-scale wind farms into a grid on the CCT [104]. Simulation results indicated that integrating large-scale wind plants did not violate Taipower's transmission system guidelines in terms of CCT even though the system CCT values fluctuated based on the capacity and the direction of power flow. Although there is already a considerable number of literature investigating the effect of wind farms on the CCT, there has been relatively little work done on the relationship between the higher PV penetration and the transient stability in terms of CCT. The author in [105] discussed the impact of solar power penetration on the transient stability, mainly the CCT metric, using 11-bus system, and concluded that the transient stability deteriorated as the PV penetration

level increased. Using simple multi-machine power system, ref [106] analyzed the impact of solar and wind models on the system transient stability. The study revealed that the increase in solar generation capacity reduced the CCT.

The CCT calculation methodology includes a standardized trial and error approach. This can be done by performing dynamic time domain stability simulations and applying a contingency in a grid, then gradually increasing the fault duration by a small time step until the rotor angle goes out of step or the system loses synchronism. Thus, the maximum duration time of the fault to maintain the synchronization in the entire power grid can be called the critical clearing time (t_{cr}). Although there are many proposed approaches to estimate the CCT [94, 107, 108, 109], the trial and error technique using dynamic simulation proves to be effective and accurate for estimating the CCT [99]. The contingency used in this study is a typical three-phase line fault on the important transmission lines. The event can be cleared by tripping the line.

Nevertheless, the CCT is not the only measurement for examining the grid transient stability. There is another parameter that is used to evaluate the transient stability margin of the system, which is the power angle-based stability margin (AM). It can provide a wider vision about the stability limits as it can determine the distance to the system instability for a specific condition [110]. According to [111], the AM index can be calculated as follows:

$$\eta = \frac{360 - \delta_{max}}{360 + \delta_{max}} \times 100 \qquad -100 > \eta > 100 \tag{6.1}$$

Where (δ_{max}) is the maximum difference between any two synchronous units' rotor angles at the same time. The network is considered transiently stable if the AM value is not less than zero.

Although the network might be stable after an even, the response of a machine in the proximity of the disturbance could show insecure dynamic behavior. Therefore, AM is used as a security indicator by a predefined threshold based on the system operator criteria. Generally, 180 degrees (i.e., $\eta = 33.33\%$) is used as a threshold to check the security condition of the system. Some references use 90 degrees as a security threshold [110, 111].

A screening procedure is conducted to choose the transmission lines that have the highest power flow within and between the five operating regions. As a result, ten transmission lines (e.g., five in each region and the other five are connecting these regions) are selected as candidates to perform this study. These transmission lines with their active and reactive power flow are shown in Table 6.1.

In this section, in each simulation process, the three-phase fault is applied separately at each of the ten selected transmission lines at time (t=5.0 sec). To clear the fault, both ends of the faulted line are opened simultaneously. Next, the changes and differences of the CCT value are checked for the four PV penetration levels (10%, 30%, 50%, and 65%) and compared with the original grid model when there is no PV unit connected. At the same time, the rotor angle of each synchronous machine is monitored and the AM index is calculated.

Table 6.2 summarizes the CCT values obtained for the ten cases with all PV penetration levels. It is obvious that there is a gradual decrease in the CCT when more solar power is integrated into the grid. This progressive decrease can be attributed to the decrease in

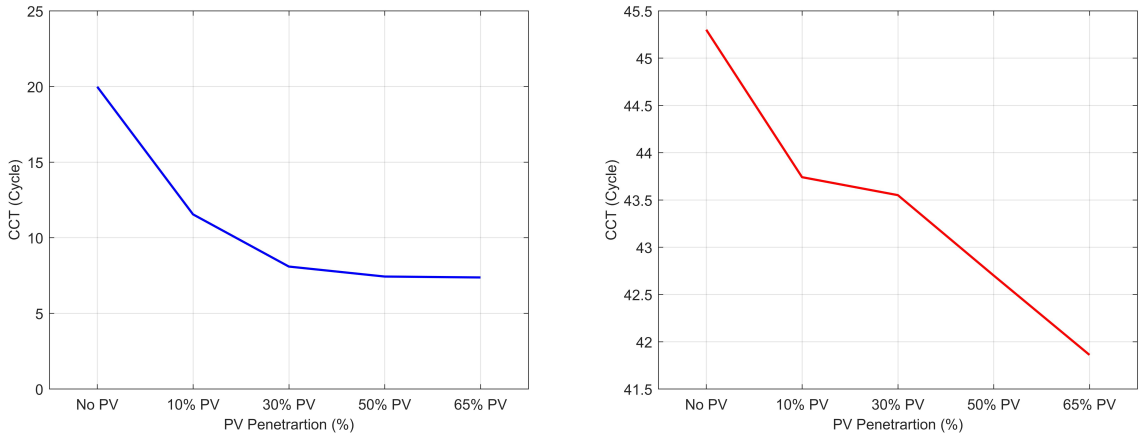
Table 6.1: Transmission lines with highest power flow.

Operating area	Transmission line	Active power flow (MW)	Reactive power flow (Mvar)
WOA	102-116	1225.1	228.6
EOA	214-223	505.80	70.00
COA	313-315	1251.4	213.1
SOA	401-403	768.70	257.5
NOA	501-502	551.00	19.80
WOA-COA	109-311	465.20	125.0
WOA-SOA	105-401	158.10	118.4
WOA-NOA	111-503	43.900	5.270
EOA-COA	215-301	1265.7	396.0
COA-NOA	312-507	352.80	44.40

Table 6.2: Comparison of CCTs values for the ten cases (Unit: Cycle).

Area	No PV	10% PV	30% PV	50% PV	65% PV
WOA	19.98	11.54	8.090	7.430	7.370
EOA	27.20	27.20	27.14	27.02	26.96
COA	10.20	8.960	7.080	6.480	5.580
SOA	21.48	21.48	20.94	20.52	20.46
NOA	21.96	20.42	19.92	19.92	19.22
WOA-COA	45.30	43.74	43.55	42.70	41.86
WOA-SOA	59.46	58.62	57.78	57.72	54.60
WOA-NOA	84.90	84.18	83.78	83.20	82.70
EOA-COA	13.50	13.50	12.00	10.98	9.480
COA-NOA	58.68	58.20	54.66	52.18	52.18

the number of online synchronous machines that leads to the total power system inertia reduction. Due to the space limitation, only two cases are presented in Figure 6.1 that shows graphical representations of the CCT changes with different PV levels for faults in the WOA and on the tie line connecting WOA and COA.

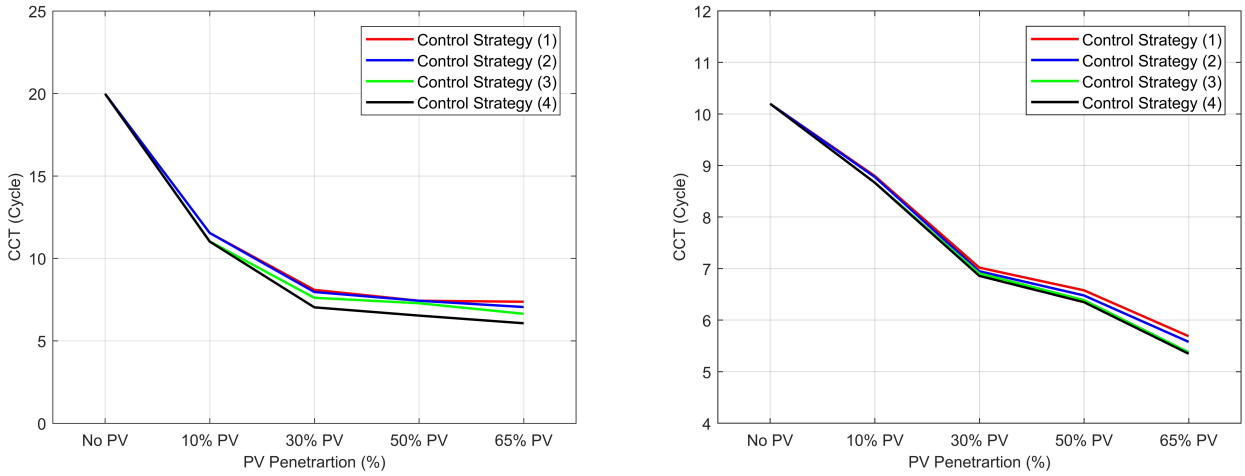


(a) Fault on the transmission line in WOA (b) Fault on the tie line between WOA and COA

Figure 6.1: Critical clearing time (CCT) changes with different PV penetration levels.

Figure 6.2 shows the differences between CCT values with four different voltage control strategies for the PV model mentioned in section 5.2.1 for the two cases in the WOA and COA. It can be seen that there is a slight difference in the CCT values with all control strategies, especially for the higher PV levels. The CCT value for the PV model with control strategy (1) is about 5.98% higher than the other control strategies.

For the disturbance in the COA, as shown in Figure 6.3a, the fault lasted for 5.58 cycles, which equals the CCT value for the 65% PV penetration scenario. It is clear that the rotor angle returned to its original value after a period of time without losing its stability before or after integrating solar energy into the system. However, when the fault duration increased by one cycle (e.g., the fault was cleared after 6.58 cycles), the rotor angle still remained



(a) WOA

(b) COA

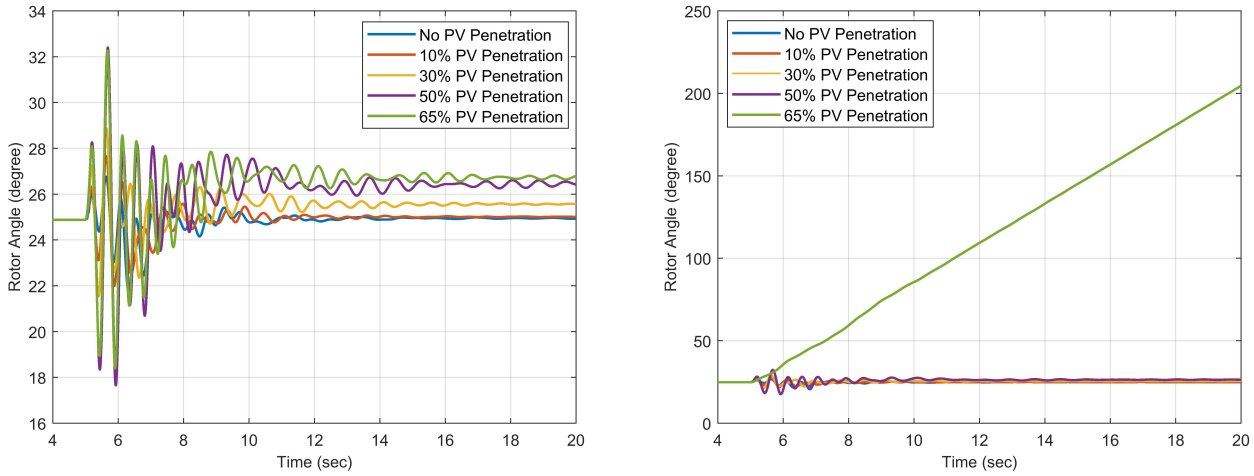
Figure 6.2: Critical clearing time (CCT) changes with different voltage control strategies.

under control for the all PV penetration levels except for the 65% PV case when the rotor angle ran far away as shown in Figure 6.3b, causing transient instability. Figure 6.4 presents the rotor angle response of a machine in the WOA to the minimum CCT associated with the 30% PV case. It is obvious that the rotor angle diverged from a stable point and never returned for the 30%, 50% and 65% PV penetration levels.

The AM index is calculated out for all ten cases and the comparison of the maximum angle separation and the corresponding AM indices are presented in Table 6.3.

From Table 6.3, it can be noticed that the AM index decreased to some extent as more solar plants were penetrated into the grid.

In order to clearly observe the impact of integrating solar energy on the power angle-based stability margin, comparisons are made between 0% and 65% PV penetration levels. Figure 6.5 and Figure 6.6 show the oscillations of the rotor angles of the synchronous units in the WOA and EOA, respectively.



(a) Fault lasted for 5.58 cycles

(b) Fault lasted for 6.58 cycles

Figure 6.3: Rotor angle oscillations of a machine in the COA with different penetration levels.

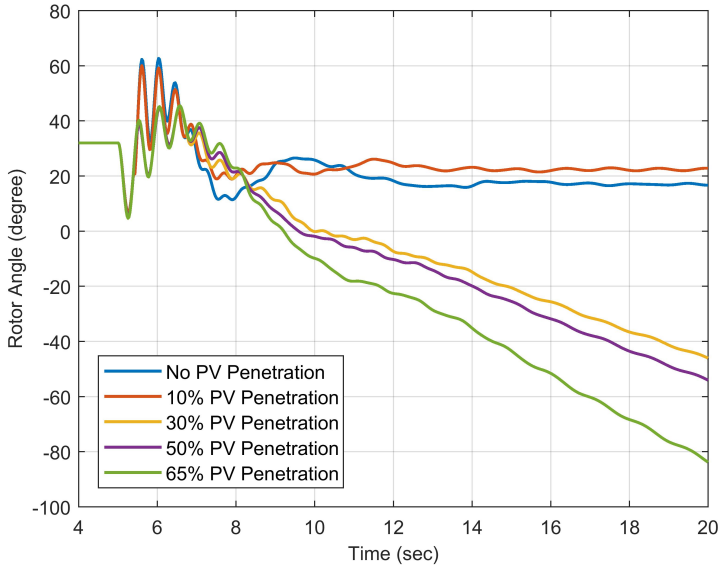


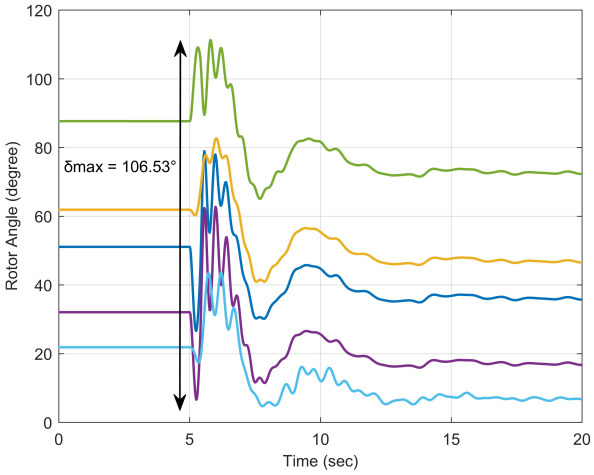
Figure 6.4: Rotor angle oscillations of a machine in the WOA with different penetration levels when a fault lasted for 8.10 cycles.

Table 6.3: AM transient stability index for the ten cases.

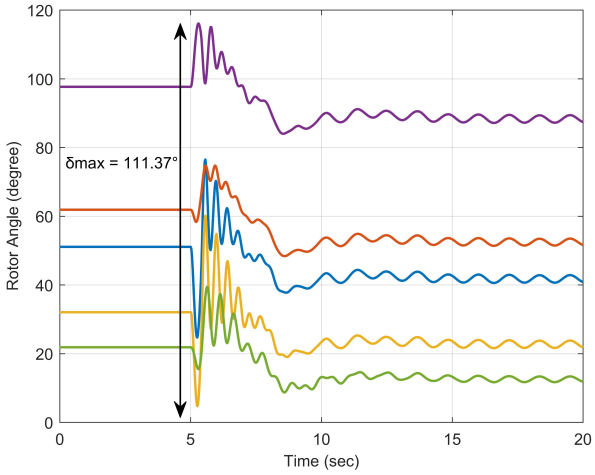
Area	**No PV**		**10% PV**		**30% PV**		**50% PV**		**65% PV**	
	δ_{max}	η	δ_{max}	η	δ_{max}	η	δ_{max}	η	δ_{max}	η
	deg.	(%)	*deg.*	(%)	*deg.*	(%)	*deg.*	(%)	*deg.*	(%)
WOA	106.53	54.33	106.95	54.19	106.95	54.19	109.17	53.46	111.37	52.75
EOA	81.52	63.07	84.12	62.12	86.64	61.20	87.03	61.06	89.07	60.33
COA	107.26	54.09	113.39	52.09	115.62	51.38	116.96	50.96	131.68	46.44
SOA	134.08	45.72	142.28	43.34	167.95	36.38	171.68	35.42	171.96	35.39
NOA	107.66	53.96	135.67	45.26	140.29	43.92	148.01	41.73	159.10	38.70
WOA-COA	130.21	46.88	135.16	45.41	148.37	41.63	150.43	41.06	155.80	39.59
WOA-SOA	115.16	51.53	121.84	49.43	121.97	49.39	123.76	48.83	125.56	48.28
WOA-NOA	47.92	76.51	48.81	76.12	49.16	75.97	49.95	75.63	50.41	75.43
EOA-COA	64.63	69.56	72.50	66.47	117.44	50.80	120.32	49.90	126.91	47.87
COA-NOA	60.73	71.13	82.77	62.61	94.96	58.26	110.52	53.02	124.55	48.59

It is observed that maximum angle separation increased by 4.54% and 9.26% for the WOA and EOA, respectively, as the PV penetration reached 65% PV level.

According to the analytical results, it can be concluded that the increasing capacity of solar plants apparently deteriorates the transient stability performance by reducing the critical clearing time (CCT) and the power angle-based stability margin (AM). Thereby, improvement strategies could be made to maximize the security and reliability of the grid; for example, protective relays settings should be selected properly to quickly clear the fault in order to keep machines synchronized when more large-scale PV plants are integrated.

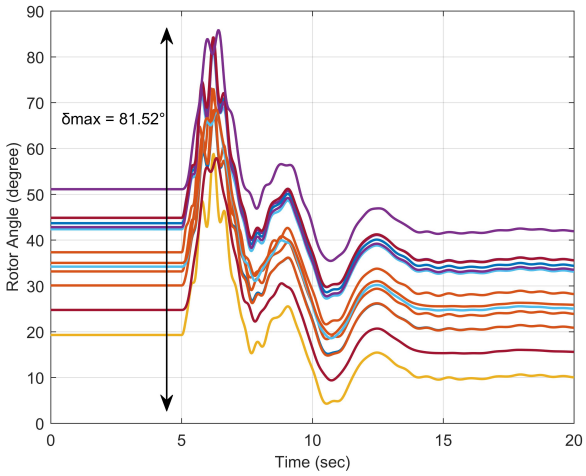


(a) No PV Case

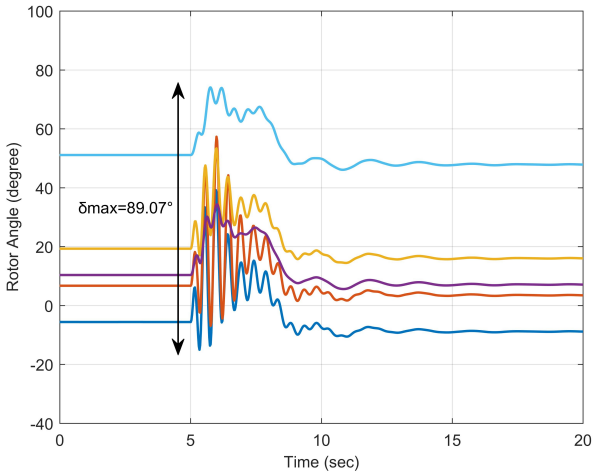


(b) 65% PV Case

Figure 6.5: Oscillations of synchronous machines rotor angles after applying a fault in the WOA.



(a) No PV Case



(b) 65% PV Case

Figure 6.6: Oscillations of synchronous machines rotor angles after applying a fault in the EOA.

6.3 Impact on Inter-Area Oscillations

The primary purpose of this section is to examine the potential impact of high penetration of large-scale solar farm on the small signal oscillation stability of the Saudi power grid. It mainly investigates power grid small-signal stability looking at oscillation frequency, oscillations damping ratio, and mode shape of the oscillations in accordance with the solar energy integration.

It is well-known that the small signal stability is the ability of the network to remain synchronized when a small disturbance occurs in the grid. This disturbance could be a little change in demands or generations or modification in the grid topology [112]. The small signal stability analysis is important to evaluate the power system electromechanical modes of oscillations, including inter-area and intra area oscillations within and between synchronous generators [113]. The small signal instability usually happens in the power electric system mainly due to insufficient damping torque that leads to the system low frequency oscillations, which are usually between 0.2 and 2.0 Hz [27, 112, 114].

It is also known that the operation and dynamic characteristics of the solar generation are considerably different from the conventional fossil-fuel power machines. Solar PV units are linked to the electrical network through power electronic interface; hence, they do not possess a rotating shaft. This means that they do not have inertia like synchronous generators that can help to damp power system oscillations after disturbances. This difference may result in a significant impact on the grid stability. Although solar PV units do not participate in electromechanical oscillation modes directly, they can dramatically alter the electromechanical damping characteristics through the interaction of their controllers with

the other synchronous machines damping torque [115, 116]. Moreover, the unpredictable output power from the solar plants may change the operating conditions of the grid that can be translated into a huge impact on the small signal stability [81]. Additionally, as more PV plants are added to the existing grid, a number of conventional units would be displaced and retired, which results in reducing the system overall inertia. This changes the power flow pattern that could lead to alteration of the oscillation damping [117]. This poorly damped oscillations may result in reducing transmission line carrying capacity, triggering protective devices, damaging generation equipment, and effecting grid security and reliability. Therefore, a thorough study on the impact and the issues of increased penetration of PV units on power system stability should be conducted.

Even though there is some literature addressing the impact of renewable energy on the small signal stability, there is no final conclusion about the small signal stability performance when introducing renewable generations. A study in [118] observed that the system oscillations damping increased as the wind power penetration increased. The system stability margin is found to be improved after integrating distributed solar and wind generation into the grid [119]. Additionally, connecting solar PV units into IEEE-14 bus test system relatively improved the small signal stability [120]. Krismanto et al. in [121] observed that the solar PV and wind energy could positively impact the small signal stability when integrated into a micro-grid. Ref [122] indicates that the mode frequency increased while the damping ratio did not change when more PV units were penetrated. Also, wind generators positively influenced the inter-area damping modes as shown in [123]. Other studies in [124, 125, 126] show that the system inter-area oscillation stability can be affected either beneficially or detrimentally based on the system operating conditions. On the other

hand, a study in [127] shows that the inter-area oscillations mode was negatively impacted as more PV units were connected to the grid. Another study found that 50% increase of large-scale and rooftop PVs resulted in reducing the oscillation damping [117]. Moreover, ref in [128] shows that the penetration of wind power negatively affected the grid small signal stability.

Based on the dynamic response of the power grid to a disturbance, matrix pencil (MP) method is carried out to obtain the crucial information about the critical modes and their relative phase, oscillation frequency and system damping [129]. This information can be used to evaluate the stability margin and to find the low frequency oscillations information.

The matrix pencil can evaluate the oscillations in a given waveform by a summation of complex exponential. It can be described as follows [17, 130]:

$$y(t) = \sum_{i}^{n} a_i \ \exp(b_i t) \ \cos(\omega_i t + \Theta_i) \tag{6.2}$$

Where

$y(t) = oscillatory\ waveform$

$n = number\ of\ desired\ modes$

$a_i = initial\ amplitude\ of\ the\ i^{th}\ mode$

$b_i = damping\ \ factor\ of\ the\ i^{th}\ mode$

$\omega_i = oscillation\ \ frequency\ of\ the\ i^{th}\ mode$

$\Theta_i = initial\ phase\ of\ the\ i^{th}\ mode$

A Hankel matrix is firstly used to find the eigenvalues and the associated eigenvectors of the input waveform. Then, the matrix pencil method employs the singular value

decomposition (SVD) to determine the desired modes based on a predefined threshold. Any values below the threshold are ignored. Finally, the least square equation is used to extract the modal parameters [17, 129, 131].

In each operating area in the Saudi grid, a conventional machine is tripped to excite the most critical inter-area modes. Then, the frequency response is recorded at five locations in each area. Figure 6.7 shows the locations of the tripped generators as well as the selected frequency measurement locations. The obtained frequency signals are used as the input to the matrix pencil analysis to determine the critical oscillation modes with corresponding oscillation frequencies and damping ratios. The intended oscillation modes have the frequency in the range of 0.1 to 2.0 Hz. The aforementioned approach is considered, firstly, for the base case of the Saudi system without PV penetration, then with introducing several PV penetration levels (e.g., 10%, 30%, 50%, and 65%) to compare the pattern of the oscillation modes with the increase of PV generation. Therefore, the impact of solar penetration on the Saudi grid small signal stability is investigated.

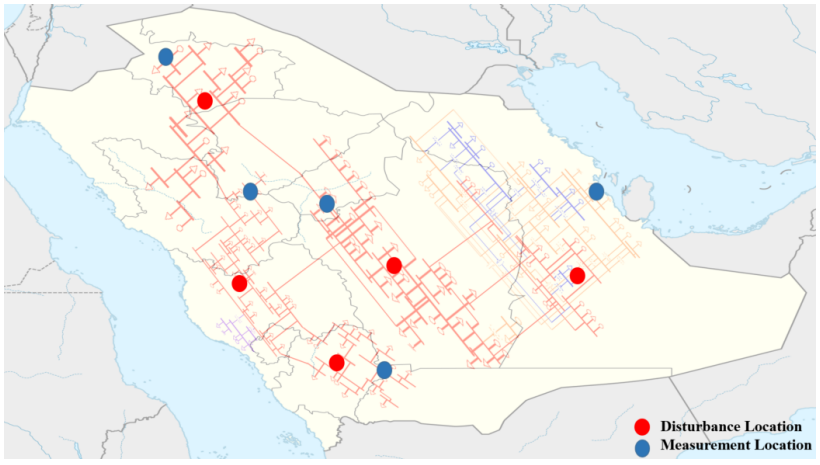


Figure 6.7: Tripped generators and observation locations.

After applying the above scenario, two oscillation modes are considered critical as they have been observed in the base case as well as the four proposed PV penetration levels. These two modes have oscillation frequencies of 0.83 Hz and 0.39 Hz. Table 6.4 summarizes the information about these modes. The impact of the increased PV penetration on the selected two modes is shown in Figure 6.8 through Figure 6.11 for both oscillation frequency and damping ratios.

Table 6.4: Oscillation frequency and damping ratio of the critical modes for the base case.

Mode number	**Frequency (Hz)**	**Damping ratio (%)**
Mode 1	0.83	7.88
Mode 2	0.39	0.89

It can be clearly seen that as the amount of PV generation increased, the average oscillation frequency increased by about 0.06 Hz and 0.088 Hz for modes 1 and 2, respectively. On the other hand, the average damping ratio considerably decreased to 4.90% and 0.44% for both modes. Based on these results, it can be concluded that higher PV penetration results in a slight increase in the oscillation frequency of the inter-area mode and reduction in the damping factor regardless of the location of the disturbance as well as the PV penetration level. This is mainly in consequence of the overall system inertia reduction associated with the displacement of the synchronous generation units. Therefore, the critical conventional machines should not be replaced in order to provide adequate damping of the inter-area oscillation modes during higher solar penetration.

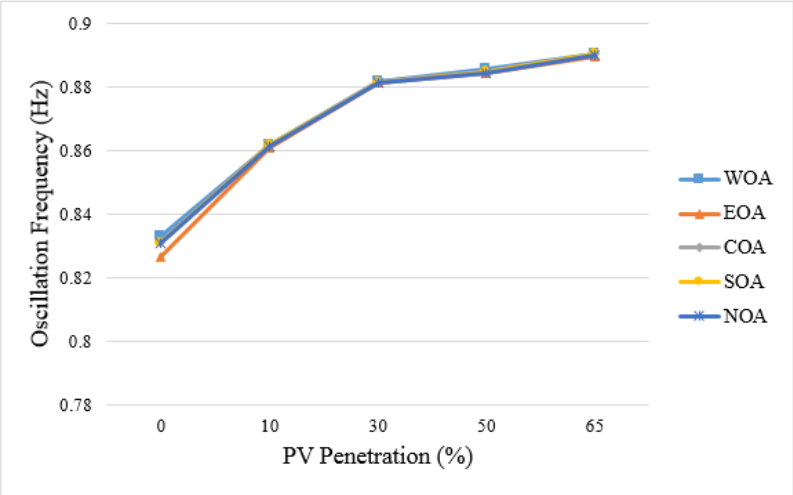


Figure 6.8: Mode 1 inter-area oscillation frequency.

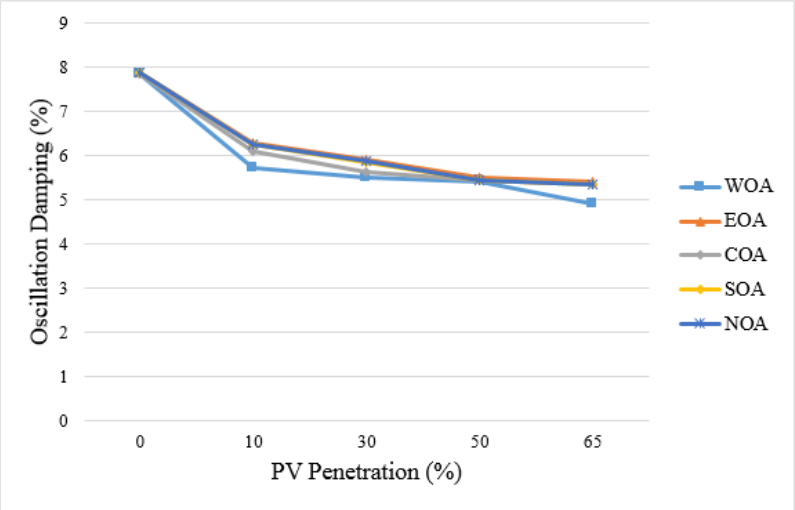


Figure 6.9: Mode 1 inter-area oscillation damping ratio.

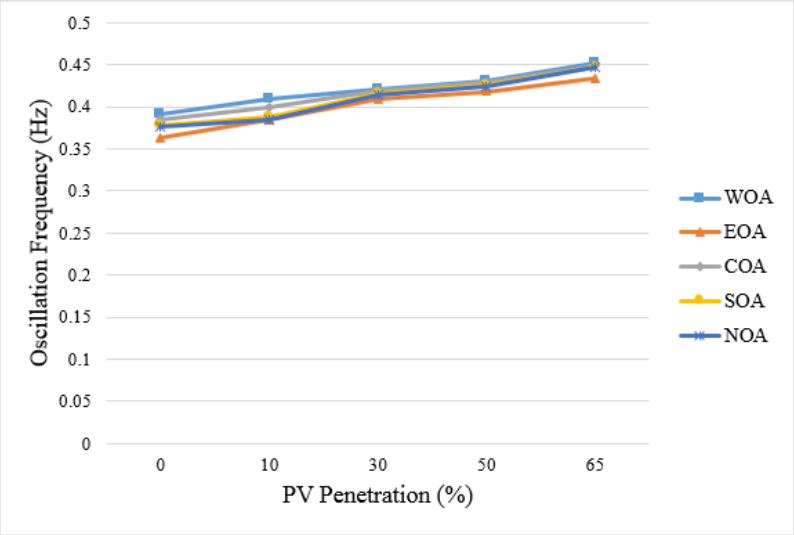


Figure 6.10: Mode 2 inter-area oscillation frequency.

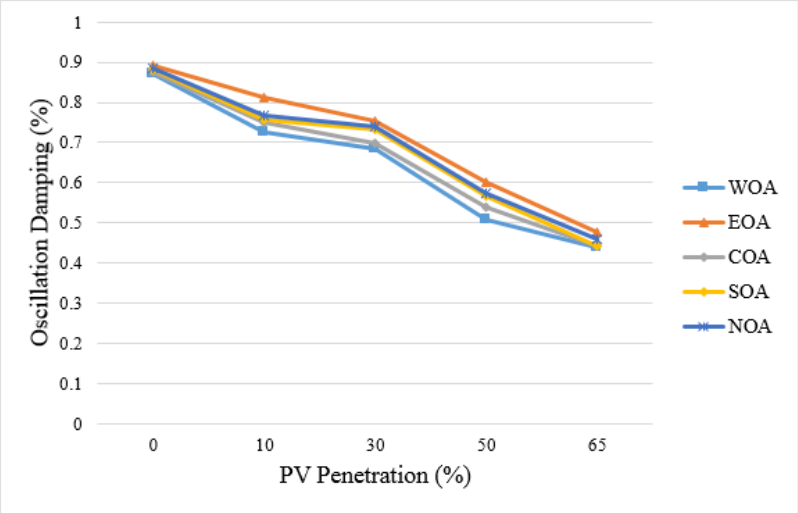
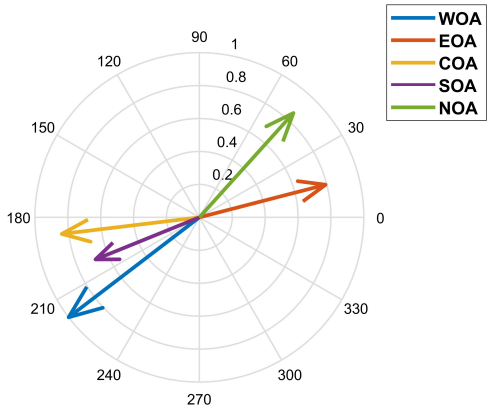


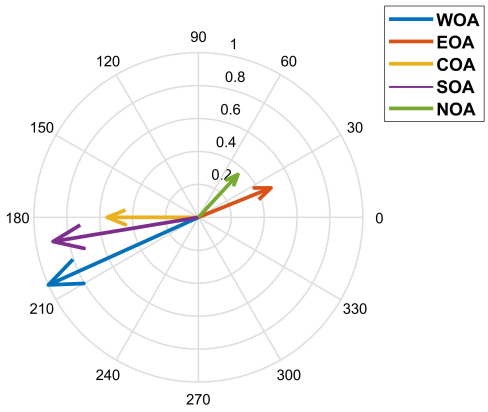
Figure 6.11: Mode 2 inter-area oscillation damping ratio.

Mode shapes can be used to provide a graphical representation of the inter-area oscillation mode. Figure 6.12 and Figure 6.13 depict the oscillation mode shapes for all PV penetration cases for the two determined critical modes. These plots show that the gradual increase of PV units could change the mode shape of the inter-area oscillations. As shown in Figure 6.12, it can be observed that the buses in the eastern and the northern areas oscillated against the other three buses in WOA, COA, and SOA. The distance between these buses started to decrease as more power being supplied from solar plants. The two groups became totally anti-phase for the 65% PV penetration level. The same trend can be observed in Figure 6.13 for Mode 2. In this case, the buses in EOA and COA oscillated against the other buses in WOA, SOA, and NOA.

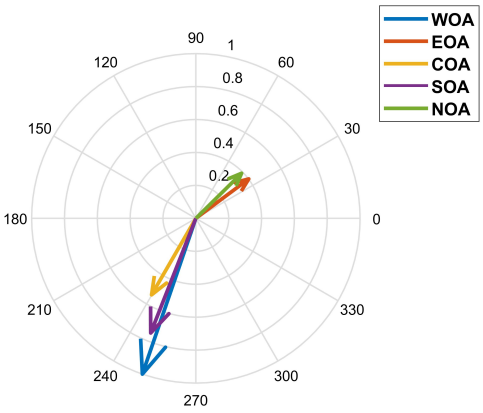
To understand the impact of the PV voltage control model, the four control strategies of the PV model, presented in Table B.1 in Appendix B, are employed in all PV plants in the Saudi grid model, and the same approach of determining the impact on the inter-area oscillation modes is applied. Similar patterns are observed for all control strategies as the oscillation frequency increases while the damping ratio decreases with the increase of the PV penetration scenarios. The control strategy (2), which is voltage/Var control without SolarControl, showed a slight improvement in the inter-area oscillation frequency and damping factor as shown in Figure 6.14 and Figure 6.15.



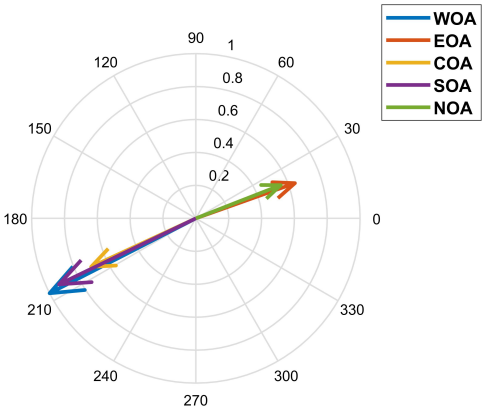
(a) 10% PV



(b) 30% PV

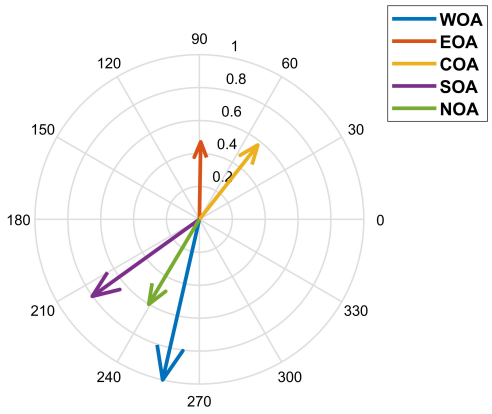


(c) 50% PV

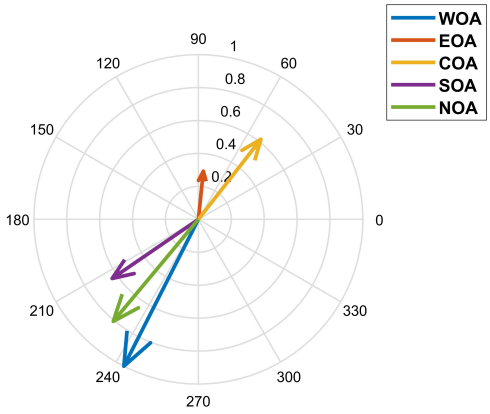


(d) 65% PV

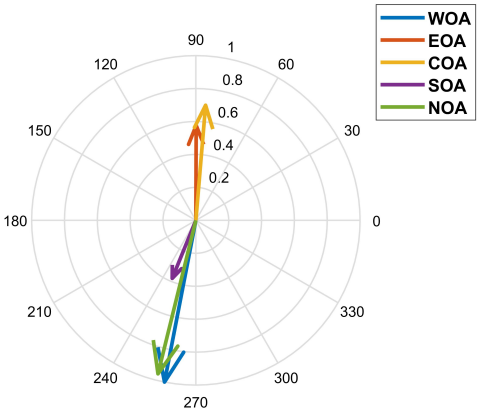
Figure 6.12: Mode shape of the inter-area mode (Mode1).



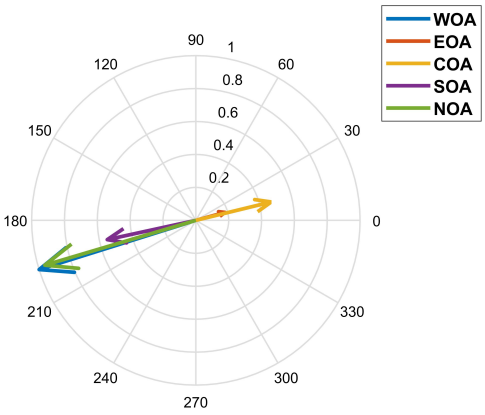
(a) 10% PV



(b) 30% PV



(c) 50% PV



(d) 65% PV

Figure 6.13: Mode shape of the inter-area mode (Mode2).

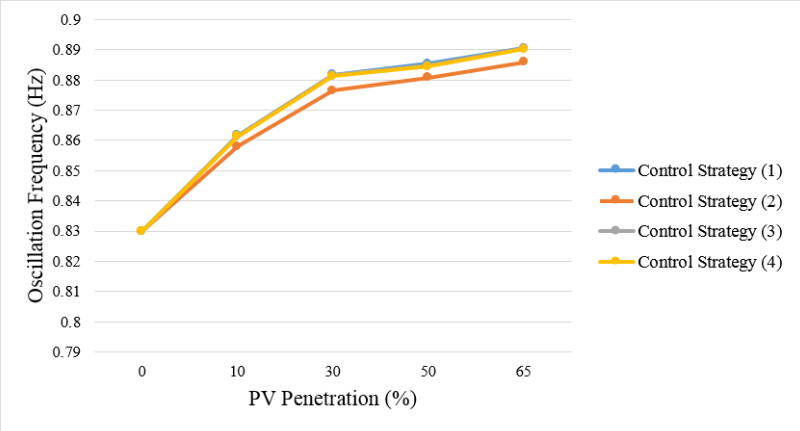


Figure 6.14: Inter-area oscillation frequency with four PV control strategies.

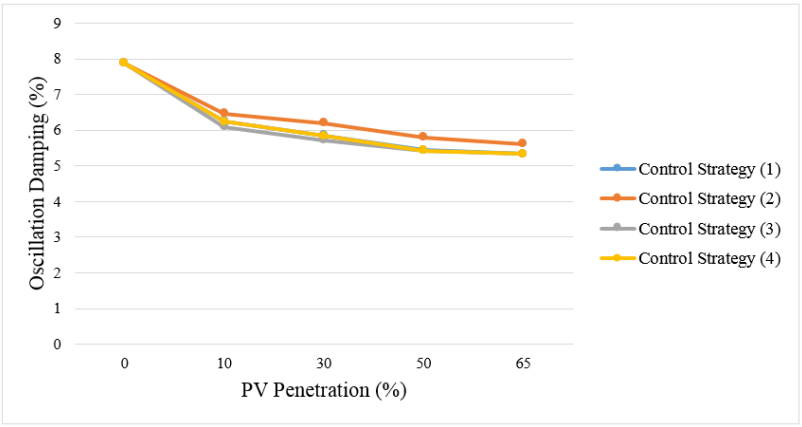


Figure 6.15: Inter-area oscillation damping ratio with four PV control strategies.

6.4 Summary

To estimate the impact of solar PV integration on the rotor angle stability, this study looks at the change of the CCT and the inter-area oscillations in the Saudi grid as more PV plants are being added. The results obtained indicate that high PV generation causes a few instability challenges. The study has shown that the increased solar energy has an adverse effect on the transient stability as it reduces the critical clearing time. In the context of small-signal stability, large-scaled solar power results in poor damping inter-area oscillations with higher frequency amplitudes. It has changed the mode shape of the inter-area modes.

Since higher PV penetration seems certain to happen in the foreseeable future, it is imperative for system operators to conduct a comprehensive analysis on the effect of integrating solar energy on power system oscillation stability. There are some corrective measures that can be considered to provide enough damping of inter-area oscillations such as keeping on major synchronous generators, incorporating advanced power system stabilizers and employing FACT devices. Also, system protection scheme needs to be modified to avoid the transient stability concerns regarding the change of the CCT due to higher solar energy integration.

Chapter 7

CONCLUSION

In general, this dissertation investigates the impact of high penetration of photovoltaic systems on the stability of the Saudi national power grid. Given the ambitious renewable energy target of the Saudi government, this work can be considered as the foundation for future research related to integrating large-scale solar farms into the Saudi grid. It can help system planners and operators to make excellent planning and operation actions regarding high solar penetration.

In the beginning, the Saudi power grid is discussed in detail, and an adaptive dynamic model resembling the real Saudi grid is developed using actual system data collected from public domains. The model is validated through comparing the obtained simulation results of confirmed generation trip cases with field measurement data taken by FNET/GridEye. It has been proven that the developed model is fully capable of representing the real Saudi power system behavior. Also, the dynamic model has shown to be stable and robust after applying various disturbances at different locations of the grid.

Since the higher penetration of renewable energy resources might increase the stress on the buses and overload the transmission lines, this research work has assessed the voltage stability condition of the Saudi power grid using static analysis techniques. The voltage levels of all load buses are determined through standard power flow. Then, VQ sensitivity and QV modal analysis are utilized to identify the weak buses and branches in the grid in terms of voltage stability. Five load buses are found to have lower voltage magnitudes and larger sensitivity factors, and their operating points might be relatively closer to the instability margin. Also, it is found that their adjacent branches contribute to voltage instability as they consume extra reactive power. The active and reactive power margins of these critical buses are estimated using PV and QV curves. Finally, corrective and preventive actions are proposed to reduce the grid tendency into voltage instability points and hence prevent cascading blackouts in the system.

In the matter of solar energy, the solar radiation in Saudi Arabia is analyzed from December 2015 to November 2017. The radiation information confirms the rich solar availability and indicates that there is adequate solar radiation all over the country throughout the year.

Dynamic analysis shows that the higher levels of solar PV penetration can cause an alteration in the frequency response after disturbances, which significantly reduce the system security. It has been found that the frequency response of the Saudi grid shows a noticeable degradation after major events as more solar PV units are being penetrated. At some PV penetration levels, the under-frequency load shedding relay is activated, mostly in the case of 50% solar generation and higher for some generator trip events in the highly loaded areas. It can be concluded that the grid is prone to frequency instability when having more

solar PV units in the system. This adverse impact on the frequency stability is due to the decrease in the overall system inertia. Therefore, keeping adequate frequency response after major disturbances with high PV penetration becomes a significant challenge. Simulation results show that the frequency instability can be improved by increasing the number of synchronous machines having active governors or reducing the governor droop control to 3%. These two practices are effectively able to reduce the frequency large deviation caused by under frequency events with higher solar penetration. Additionally, it has been proven that the energy storage system can effectively improve the frequency stability based on the available energy capacity.

The impacts of the higher PV penetration on the rotor angle stability and inter-area oscillations are investigated. It has been determined that the inter-area oscillations are highly affected with the increasing amount of solar generation. The oscillation frequency magnitude is increased whereas the oscillation damping is reduced as the number of penetrated solar panels is increased in the Saudi grid. The mode shape changes with different amounts of solar energy. Further study is performed to demonstrate the corresponding change in the critical clearing time (CCT) with higher solar integration in order to look at the impact on the transient stability. It has been found that the CCT in most of the cases tends to slightly decrease with the increase of PV penetration levels, which means the system security is reduced. This pinpoints the fact that the reduced system inertia resulted from displacing conventional generation units is one of the causes of deteriorated rotor angle stability. Consequently, keeping critical conventional machines online can help to alleviate the adverse impact on the rotor angle stability and inter-area oscillations resulted from the contribution of the solar PV units.

In future work, the dynamic model accuracy can be further improved by installing more synchro-phasor measurements at different regions in the country to capture more events and better match the current Saudi power grid. Since this study represents a specific snapshot of the grid operating condition, it is imperative to extend this model by incorporating different loading conditions. Further studies are recommended to compare the impact and the cost of the different reactive power support applications to improve the voltage stability.

Additional research needs to be conducted to address the economic analysis for installing such large-scale solar PV plants and explore the economic advantages of incorporating solar energy and associated energy storage facilities. Proposing mitigation practices to improve the rotor angle stability and the inter-area oscillations when more PV plants are installed could be an interesting research topic. Future work can also focus on designing more effective protection scheme based on the observed alteration of the CCT after more PV units are being added to the grid to improve power system security and reliability.

Since the Saudi government is planning to incorporate certain levels of wind energy in its energy portfolio in addition to the suggested solar PV plants, this work can be extended by studying the impact of penetration of large-scale solar and wind farms at different locations on the frequency stability and rotor angle stability.

Main Contribution

The major contributions of this dissertation are

- Developing an adaptive dynamic model resembling the actual behavior of the Saudi power grid, and validating its accuracy and stability.

- Investigating the voltage stability conditions of the Saudi power grid.
- Analyzing the solar radiation data in Saudi Arabia in the recent years.
- Studying the impact of high PV penetration on the frequency stability of the Saudi power system.
- Studying the impact of high PV penetration on the critical clearing time and the inter-area oscillations.

BIBLIOGRAPHY

[1] "Small-scale solar PV systems regulations," tech. rep., The Electricity & Co-Generation Regulatory Authority, July 2017. 1

[2] Saudi Press Agency (SPA), "HRH crown prince signs MoU with Softbank to establish the world's largest solar project." Available at https://www.spa.gov.sa/viewstory.php?lang=en&newsid=1745260, March 2018. 2

[3] "Saudi Electricity Company, annual report," tech. rep., Saudi Electricity Company, 2015. 8, 11, 12

[4] ECRA, "The Electricity & Co-Generation Regulatory Authority." Available at http://www.ecra.gov.sa/en-us/Pages/default.aspx, 2017. 8, 9, 10, 11, 13

[5] K.A.CARE, "King Abdullah city for atomic and renewable energy." Available at https://www.kacare.gov.sa/en/Pages/default.aspx, 2017. 8, 75

[6] B. H. A. Mutwali and M. E. El-Hawary, "An economic analysis of grid-tied residential photovoltaic systems: A case study of Saudi Arabia," in *2013 26th IEEE Canadian Conference on Electrical and Computer Engineering (CCECE)*, pp. 1–4, May 2013. 9

[7] "Saudi Electricity Company, annual report," tech. rep., Saudi Electricity Company, 2012. 9

[8] R. R. Obaid and A. H. Mufti, "Present state, challenges, and future of power generation in Saudi Arabia," in *2008 IEEE Energy 2030 Conference*, pp. 1–6, Nov 2008. 11, 12

[9] T. Alquthami and R. R. Obaid, "An adaptive dynamic model of the western power grid of Saudi Arabia," in *2011 IEEE PES Conference on Innovative Smart Grid Technologies - Middle East*, pp. 1–6, Dec 2011. 12

[10] T. M. Aljohani and A. M. Alzahrani, "The operation of the GCCIA HVDC project and its potential impacts on the electric power systems of the region," *International Journal of Electronics and Electrical Engineering*, vol. 2, no. 3, pp. 207–213, 2014. 12

[11] "Electricity, Arab fund embodiment of joint Arab action (AFESD)," in *Arab Fond for Economic and Social Development*, SAFAT, Kuwait, 2011. 12, 13

[12] I. C. Report, "Dynamic models for steam and hydro turbines in power system studies," *IEEE Transactions on Power Apparatus and Systems*, vol. PAS-92, pp. 1904–1915, Nov 1973. 17

[13] P. M. Anderson and A. A. Fouad, *Power system control and stability*. Wiley India Pvt. Limited, 2008. 17

[14] "IEEE recommended practice for excitation system models for power system stability studies," *IEEE Std 421.5-2005 (Revision of IEEE Std 421.5-1992)*, pp. 1–93, April 2006. 17

[15] L. Lima, "Report on the 14-generator system Australian reduced model," tech. rep., IEEE PES Task Force on Benchmark Systems for Stability Controls, 2013. 17

[16] *Siemens Power Technologies International, PSS®E 33.5 Model Library.*, 2013. 19, 20, 127

[17] G. Kou, *Dynamic Modeling and Renewable Integration Studies on the U.S. Power Grids*. PhD thesis, The University of Tennessee, Knoxville, August 2016. 21, 90, 91, 92, 95, 120, 150, 151

[18] G. Kou, P. Markham, S. Hadley, T. King, and Y. Liu, "Impact of governor deadband on frequency response of the U.S. Eastern Interconnection," *IEEE Transactions on Smart Grid*, vol. 7, pp. 1368–1377, May 2016. 37

[19] Y. Zhang, P. Markham, T. Xia, L. Chen, Y. Ye, Z. Wu, Z. Yuan, L. Wang, J. Bank, J. Burgett, R. W. Conners, and Y. Liu, "Wide-area frequency monitoring network (FNET) architecture and applications," *IEEE Transactions on Smart Grid*, vol. 1, pp. 159–167, Sept 2010. 38, 39

[20] Z. Zhong, C. Xu, B. J. Billian, L. Zhang, S. J. S. Tsai, R. W. Conners, V. A. Centeno, A. G. Phadke, and Y. Liu, "Power system frequency monitoring network (FNET) implementation," *IEEE Transactions on Power Systems*, vol. 20, pp. 1914–1921, Nov 2005. 38

[21] Y. Ye, *Wide-area Situational Awareness Application Developments*. PhD thesis, The University of Tennessee, Knoxville, December 2011. 38, 42

[22] R. M. Gardner, J. K. Wang, and Y. Liu, "Power system event location analysis using wide-area measurements," in *2006 IEEE Power Engineering Society General Meeting*, pp. 7 pp.–, 2006. 38

[23] D. Zhou, Y. Liu, and J. Dong, "Frequency-based real-time line trip detection and alarm trigger development," in *2014 IEEE PES General Meeting — Conference Exposition*, pp. 1–5, July 2014. 39

[24] D. Kosterev and D. Davies, "System model validation studies in WECC," in *IEEE PES General Meeting*, pp. 1–4, July 2010. 40

[25] J. W. Ingleson and E. Allen, "Tracking the Eastern Interconnection frequency governing characteristic," in *IEEE PES General Meeting*, pp. 1–6, July 2010. 42, 44

[26] L. Chen, P. N. Markham, and Y. Liu, "Wide-area dynamic model validation using FNET measurements," in *2012 IEEE PES Innovative Smart Grid Technologies (ISGT)*, pp. 1–7, Jan 2012. 42

[27] P. Kundur, *Power system stability and control*, vol. 7. McGraw-Hill New York, 1994. 50, 51, 53, 54, 55, 56, 57, 58, 59, 60, 138, 148

[28] V. Ajjarapu, *Computational techniques for voltage stability assessment and control*, vol. 7. Springer Science and Business Media, 2007. 50, 51, 60

[29] M. J. Khami, B. T. Atiyah, and K. M. Hashem, "Computer aided voltage stability analysis in power systems," *Journal of Thi-Qar University*, vol. 5, pp. 71–82, 2010. 51

[30] D. Das, *Electrical power systems*. New Age International (P) Limited, 2007. 51

[31] T. V. Cutsem and C. Vournas, *Voltage stability of electric power systems*, vol. 441. Springer Science and Business Media, 1998. 51, 52, 55, 56, 69

[32] K. Morison, H. Hamadani, and L. Wang, "Load modeling for voltage stability studies," in *2006 IEEE PES Power Systems Conference and Exposition*, pp. 564–568, Oct 2006. 51

[33] J. L. Corwin and W. T. Miles, *Impact assessment of the 1977 New York City blackout. Final report.* Jul 1978. 51

[34] A. Kurita and T. Sakurai, "The power system failure on July 23, 1987 in Tokyo," in *Proceedings of the 27th IEEE Conference on Decision and Control*, pp. 2093–2097 vol.3, Dec 1988. 51

[35] "Final report on the August 14, 2003 blackout in the United States and Canada: Causes and recommendations," tech. rep., U.S.-Canada Power System Outage Task Force, 2004. 51

[36] "Major interruptions (blackouts) study," tech. rep., Arab Union of Producers, Transporters, and Distributors of Electricity , Committee of Interconnected Arab Networks (CIAN), 2006. 52

[37] A. Kargarian, M. Raoofat, and M. Mohammadi, "Reactive power market management considering voltage control area reserve and system security," *Applied Energy*, vol. 88, no. 11, pp. 3832 – 3840, 2011. 53

[38] S. B. Halbhavi, S. Karki, and S. G. Kulkarni, "Reactive power pricing framework problems & a proposal for a competitive market," *International Journal of Innovations in Engineering and Technology (IJIET)*, vol. 1, no. 2, pp. 22 – 27, 2012. 53, 54

[39] A. Tiranuchit and R. J. Thomas, "A posturing strategy against voltage instabilities in electric power systems," *IEEE Transactions on Power Systems*, vol. 3, pp. 87–93, Feb 1988. 55

[40] "Load modeling for power flow and transient stability computer studies," LoadModeling Reference Manual, Final Report EL-5003CCMV2 Final Report EL-5003CCMV2, EPRI, 1987. 55

[41] "Assessment of voltage stability methods and tools," EPRI project rp3578-01 final report tr-105214, EPRI, 1995. 56

[42] K. Ellithy, A. Gastli, A. Alhinai, and Z. Alabri, "Voltage stability analysis of Muscat power system during summer weather conditions," *Sultan Qaboos University Journal for Science*, vol. 5, pp. 35–45, 2000. 60

[43] Y. Mansour and C. Canizares, *Power system stability and control*, vol. 5, ch. Voltage Stability. CRC Press, third ed., 2012. 61

[44] "The Saudi Arabian distribution code," tech. rep., Saudi Electricity Company, November 2008. 62, 71, 92

[45] H. Saadat, *Power system analysis*. McGraw-Hill, third ed., 2009. 69

[46] F. R. Pazheri, M. F. Othman, N. H. Malik, and A. A. Al-Arainy, "Environmental friendly power dispatch in Saudi Arabia with renewable energy and energy storage," in *2012 4th International Conference on Intelligent and Advanced Systems (ICIAS2012)*, vol. 1, pp. 455–460, June 2012. 73, 80

[47] F. R. Pazheri, "Solar power potential in Saudi Arabia," *Journal of Engineering Research and Applications*, vol. 4, pp. 171–174, Sept 2014. 73, 74, 76, 77, 78, 79

[48] A. Hepbasli and Z. Alsuhaibani, "A key review on present status and future directions of solar energy studies and applications in Saudi Arabia," *Renewable and Sustainable Energy Reviews*, vol. 15, no. 9, pp. 5021 – 5050, 2011. 73, 76, 77, 78, 80

[49] S. Rehman, M. Bader, and S. A. Al-Moallem, "Cost of solar energy generated using PV panels," vol. 11, pp. 1843–1857, 10 2007. 73, 77, 80

[50] A. K. Gumgumji and O. A. Mohammed, "Increasing renewable penetration in the Saudi Arabia electricity system," in *2013 Proceedings of IEEE Southeastcon*, pp. 1–5, April 2013. 74, 75, 76, 77

[51] Z. Aljarboua, "The national energy strategy for Saudi Arabia," *Engineering and Technology*, vol. 3, no. 9, pp. 1774–1783, 2009. 74

[52] F. R. Pazheri, N. H. Malik, A. A. Al-Arainy, E. A. Al-Ammar, A. Imthias, and S. O. K, "Smart grid can make Saudi Arabia megawatt exporter," in *2011 Asia-Pacific Power and Energy Engineering Conference*, pp. 1–4, March 2011. 74, 76, 78

[53] "Saudi Arabia vision 2030." Available at http://vision2030.gov.sa/en, 2016. 75

[54] A. Jamal and K. S. Jerath, "An analysis of present and future of solar energy in Kingdom of Saudi Arabia along with a comparative study between Saudi Aramco Solar Car Park and other similar projects in Gulf," *International Journal of Advance Engineering and Research Development*, vol. 3, pp. 15–25, March 2016. 75, 79

[55] A. Almasoud and H. M. Gandayh, "Future of solar energy in Saudi Arabia," *Journal of King Saud University - Engineering Sciences*, vol. 27, no. 2, pp. 153 – 157, 2015. 75, 78, 79, 80, 81

[56] International Energy Agency, "US energy information administration, 2014. Saudi Arabia energy profile." Available at https://www.iea.org/statistics/statisticssearch/report/?country=SAUDIARABI&product=coal&year=2014, 2014. 75

[57] R. H. Sagor and M. A. Abido, "Study of solar energy for PV implementation in Saudi Arabia," in *2010 IEEE International Energy Conference*, pp. 830–834, Dec 2010. 76

[58] A. AlDowsari, R. Bkayrat, H. AlZain, and T. Shahin, "Best practices for mitigating soiling risk on PV power plants," in *2014 Saudi Arabia Smart Grid Conference (SASG)*, pp. 1–6, Dec 2014. 76

[59] H. Albalawi, E. Makram, and T. Alogla, "PV penetration with battery storage for an isolated northwest grid of Saudi Arabia," in *2015 North American Power Symposium (NAPS)*, pp. 1–6, Oct 2015. 76, 77, 80, 81

[60] R. A. Shalwala and J. A. M. Bleijs, "Impact of grid-connected PV systems in residential areas in Saudi Arabia," in *2009 44th International Universities Power Engineering Conference (UPEC)*, pp. 1–5, Sept 2009. 77

[61] A. Alshehri, B. Parrott, A. Outa, A. Amer, F. Abdellatif, H. Trigui, P. Carrasco, S. Patel, and I. Taie, "Dust mitigation in the desert: Cleaning mechanisms for solar

panels in arid regions," in *2014 Saudi Arabia Smart Grid Conference (SASG)*, pp. 1–6, Dec 2014. 77

[62] S. Rehman and I. El-Amin, "Performance evaluation of an off-grid photovoltaic system in Saudi Arabia," *Energy and Exergy Modelling of Advance Energy Systems*, vol. 46, no. 1, pp. 451 – 458, 2012. 77, 81

[63] N. Al-Abbadi, S. Alawaji, M. B. Mahfoodh, D. Myers, S. Wilcox, and M. Anderberg, "Saudi Arabian solar radiation network operation data collection and quality assessment," *Renewable Energy*, vol. 25, no. 2, pp. 219 – 234, 2002. 78

[64] M. Yamada, "Vision 2030 and the birth of Saudi solar energy," *Middle East Institute*, vol. 7, pp. 1–9, July 2016. 79, 80

[65] S. Rehman, "Solar radiation over Saudi Arabia and comparisons with empirical models," *Energy*, vol. 23, no. 12, pp. 1077 – 1082, 1998. 80

[66] A. Almarshoud, "Performance of solar resources in Saudi Arabia," *Renewable and Sustainable Energy Reviews*, vol. 66, pp. 694 – 701, 2016. 80

[67] S. Alyahya and M. A. Irfan, "Role of Saudi universities in achieving the solar potential 2030 target," *Energy Policy*, vol. 91, pp. 325 – 328, 2016. 81

[68] K.A.CARE, "King Abdullah City for Atomic and Renewable Energy - Renewable Resource Atlas." Available at https://rratlas.kacare.gov.sa/RRMMDataPortal/en/MapTool, 2017. 82, 83

[69] E. Zell, S. Gasim, S. Wilcox, S. Katamoura, T. Stoffel, H. Shibli, J. Engel-Cox, and M. A. Subie, "Assessment of solar radiation resources in Saudi Arabia," *Solar Energy*, vol. 119, pp. 422 – 438, 2015. 82, 84, 85

[70] F. Vignola, J. Michalsky, and T. Stoffel, *Solar and Infrared Radiation Measurements*. CRC Press, Boca Raton, FL, 2012. 86

[71] B. Tamimi, C. Canizares, and K. Bhattacharya, "System stability impact of large-scale and distributed solar photovoltaic generation: The case of Ontario, Canada," *IEEE Transactions on Sustainable Energy*, vol. 4, pp. 680–688, July 2013. 89

[72] K. Clark, N. E. Miller, and R. Walling, "Modeling of GE solar photovoltaic plants for grid studies," tech. rep., General Electric International, Inc, Schenectary, NY, 2010. 90, 91

[73] A. Jimenez, "PSSE PV inverter and power plant controller models based on GEPV models," tech. rep., Power Electronics, 2015. 90, 91

[74] "The Saudi Arabian grid code," tech. rep., National Grid Saudi Arabia, October 2016. 92

[75] "Rate of change of frequency distribution code modifications," tech. rep., Northern Ireland Electricity Networks, April 2016. 103

[76] F. Teng and G. Strbac, "Assessment of the role and value of frequency response support from wind plants," *IEEE Transactions on Sustainable Energy*, vol. 7, pp. 586–595, April 2016. 103

[77] C. Seneviratne and C. Ozansoy, "Frequency response due to a large generator loss with the increasing penetration of wind/PV generation a literature review," *Renewable and Sustainable Energy Reviews*, vol. 57, no. Supplement C, pp. 659 – 668, 2016. 103

[78] N. Miller, M. Shao, S. Pajic, and R. DAquila, "Eastern frequency response study," tech. rep., GE Energy, Schenectady, New York, May 2013. 103

[79] J. Undrill, "Power and frequency control as it relates to wind-powered generation," Tech. Rep. LBNL-4143E, Ernest Orlando Lawrence Berkeley National Laboratory, 2010. 117

[80] N. W. Miller, M. Shao, R. D'aquila, S. Pajic, and K. Clark, "Frequency response of the US Eastern Interconnection under conditions of high wind and solar generation," in *2015 Seventh Annual IEEE Green Technologies Conference*, pp. 21–28, April 2015. 118

[81] J.-W. Shim, *The Impact of Large-Scale Renewable Energy on Grid Small-Signal and Frequency Stability: Modelling, Analysis, and Control*. PhD thesis, The University of Sydney and Yonsei University, Seoul, South Korea, July 2016. 120, 126, 149

[82] "Governor droop setting," Tech. Rep. PRC-001-WECC-CRT-1.2, Western Electricity Coordinating Council, 2016. 122

[83] A. Oudalov, D. Chartouni, and C. Ohler, "Optimizing a battery energy storage system for primary frequency control," *IEEE Transactions on Power Systems*, vol. 22, pp. 1259–1266, Aug 2007. 126

[84] X. Xu, M. Bishop, D. G. Oikarinen, and C. Hao, "Application and modeling of battery energy storage in power systems," *CSEE Journal of Power and Energy Systems*, vol. 2, pp. 82–90, Sept 2016. 126

[85] "WECC battery storage dynamic modeling guideline," tech. rep., Western Electricity Coordinating Council, Modeling and Validation Work Group, November 2016. 126

[86] I. Serban and C. Marinescu, "Control strategy of three-phase battery energy storage systems for frequency support in microgrids and with uninterrupted supply of local loads," *IEEE Transactions on Power Electronics*, vol. 29, pp. 5010–5020, Sept 2014. 126

[87] M. A. Torres, L. A. C. Lopes, L. A. Morn, and J. R. Espinoza, "Self-tuning virtual synchronous machine: A control strategy for energy storage systems to support dynamic frequency control," *IEEE Transactions on Energy Conversion*, vol. 29, pp. 833–840, Dec 2014. 126

[88] J. Schmutz, "Primary frequency control provided by battery," Master's thesis, ETH Zurich, June 2013. 126

[89] X. Wang and M. Yue, "Design of energy storage system to improve inertial response for large scale PV generation," in *2016 IEEE Power and Energy Society General Meeting (PESGM)*, pp. 1–5, July 2016. 127

[90] M. C. Such, "Operation and control strategies for battery energy storage systems to increase penetration levels of renewable generation on remote microgrids," Master's thesis, The University of Texas at Austin, May 2013. 127

[91] D.-H. Son and S.-R. Nam, "Development of PSS/E dynamic model for controlling battery output to improve frequency stability in power systems," vol. 11, no. 4, p. 1193, 2017. 127

[92] P. Kundur, J. Paserba, V. Ajjarapu, G. Andersson, A. Bose, C. Canizares, N. Hatziargyriou, D. Hill, A. Stankovic, C. Taylor, T. V. Cutsem, and V. Vittal, "Definition and classification of power system stability IEEE/CIGRE joint task force on stability terms and definitions," *IEEE Transactions on Power Systems*, vol. 19, pp. 1387–1401, Aug 2004. 137

[93] S. Savulescu, *Real-Time Stability Assessment in Modern Power System Control Centers*. IEEE Press Series on Power Engineering, Wiley, 2009. 138

[94] L. G. W. Roberts, A. R. Champneys, K. R. W. Bell, and M. di Bernardo, "Analytical approximations of critical clearing time for parametric analysis of power system transient stability," *IEEE Journal on Emerging and Selected Topics in Circuits and Systems*, vol. 5, pp. 465–476, Sept 2015. 138, 140

[95] Y. J. Lin, "Comparison of speed and voltage based critical clearing time of squirrel cage induction generator," in *2010 IEEE 11th International Conference on Probabilistic Methods Applied to Power Systems*, pp. 283–286, June 2010. 139

[96] C. Liu, Z. Chen, C. L. Bak, Z. Liu, P. Lund, and P. Ronne-Hansen, "Transient stability assessment of power system with large amount of wind power penetration: The Danish case study," in *2012 10th International Power Energy Conference (IPEC)*, pp. 461–467, Dec 2012. 139

[97] M. Chowdhury, N. Hosseinzadeh, W. Shen, and H. Pota, "Comparative study on fault responses of synchronous generators and wind turbine generators using transient stability index based on transient energy function," *International Journal of Electrical Power & Energy Systems*, vol. 51, pp. 145 – 152, 2013. 139

[98] A. Mitra and D. Chatterjee, "A sensitivity based approach to assess the impacts of integration of variable speed wind farms on the transient stability of power systems," *Renewable Energy*, vol. 60, pp. 662 – 671, 2013. 139

[99] E. J. Medina-Dominguez and J. F. Medina-Padron, "Critical clearing time and wind power in small isolated power systems considering inertia emulation," *Energies*, vol. 8, no. 11, pp. 12669–12684, 2015. 139, 140

[100] L. Shi, S. Sun, L. Yao, Y. Ni, and M. Bazargan, "Effects of wind generation intermittency and volatility on power system transient stability," *IET Renewable Power Generation*, vol. 8, pp. 509–521, July 2014. 139

[101] N. Amutha and B. K. Kumar, "Effect of modeling of induction generator based wind generating systems on determining CCT," *IEEE Transactions on Power Systems*, vol. 28, pp. 4456–4464, Nov 2013. 139

[102] Y. Chen and Z. Liu, "Effect of large-scale wind farm on transient stability," in *2010 International Conference on Electrical and Control Engineering*, pp. 3680–3683, June 2010. 139

[103] H. Hou, L. Lin, T. Wu, and Y. Miao, "Comparison of transient stability between wind farm based on DFIG and traditional power plant in an actual grid," in *2010 Asia-Pacific Power and Energy Engineering Conference*, pp. 1–4, March 2010. 139

[104] Y.-K. Wu, T.-C. Lee, T.-Y. Hsieh, and W.-M. Lin, "Impact on critical clearing time after integrating large-scale wind power into Taiwan power system," *Sustainable Energy Technologies and Assessments*, vol. 16, pp. 128 – 136, 2016. 139

[105] A. Hoballah, "Power system dynamic behavior with large scale solar energy integration," in *2015 4th International Conference on Electric Power and Energy Conversion Systems (EPECS)*, pp. 1–6, Nov 2015. 139

[106] S. Anup, A. Verma, and T. S. Bhatti, "Transient stability study in solar photovoltaic-wind plant based multimachine system," in *2017 IEEE International Conference on Smart Grid and Smart Cities (ICSGSC)*, pp. 178–182, July 2017. 140

[107] A. Paul and N. Senroy, "Critical clearing time estimation using synchrophasor data-based equivalent dynamic model," *IET Generation, Transmission Distribution*, vol. 9, no. 7, pp. 609–614, 2015. 140

[108] I. B. Sulistiawati, A. Priyadi, O. A. Qudsi, A. Soeprijanto, and N. Yorino, "Critical clearing time prediction within various loads for transient stability assessment by means of the extreme learning machine method," *International Journal of Electrical Power & Energy Systems*, vol. 77, pp. 345 – 352, 2016. 140

[109] W. Phootrakornchai and S. Jiriwibhakorn, "Online critical clearing time estimation using an adaptive neuro-fuzzy inference system (ANFIS)," *International Journal of Electrical Power & Energy Systems*, vol. 73, pp. 170 – 181, 2015. 140

[110] M. Pavella, D. Ernst, and D. Ruiz-Vega, *Transient Stability of Power Systems: A Unified Approach to Assessment and Control*. Power Electronics and Power Systems, Springer US, 2012. 140, 141

[111] L. Shi, S. Dai, Y. Ni, L. Yao, and M. Bazargan, "Transient stability of power systems with high penetration of DFIG based wind farms," in *2009 IEEE Power Energy Society General Meeting*, pp. 1–6, July 2009. 140, 141

[112] S. Gurung, S. Naetiladdanon, and A. Sangswang, "Impact of large photovoltaic penetration on small signal stability," in *2016 IEEE Region 10 Conference (TENCON)*, pp. 646–650, Nov 2016. 148

[113] D. J. Vowles, C. Samarasinghe, M. J. Gibbard, and G. Ancell, "Effect of wind generation on small-signal stability - a New Zealand example," in *2008 IEEE Power and Energy Society General Meeting - Conversion and Delivery of Electrical Energy in the 21st Century*, pp. 1–8, July 2008. 148

[114] M. Edrah, K. L. Lo, and O. Anaya-Lara, "Impacts of high penetration of DFIG wind turbines on rotor angle stability of power systems," *IEEE Transactions on Sustainable Energy*, vol. 6, pp. 759–766, July 2015. 148

[115] J. Quintero, V. Vittal, G. T. Heydt, and H. Zhang, "The impact of increased penetration of converter control-based generators on power system modes of

oscillation," *IEEE Transactions on Power Systems*, vol. 29, pp. 2248–2256, Sept 2014. 149

[116] L. G. Meegahapola, T. Littler, and D. Flynn, "Decoupled-DFIG fault ride-through strategy for enhanced stability performance during grid faults," *IEEE Transactions on Sustainable Energy*, vol. 1, pp. 152–162, Oct 2010. 149

[117] S. Eftekharnejad, V. Vittal, G. T. Heydt, B. Keel, and J. Loehr, "Small signal stability assessment of power systems with increased penetration of photovoltaic generation: A case study," *IEEE Transactions on Sustainable Energy*, vol. 4, pp. 960–967, Oct 2013. 149, 150

[118] J. Slootweg and W. Kling, "The impact of large scale wind power generation on power system oscillations," *Electric Power Systems Research*, vol. 67, no. 1, pp. 9 – 20, 2003. 149

[119] R. Krishan, A. Verma, and B. Prasad, "Small signal stability analysis of grid connected distributed PV and wind energy system," in *2014 6th IEEE Power India International Conference (PIICON)*, pp. 1–6, Dec 2014. 149

[120] R. Shah, N. Mithulananthan, A. Sode-Yome, and K. Y. Lee, "Impact of large-scale PV penetration on power system oscillatory stability," in *IEEE PES General Meeting*, pp. 1–7, July 2010. 149

[121] A. U. Krismanto, M. Nadarajah, and O. Krause, "Influence of renewable energy based microgrid on low frequency oscillation of power systems," in *2015 IEEE PES Asia-Pacific Power and Energy Engineering Conference (APPEEC)*, pp. 1–5, Nov 2015.

149

[122] R. Elliott, R. Byrne, A. Ellis, and L. Grant, "Impact of increased photovoltaic generation on inter-area oscillations in the Western North American power system," in *2014 IEEE PES General Meeting — Conference Exposition*, pp. 1–5, July 2014. 149

[123] G. Tsourakis, B. M. Nomikos, and C. D. Vournas, "Contribution of doubly fed wind generators to oscillation damping," *IEEE Transactions on Energy Conversion*, vol. 24, pp. 783–791, Sept 2009. 149

[124] W. Du, H. F. Wang, and R. Dunn, "Power system small-signal oscillation stability as affected by large-scale PV penetration," in *2009 International Conference on Sustainable Power Generation and Supply*, pp. 1–6, April 2009. 149

[125] D. Gautam, V. Vittal, and T. Harbour, "Impact of increased penetration of DFIG-based wind turbine generators on transient and small signal stability of power systems," *IEEE Transactions on Power Systems*, vol. 24, pp. 1426–1434, Aug 2009. 149

[126] H. Liu, L. Jin, D. Le, and A. A. Chowdhury, "Impact of high penetration of solar photovoltaic generation on power system small signal stability," in *2010 International Conference on Power System Technology*, pp. 1–7, Oct 2010. 149

[127] R. Shah, N. Mithulananthan, and R. Bansal, "Oscillatory stability analysis with high penetrations of large-scale photovoltaic generation," *Energy Conversion and Management*, vol. 65, pp. 420 – 429, 2013. 150

[128] B. Mehta, P. Bhatt, and V. Pandya, "Small signal stability analysis of power systems with DFIG based wind power penetration," *International Journal of Electrical Power & Energy Systems*, vol. 58, pp. 64 – 74, 2014. 150

[129] M. L. Crow and A. Singh, "The matrix pencil for power system modal extraction," *IEEE Transactions on Power Systems*, vol. 20, pp. 501–502, Feb 2005. 150, 151

[130] T. K. Sarkar and O. Pereira, "Using the matrix pencil method to estimate the parameters of a sum of complex exponentials," *IEEE Antennas and Propagation Magazine*, vol. 37, pp. 48–55, Feb 1995. 150

[131] L. L. Grant and M. L. Crow, "Comparison of matrix pencil and prony methods for power system modal analysis of noisy signals," in *2011 North American Power Symposium*, pp. 1–7, Aug 2011. 151

APPENDICES

A Meteorological Stations Information

Table A.1: Stations elevation and instruments types.

Number	Station	Station elevation (m)	Instrument type
1	Abha	2,173	Tier 1B
2	Afif	1,060	Tier 2
3	Al Aflaaj	567	Tier 2
4	Al Baha	1,680	Tier 1C
5	Al Dawadmi	955	Tier 2
6	Al Hanakiyah	873	Tier 2
7	Al Jouf	680	Tier 1C
8	Al Qunfudhah	20	Tier 2
9	Al-Uyaynah	779	Tier 1A
10	Al Wajh	21	Tier 1C
11	Arar	570	Tier 1C
12	Duba	45	Tier 2
13	Hafar Al Batin	383	Tier 2
14	Hail	950	Tier 1C
15	Dammam (IAFU)	28	Tier 1B
16	Jazan	1	Tier 2
17	K.A.CARE HQ	668	Tier 2
18	K.A. CARE	895	Tier 2
19	Osfan	119	Tier 2
20	Hada Al Sham	245	Tier 2
21	Jeddah (KAU)	75	Tier 2
22	Thuwal	34	Tier 2
23	Al Dhahran	75	Tier 2
24	Al Ahsa	170	Tier 1C
25	Riyadh (KSU)	688	Tier 2

Continued on the next page

Table A.1 – *Continued from the previous page*

Number	**Station**	**Station elevation (m)**	**Instrument type**
26	Majmaah	718	Tier 2
27	Najran	1,187	Tier 2
28	Al Kharj	465	Tier 2
29	Riyadh (PNU)	633	Tier 2
30	Qassim	688	Tier 1B
31	Rania	933	Tier 1C
32	Yanbu	17	Tier 1C
33	Al Khafji	5	Tier 1C
34	Farasan	16	Tier 2
35	Hagl	36	Tier 2
36	Al Jubail	89	Tier 2
37	Umluj	10	Tier 2
38	Shaqra	804	Tier 2
39	Sharurah	760	Tier 2
40	Tabuk	781	Tier 1C
41	Madinah	643	Tier 1C
42	Taif	1,518	Tier 1C
43	Timaa	844	Tier 2
44	Al Farshah	1,094	Tier 2
45	Makkah	295	Tier 1C
46	Wadi Addawasir	671	Tier 1C

Table A.2: Irradiance information in Saudi Arabia.

Location	**Average monthly DHI** (Wh/m^2)	**Average monthly DNI** (Wh/m^2)	**Average monthly GHI** (Wh/m^2)	**Average monthly temperature** (C^0)
Hanakiyah	2,208.72	6,025.15	6,239.28	28.22
Osfan	2,446.08	5,046.01	5,952.15	30.05
Hada Al Sham	2,449.87	5,009.03	5,957.77	30.77
Jeddah (KAU)	2,486.42	4,834.21	5,858.43	30.98
Thuwal	2,363.15	5,171.62	5,946.09	28.44
Rania	2,430.44	5,583.83	6,272.68	28.05
Yanbu	2,204.60	5,901.58	6,195.55	28.31
Taif	2,118.81	6,314.76	6,386.22	23.88
Hafar Al Batin	2,337.59	5,445.71	5,920.34	27.00
Dammam(IAFU)	2,261.68	5,329.39	5,852.08	27.23
Dhahran	2,168.54	5,025.91	5,537.15	27.96
Ahsa	2,457.19	5,264.13	6,015.76	28.63
Jubail	2,220.60	5,187.09	5,712.28	26.69
Afif	2,397.52	5,904.78	6,372.29	26.11
Dawadmi	2,418.16	5,763.63	6,297.46	26.13
Aflaaj	2,610.48	5,575.61	6,422.11	28.99
Uyaynah	2,343.12	5,636.46	6,148.40	25.96
K.A.CARE HQ	2,403.96	5,281.23	6,002.48	28.75
K.A. CARE	2,436.30	5,840.51	6,374.22	26.37
Riyadh (KSU)	2,457.48	5,407.48	6,150.21	28.07
Majmaah	2,443.48	5,410.57	6,084.44	25.90
Kharj	2,518.80	5,139.35	6,012.19	27.69

Continued on the next page

Table A.2 – *Continued from the previous page*

Location	**Average monthly DHI** (Wh/m^2)	**Average monthly DNI** (Wh/m^2)	**Average monthly GHI** (Wh/m^2)	**Average monthly temperature** (C^0)
Qassim	2,344.15	5,625.99	6,104.16	26.88
Shaqra	2,456.54	5,583.88	6,219.28	26.94
Wadi Adwasir	2,504.54	5,676.59	6,408.14	27.70
Baha	2,148.42	6,008.44	6,244.00	23.84
Qunfudhah	2,704.23	4,253.20	5,763.63	30.22
Jazan	2,775.55	3,934.39	5,661.45	30.30
Najran	2,468.08	6,123.54	6,696.31	26.66
Farasan	2,767.82	3,990.66	5,693.66	30.82
Sharurah	2,426.96	6,203.25	6,687.21	29.20
Farshah	2,334.59	5,113.26	5,940.89	28.05
Jouf	1,936.51	6,580.42	6,177.30	23.55
Wajh	1,803.14	6,698.40	6,189.97	26.18
Arar	1,932.26	6,426.99	6,043.15	23.11
Duba	1,661.87	6,925.12	6,140.03	27.64
Hagl	1,596.80	6,782.62	5,963.48	25.58
Tabuk	1,669.49	7,135.80	6,262.52	23.13
Umluj	1,944.08	6,234.65	6,094.67	27.68
Timaa	1,884.19	6,989.42	6,413.08	24.79

Table A.3: Average monthly DHI/GHI ratio for all stations.

Location	DHI/GHI
Hanakiyah	0.354002134
Osfan	0.410956545
Hada Al Sham	0.411205499
Jeddah (KAU)	0.424416955
Thuwal	0.397429402
Rania	0.38746428
Yanbu	0.355835371
Taif	0.331778332
Hafar Al Batin	0.394840243
Dammam (IAFU)	0.386473753
Dhahran	0.391634692
Ahsa	0.408458889
Jubail	0.388741221
Afif	0.376241133
Dawadmi	0.383989573
Aflaaj	0.406483852
Uyaynah	0.381093468
K.A.CARE HQ	0.400494934
K.A. CARE	0.382210767
Riyadh (KSU)	0.399575624
Majmaah	0.401593956
Kharj	0.41894901
Qassim	0.38402578
Shaqra	0.39498843
Wadi Addawasir	0.390837437
Baha	0.344076751

Continued on the next page

Table A.3 – *Continued from the previous page*

Location	**DHI/GHI**
Qunfudhah	0.469187889
Jazan	0.490253903
Najran	0.368572255
Farasan	0.48612345
Sharurah	0.362925486
Farshah	0.392970186
Jouf	0.31348871
Wajh	0.291300707
Arar	0.319743566
Duba	0.270660854
Hagl	0.267762969
Tabuk	0.266584609
Umluj	0.318979709
Timaa	0.293803873

B GE PV Model Control Strategies and Dynamic Parameters

Table B.1: GE PV model control strategies.

Control strategy	**Configuration**
Volt/Var control with SolarConrol	VARFLG=1, PFAFLG=0, KQi=0.1
Volt/Var control without SolarConrol	VARFLG=0, PFAFLG=0, KQi=0.001
Fast power factor control with SolarConrol	VARFLG=1, PFAFLG=0, KQi=0.5
Fast power factor control without SolarConrol	VARFLG=0, PFAFLG=1, KQi=0.5

Table B.2: Dynamic model data for control model (GEPVE).

Description	**Value**
Tfv V-regulator filter	0.15
Kpv V-regulator proportional gain	18
Kiv V-regulator integrator gain	5
Rc line drop compensation resistance	0
Xc line drop compensation reactance	0
QMX V-regulator max limit	1
QMN V-regulator min limit	-1
IPMAX Max active current limit	1.12
TRV V-sensor	0.02

Continued on the next page

Table B.2 – *Continued from the previous page*

Description	**Value**
KQi MVAR/Volt gain	0.1
VMINCL	0.88
VMAXCL	1.15
KVi Volt/MVAr gain	120
XlQmin min. limit for Eqcmd	0.55
XlQmax max. limit for Eqcmd	1.55
Tv Lag time constant in WindVar controller	0.05
Tp Pelec filter in fast PF controller	0.05
Fn - A portion of on-line PV converters	1
ImaxTD - Converter current limit	1.12
Iphl - Hard active current limit	1.12
Iqhl - Hard reactive current limit	1.12
TIpqd - Reactive droop time constant	5
Kqd - Reactive droop gain	0
Xqd - Reactive droop Synthesizing Impedance	0
Vermx - Reactive power control maximum error signal	0.01
Vermn - Reactive power control minimum error signal	-0.01
Vfrz - Reactive power control freeze voltage	0.7

Table B.3: Dynamic model data for inverter model (GEPVG).

Description	**Value**
PRATE, rated power, MVA	600
Xeq-equivalent reactance for current injection	9,9999
VHVRCR2- HVRCR voltage 2	1.2
CURHVRCR2- Max. reactive current at VHVRCR2	2
Rlp_LVPL-Rate of active current change	5
T_LVPL-Voltage sensor for LVPL	0.02
LVPL voltage 1	0
LVPL power 1	0
LVPL voltage 2	0.5
LVPL power 2	0.167
LVPL voltage 3	0.90
LVPL power 3	0.98
XLVPL	0

C Lists of the Displaced Conventional Generators for PV Plants

Table C.1: List of the displaced conventional generators for 10% PV penetration level.

Bus number	Bus name	Operating region	Pgen (MW)	Qgen (Mvar)
104	RABIGH (R2)	WESTERN	480.0	88.740
110	YANBU (Y1)	WESTERN	661.6	100.89
206	JUBAIL	EASTERN	459.0	49.990
308	CENTR-SLACK (C1)	CENTRAL	680.3	137.37
310	UNAYZAH	CENTRAL	859.8	146.66
406	BISHAH	SOUTHERN	365.4	29.159
413	SHAQIQ	SOUTHERN	1,020	115.80
501	TABUK-1 (B1)	NORTHERN	641.9	98.284
501	TABUK-1 (B2)	NORTHERN	641.9	98.284
504	WAJH	NORTHERN	290.6	-17.25

Table C.2: List of the displaced conventional generators for 30% PV penetration level [a].

Bus number	Bus name	Operating region	Pgen (MW)	Qgen (Mvar)
104	RABIGH (R1)	WESTERN	1,575.6	291.29
104	RABIGH (R3)	WESTERN	1,288.0	238.12
110	YANBU (Y2)	WESTERN	1,027.8	156.73
208	SWCC (S1)	EASTERN	792.50	123.47
208	SWCC (S2)	EASTERN	792.50	123.47
211	GAZLAN II (Z1)	EASTERN	885.33	108.89
211	GAZLAN II (Z2)	EASTERN	885.33	108.89
308	CENTR-SLACK (C2)	CENTRAL	680.30	137.37
308	CENTR-SLACK (P7)	CENTRAL	800.00	161.53
308	CENTR-SLACK (P9)	CENTRAL	800.00	161.53
401	BAHAH	SOUTHERN	893.10	211.00
508	QURAYYAT	NORTHERN	372.80	126.79
511	ARAR	NORTHERN	287.80	69.581
512	RAFHA	NORTHERN	223.00	-50.67

[a] 30% PV penetration level includes this list and all added PV plants for 10% PV penetration level.

Table C.3: List of the displaced conventional generators for 50% PV penetration level [a].

Bus number	Bus name	Operating region	Pgen (MW)	Qgen (Mvar)
204	KHARSANIYH (K1)	EASTERN	725.50	180.98
204	KHARSANIYH (K2)	EASTERN	725.50	180.98
207	MARAFIQ (M2)	EASTERN	866.67	153.50
210	GAZLAN I (G1)	EASTERN	800.00	139.09
210	GAZLAN I (G2)	EASTERN	800.00	139.09
215	SHEDQUM (H1)	EASTERN	869.75	296.78
215	SHEDQUM (H2)	EASTERN	869.75	296.78
217	FARAS (F1)	EASTERN	779.35	146.79
217	FARAS (F2)	EASTERN	779.35	146.79
301	RIYADH-1 (R1)	CENTRAL	891.67	481.58
304	KHARJ (K1)	CENTRAL	775.50	351.99
304	KHARJ (K2)	CENTRAL	775.50	351.99
308	CENTR-SLACK (P8)	CENTRAL	800.00	161.53
312	HAIL	CENTRAL	848.90	333.51

[a] 50% PV penetration level includes this list and all added PV plants for 30% PV penetration level.

Table C.4: List of the displaced conventional generators for 65% PV penetration level[a].

Bus number	**Bus name**	**Operating region**	**Pgen (MW)**	**Qgen (Mvar)**
102	JEDDAH (J1)	WESTERN	1,683.95	358.99
209	JUAYMAH	EASTERN	652.60	291.05
212	DAMMAM (D1)	EASTERN	558.70	275.87
212	DAMMAM (D2)	EASTERN	1,188.8	587.00
216	UTHMANYAH	EASTERN	722.20	365.86
301	RIYADH-1 (R2)	CENTRAL	891.67	481.58
301	RIYADH-1 (R3)	CENTRAL	891.67	481.58
309	BURAYDAH	CENTRAL	859.75	649.44
313	PP10 (P)	CENTRAL	775.50	567.51
313	PP10 (PP)	CENTRAL	775.50	567.51
503	DUBA	NORTHERN	191.10	83.20

[a] 65% PV penetration level includes this list and all added PV plants for 50% PV penetration level.

D Additional Results for Generator Trip Cases with Higher PV Penetration

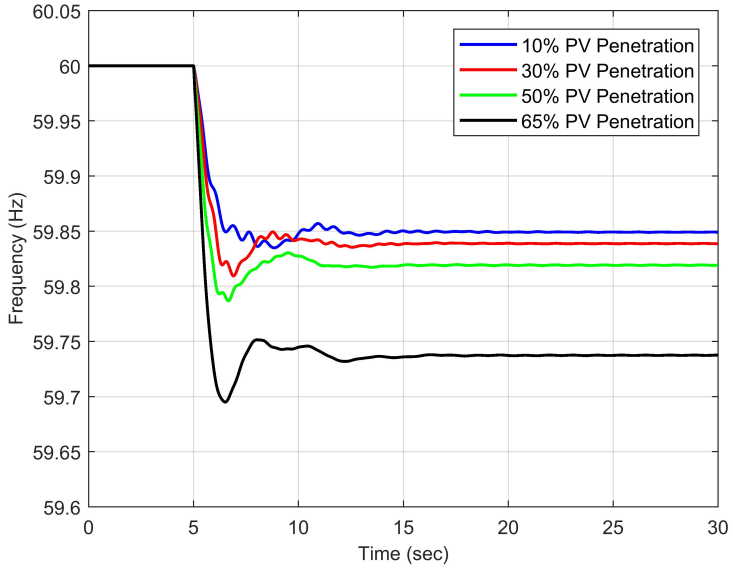


Figure D.1: Frequency responses with different PV levels after a contingency in the EOA.

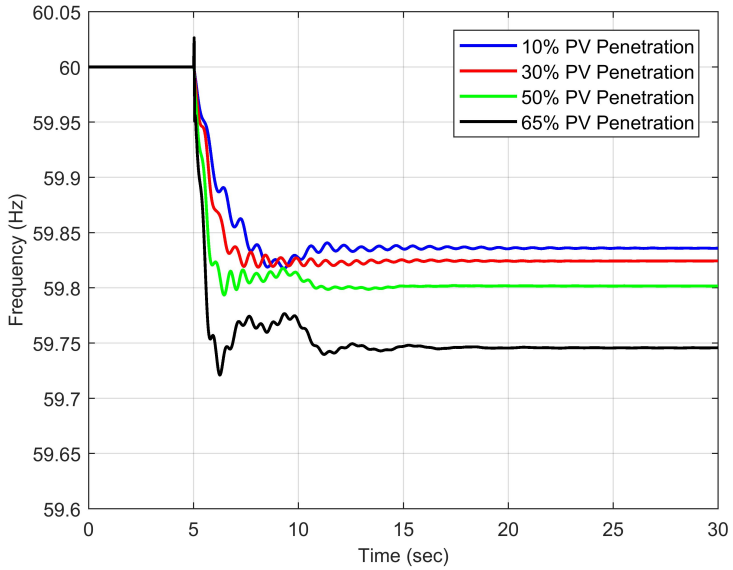


Figure D.2: Frequency responses with different PV levels after a contingency in the COA.

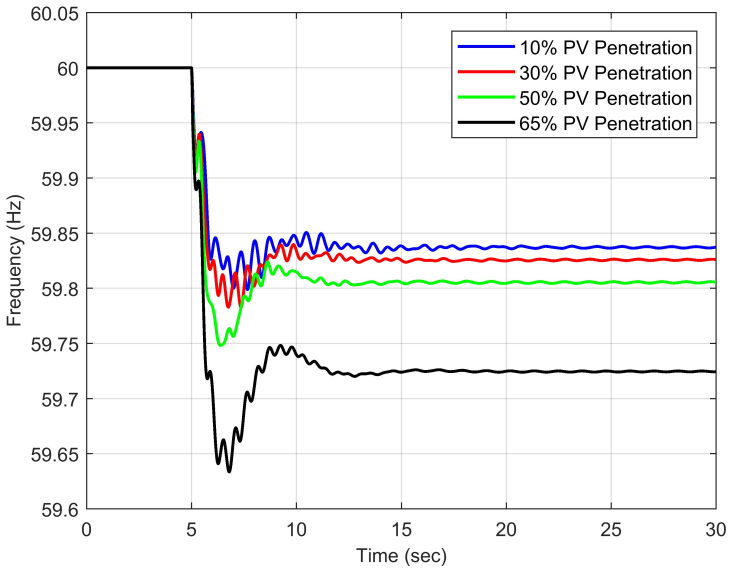


Figure D.3: Frequency responses with different PV levels after a contingency in the NOA.

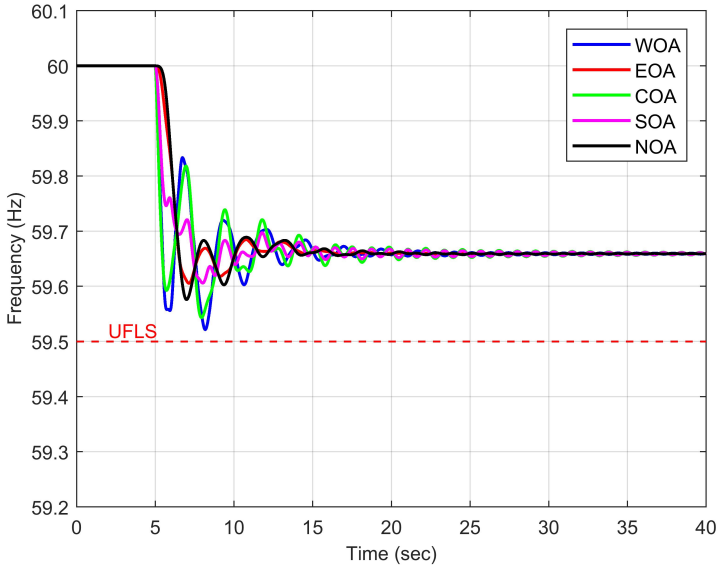


Figure D.4: Frequency responses for each area after a generator loss in the COA with 10% PV.

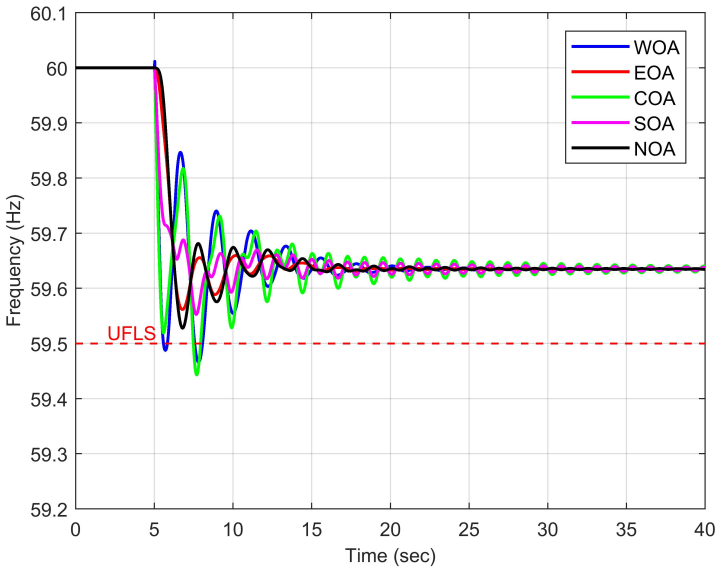


Figure D.5: Frequency responses for each area after a generator loss in the COA with 30% PV.

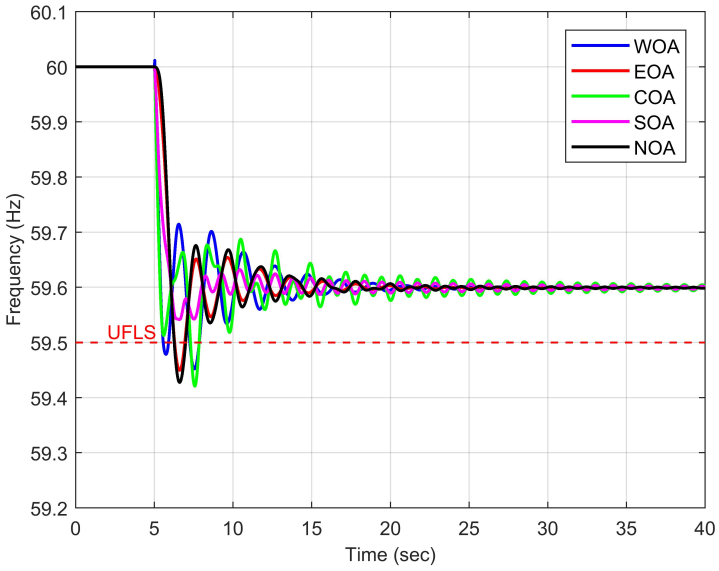


Figure D.6: Frequency responses for each area after a generator loss in the COA with 50% PV.

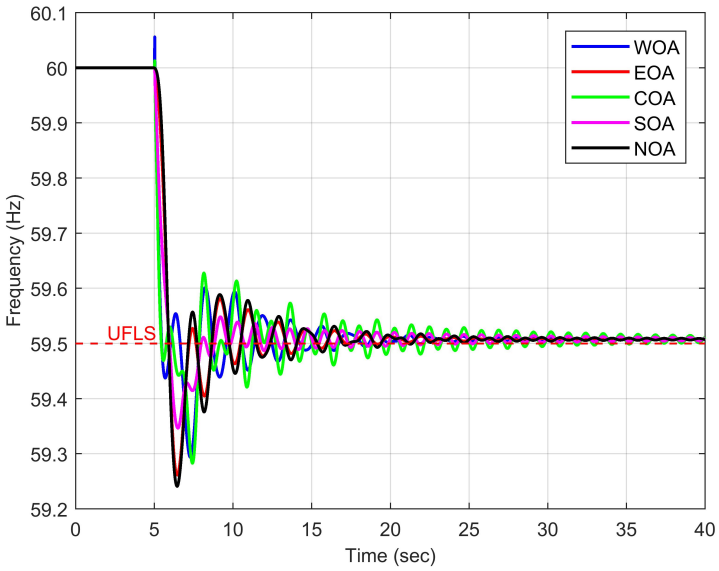


Figure D.7: Frequency responses for each area after a generator loss in the COA with 65% PV.

VITA

Abdulelah Alharbi got his Bachelor's degree in Electrical Engineering from Qassim University in 2009. He received his Master's degree from the Department of Electrical Engineering at the University of Tennessee at Chattanooga in 2013. In 2014, he started his Ph.D. study at the University of Tennessee Knoxville. His research of interest includes power system dynamic and renewable energy penetration.